Pressure Filtration of Oil Sands Mature Fine Tailings

by

Rosalynn S. Loerke

A thesis submitted in partial fulfillment of the requirements for the degree of

Master of Science

in

Chemical Engineering

Department of Chemical and Materials Engineering
University of Alberta

ABSTRACT

Dewatering of the oil sands mature fine tailings (MFT) is studied through pressure filtration following treatment by dual polymer flocculants. Polymer pairs consisting of anionic polyacrylamide (A3335) and cationic polyDADMAC (Alcomer 7115), and A3335 and non-ionic polyethylene oxide (PEO) are tested. The effect of the residual bitumen in MFT on dewaterability and filtration is also assessed. Ideal clay systems of kaolinite are compared against kaolinite slurries homogenized with bitumen at the same concentration that exists in the MFT. The dual polymer treatment of MFT is found to be more efficient than the single polymer treatment in terms of shorter capillary suction times (CST), higher filter cake solids content, higher net water release (NWR), faster water release rate, and lower specific resistance to filtration (SRF). Additionally, it is found that the addition of bitumen to pure kaolinite decreases filterability performance, but the kaolinite/bitumen mixture had comparable filterability to dual polymer flocculated MFT if treated with the same dosage of the dual polymers. The porosity of the filter cakes are assessed with micro computed tomography (micro-CT). It is found that the porosity correlates well with solids content data and that pore connectivity increases with dual polymer treatment.

ACKNOWLEDGEMENTS

Thank you sincerely to Dr. Qi Liu for his valuable academic and professional guidance, and for advising me through a masters in a field that was new to me. Thank you to Dr. Xiaoli Tan for his insightful experimental advice, and to Lisa Brandt and Brittany McKinnon for their excellent technical support. I am appreciative of Ying Zhu and Mubaraka Husain for their previous related work from which I could build upon. Thank you to Natural Resources Canada (NRCan) and Imperial Oil Limited for the financial support, and Simon Yuan (Syncrude) and Babak Jajuee (Imperial Oil) for their feedback and technical advice. Thank you to Dr. Petr Nikrityuk for his involvement, patience, and support with the CFD modeling of dense multi-phase slurry systems: a field I was also new to. Thank you to Dr. Michael Doschak and Waheed Asghar for their support and providing the facilities to carry out my micro computed tomography work. Finally I am gratefully thankful for my parents and partner who have given their unconditional support for my education and goals.

TABLE OF CONTENTS

LIST OF TABLES

LIST OF FIGURES

LIST OF ABBREVIATIONS

BL	Bottom Layer
BMD	Bone Mineral Density
CFD	Computational Fluid Dynamics
CHWE	Clark Hot Water Extraction
CNRL	Canadian Natural Resources Ltd.
CST	Capillary Suction Time
DLVO	Derjaguin-Landau-Vervey-Overbeek
EDL	Electric Double Layer
ESVC	Excess Solid Volume Correction
FFT	Fluid Fine Tailings
HMW	High Molecular Weight
HU	Hounsfield Unit
IO	Inner-Outer
LES	Large Eddy Simulation
MBI	Methylene Blue Index
MFM	Multi Fluid Model
MFT	Mature Fine Tailings
Micro-CT	Micro Computer Tomography
ML	Middle Layer
MRF	Multiple Reference Frame
NWR	Net Water Release
PAM	Polyacrylamide
PBT	Pitched Blade Turbine
PEO	Polyethylene oxide
polyDADMAC	poly(diallyldimethylammonium chloride)
PSD	Particle Size Distribution
PZC	Point of Zero Charge
Q-XRD	Quantitative X-Ray Diffraction
RAM	Random Access Memory
RANS	Reynolds Averaged Navier-Stokes
ROI	Region of Interest
SEM	Scanning Electron Microscope
SG	Sliding Grid
SRF	Specific Resistance to Filtration
SVM	Settling Velocity Model
VOI	Volume of Interest

1 INTRODUCTION

1.1 Introduction to Alberta Oil Sands and Tailings

Knowledge of the Canadian oil sands dates back 300 years when James Knight observed "gum or pitch that flows out of the banks of a river" (the Athabasca) (CAPP, 2016a). Subsequent geological exploration delineated that the oil sands underlie 142,200 km^2 of land with 3.4% being close enough to the surface to be accessible by open pit mining (AER, 2015). The total bitumen production in 2015 was 2.5 million barrels per day with approximately 46% of the bitumen extracted from open pit operations and the balance extracted in situ from reserves that were too deep for open pit mining (AER, 2016). In open pit mining, the overburden is removed and the oil sands ore is collected for bitumen extraction via a warm water process based largely on the original Clark Hot Water Extraction (CHWE) Process (Clark, 1939). In this process, the crushed ore is mixed with process water and sodium hydroxide and then sent through tumblers or hydrotransport pipelines to primary separation vessels (PSV). During hydrotransport the bitumen is liberated from the sand grains, and in the PSV air bubbles are introduced which attach to the bitumen and form a bitumen froth that is skimmed off. A middling stream, containing unaerated bitumen, is discharged from the middle of the PSV and processed in self-aerated flotation cells or cyclo-separators to recover the bitumen. The sands/clay/water mixture containing residual bitumen is removed from the bottom of the PSV as primary tailings. The bitumen froth is treated to reject trapped

water, sands, and fine clays into froth treatment tailings. Both the primary tailings and the froth treatment tailings are discharged to the tailings ponds (Fig. 1). For every barrel of bitumen produced by open pit mining, about 21 barrels of total tailings are generated (Masliyah *et al.*, 2011).

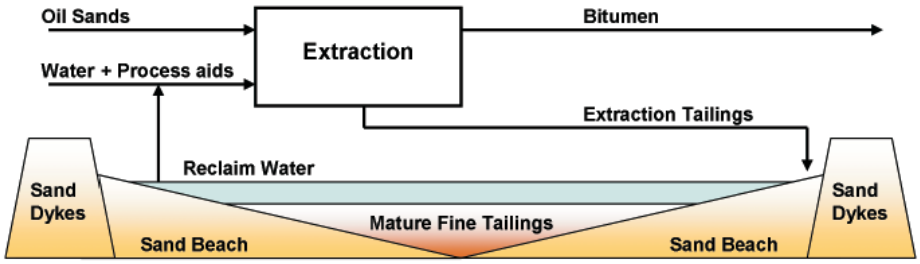

Figure 1. Water-based oil sands extraction and tailings disposal (Beier & Sego, 2008)

In the tailings ponds, the coarse solids settle quickly and the clarified water is recycled back to the extraction process. The remainder of tailings, known as fluid fine tailings (FFT), contain fine solids at a concentration of about 20 wt.%. After several years, the FFT settles to a gel-like slurry known as mature fine tailings (MFT) with a solids content between 30-40 wt.% and traces of process chemicals, naphthenic acids, and bitumen. Fine clays make up the majority of the solids in MFT with particle sizes $d_{90} < 44$ μm (Masliyah *et al.*, 2004). The predominant clay species in MFT are kaolinite and illite at 80% and 15% respectively. The arrangement of the predominant clay species has been described as a "house of cards" like structure, as shown in Figure 2, that effectively traps water. This is one of the reasons why it is difficult to remove water from fine clays (Van Olphen, 1977).

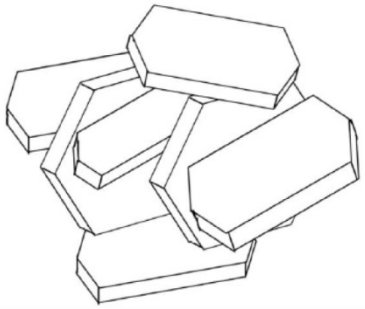

Figure 2. “House of cards” clay structure observed in MFT (Hunter, 2000).

1.2 Current State of Tailings Management

With $1.2 billion invested in tailings reduction strategies by oil sands operators (CAPP, 2016b), a vast suite of technologies have been researched, tested, and piloted. The treatments include physical, mechanical, chemical, and natural processes and in many approaches different technologies have been combined to achieve the desired result. Physical and mechanical treatments include filtration of whole, coarse, or thickened fine tailings, cross flow filtration of whole tailings, centrifugation of fine tailings, pressure plate filtration, thermal drying of MFT, electro-kinetic treatment, blast densification, wick draining, and surcharge loading. Chemical treatments include coagulation and flocculation of the tailings, and biological and chemical in-situ treatments. Natural processes include sedimentation, self-weight consolidation, evaporative drying, accelerated dewatering by rim ditching, freeze thaw, and plant (evapotranspiration) dewatering. Further management of the tailings includes co-disposal with overburden, sand, and

reclaimed material, and storage strategies such as storing the MFT in water capped lakes (BGC Engineering Inc, 2010; COSIA, 2016). Technologies that are currently being employed commercially use freshwater capping, creating a composite tails mixture of fine tails and gypsum, thin lift dewatering and centrifugation to separate water from tailings (Sobkowicz, 2012).

Coagulation of whole tailings with gypsum has been studied since the early 1980s (Liu *et al*., 1980), however the commercial use of high-molecular-weight flocculants to rapidly dewater MFT must still overcome the challenges of sensitive mixing conditions and efficient dosing that are unique to large polymer molecules.

1.3 Problem Statement

There is ever growing political, social, and environmental pressure to reclaim the land and waste from oil sands operations. To date, the tailings ponds cover 176 km^2 and hold enough liquid to fill the equivalent of 390,000 Olympic-sized swimming pools. According to Alberta Environment, if dikes, berms, beaches and other pond infrastructure are included, the footprint extends to 220 km^2 (AESRD & AER, 2015; Steward, 2015). It is predicted that Syncrude's production of MFT will reach one billion cubic meters by 2025 and that Suncor's will reach 800 million cubic meters by 2033 (Masliyah *et al.*, 2011). These estimated accumulations would fill 720,000 Olympic-sized swimming pools.

Filtration is one avenue of potential treatment options, and much work has been devoted into examining the filterability of MFT. Pressure filtration (Alamgir *et al*.,

2012; Yuming *et al*., 2008; Zhu, 2015) and vacuum filtration (Liu *et al*., 1980; Zhu, 2015) have been assessed for flocculated oil sands tailings with various polymer treatment and treatment conditions. Numerous studies have been performed on FFT, coarse tailings, and diluted MFT. Little open literature exists on the flocculation and filtration however of whole MFT with solids content greater than 30 wt.%. Whole MFT has proven to be difficult to dewater due to its gel-like structure, which not only effectively holds water but also poses a challenge in even flocculant distribution.

Furthermore, it has been reported that the presence of residual bitumen hinders the settling rate of flocculated MFT (Klein, 2014) and lowers the attachment energy of certain polymers such as polyacrylamides (Long *et al*., 2006). It is also speculated that the bitumen may bind to the filtration medium and further hinder filtration. This would pose more of an obstacle in filtration methods that reuse the filter media such as a filter press that uses filter cloths.

1.4 Thesis Objectives

Filterability of dual polymer flocculated whole MFT is assessed. The rationale behind the use of the dual polymer flocculants is that the filter cake will maintain sufficient hydraulic conductivity to ensure continuous filtration. It is hypothesized that the second stage of flocculation bridges the flocs formed in the first stage, thus creating large water channels for water release as shown in Figure 3.

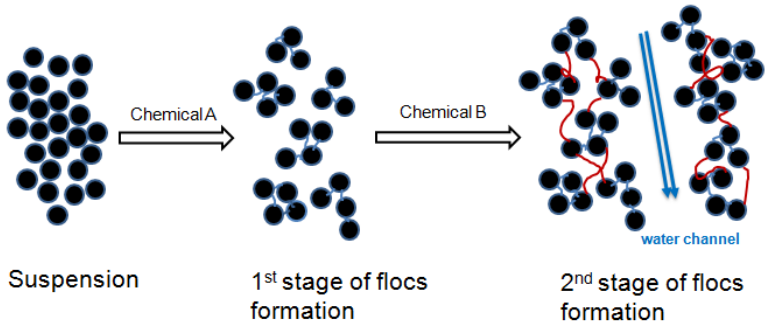

Figure 3. Hypothesized mechanism of dual stage floc formation (adapted from (Fan *et al.*, 2000).

Evidence supporting this hypothesis has been shown in earlier work on cationic and anionic dual polymer treatment of MFT (see Section 2.2 Fig. 9) (Zhu, 2015). Two polymer pairs are assessed in this work; cationic poly(diallyldimethyl-ammonium chloride) (polyDADMAC) commercially known as Alcomer 7115 paired with anionic linear polyacrylamide (PAM) commercially known as A3335, and A3335 paired with nonionic polyethylene oxide (PEO).

The filterability of the dual polymer flocculated MFT is assessed using capillary suction time (CST), net water release (NWR), water release rates, specific resistance to filtration (SRF), and solids content of filter cakes produced with a laboratory filter press. The ultimate goal is to produce filter cakes with solids content of over 70 wt.%

This work also contrasts the effect that residual bitumen has on the filterability of MFT by comparing high purity kaolinite samples with and without homogenizing with residual bitumen at the same concentration that is present in MFT.

The porosity and pore connectivity of filter cakes from MFT, kaolinite, and bitumen modified kaolinite treated with polymers is assessed with micro computed tomography (micro-CT) analysis. Relationships between pore structures, bitumen content, and filterability are addressed.

2 LITERATURE REVIEW

2.1 Chemical and Physical Properties of MFT

2.1.1 Tailings Composition

The Athabasca oil sands typically consist of a mixture of sand grains, mineral solids, clays, water, electrolytes, and bitumen. Once the oil sands have been processed, much of the solids end up in the tailings, which also contains residual bitumen, additional added water and chemicals such as caustic soda and surfactants.

After settling, the typical MFT composition is about 30-40 wt.% solids and 60-70 wt.% water, 1-3 wt.% residual bitumen, with traces of other process chemicals and naphthenic acids. For consolidation purposes, it is the settling of and water release from the fine clays within MFT that poses the greatest challenge. Clays refer to mineral solids less than 2 μm whereas fines refer to solids smaller than 44 μm. The typical composition of oil sands clays dominates in kaolinite (69%) and illite (28%) with small amounts of chlorite (1%), smectite (0.3%), and other mixed layer clays (1.7%) (Masliyah *et al.*, 2011).

The MFT also contains a number of toxic components that require containment within specifically designed ponds. Traces of benzene, toluene, polycyclic aromatic hydrocarbons, phenolic compounds, ammonia, naphthenic acids, and trace heavy metals such as mercury, lead, and arsenic have been detected (Kelly *et*

al., 2009; Nix & Martin, 1992; Pembina Institute, 2010). Naphthenic acids are considered to have the greatest effect on toxicology (Bauer, 2013).

2.1.2 Clay Properties

The clay minerals present in MFT are composed of two basic layers: a silicon-oxygen tetrahedron sheet (T), and an aluminum-oxygen-hydroxyl octahedron sheet (O) known as gibbsite. When the O-sheet is made of magnesium hydroxide, then it is known as brucite. The different arrangements of the T and O sheets results in the different clay minerals as shown in Figure 4.

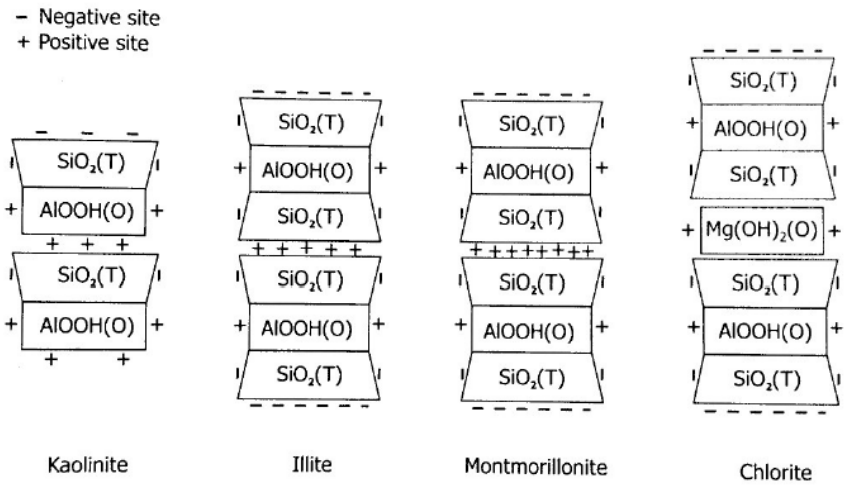

Figure 4. Schematic structure of the dominate clay species found in MFT (Masliyah *et al*., 2011).

The clays are able to absorb calcium from the process water, which occurs via a cation exchange mechanism and the clays can also undergo isomorphic substitution of higher or lower valence cations of similar sizes. For example, in the T sheet, Si^{4+} can be substituted by Al^{3+} and in the O sheet, Al^{3+} can be substituted by Mg^{2+}. Typically the isomorphic substitution leaves the clay units with a net negative

charge, and compensating cations such as Na^{+}, K^{+}, Ca^{2+}, Mg^{2+}, and Fe^{2+} will associate to make the clay electrically neutral.

The various surface properties of the clays affect flocculation with different polymers. Polymer flocculation of MFT relies largely on non-covalent chemical interactions, which are affected by the surface properties and surface charges of the interacting species. Non-covalent chemical interactions include electrostatic interactions (hydrogen and ionic bonding), Van der Waals forces, and hydrophobic effects (Bruice, 2012).

2.1.2.1 Kaolinite $Al_2Si_2O_5(OH)_4$

Kaolinite is a two-layer (T-O) clay with a Si:Al ratio of 1:1 as shown in Figure 5. There is basal oxygen on the T surface sheet and hydroxyls on the O sheet. Bonding between Si:Al units occurs via hydrogen bonds between the hydroxyls and the oxygens. There are many of these bonds, thus making the interaction very strong and not allowing the clay to swell when immersed in water or electrolyte solution.

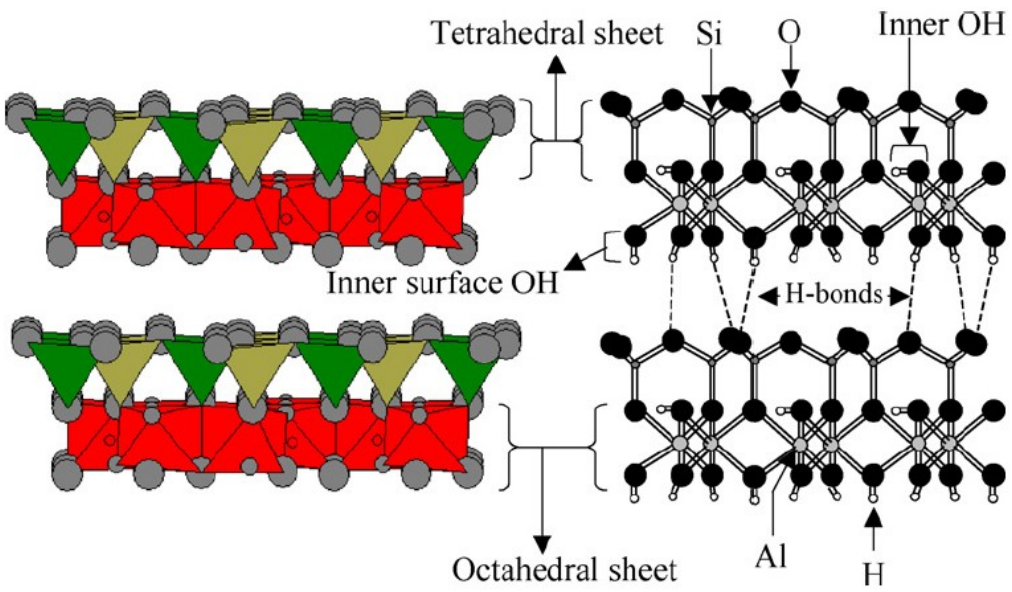

Figure 5. Structure of two units of kaolinite (Konan *et al*., 2007).

Water can however intercalate to form $Al_2Si_2O_5(OH)_4 \cdot H_2O$. There is very little ionic penetration into the interlayer, and cationic exchange capacity is low (3-5 meq/100 g) (Mitchell, 1976). Cationic exchange occurs mainly at the edges of the layers. Isomorphic substitution occurs at a low level with Al^{3+} substituting for Si^{4+} on the T sheet and Mg^{2+} for Al^{3+} on the O sheet, resulting in a relatively low permanent negative charge (Masliyah *et al.*, 2011).

2.1.2.2 Illite $K(Al,Fe,Mg)_5(Al,Si)_8O_{20}(OH)_4$

Illite is a three-layer (T-O-T) clay with a Si:Al 2:1 ratio as shown in Figure 6. Isomorphic substitution occurs at a high level with a quarter of the Si atoms being substituted with Al^{3+} in the T sheet. The compensating ions which are mainly potassium, sit in the hexagonal holds, thus making the binding of the units strong.

For this reason, the potassium does not participate in cation exchange, and the exchange takes place on edges with a capacity of 10-40 meq/100 g (Mitchell, 1976).

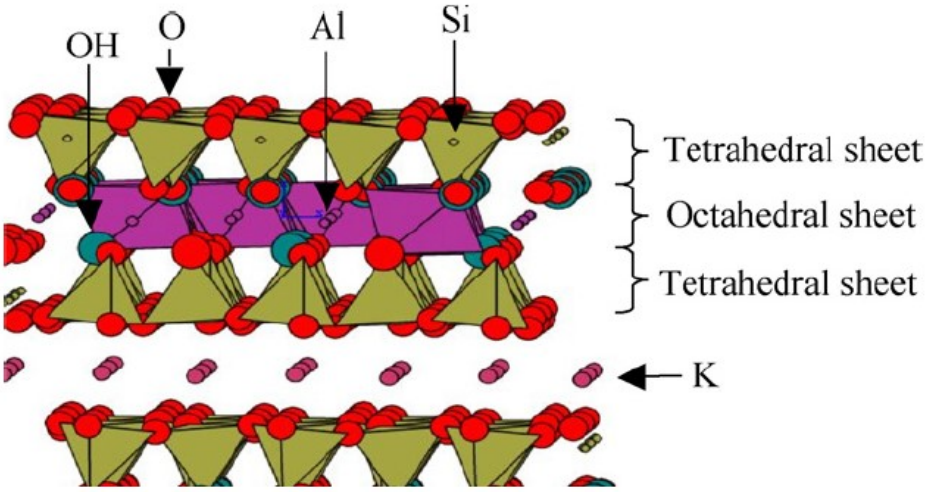

Figure 6. Structure of illite with potassium ions in the interlayer (Konan *et al.*, 2007).

2.1.2.3 Montmorillonite $(Na,Ca,H_3O)_x[Al_{4-x}(Fe,Mg)_xSi_8O_{20}(OH)_4]$

Isomorphic substitution occurs on both the T and O sheets of smectite clays such as montmorillonite. The substitution on the O sheet delocalizes the charge on the O sheet however, resulting in the compensating ions sitting on the T sheet. This weakens the interlayer binding allowing the compensating ions to participate in cation exchange at a high capacity (80-150 meq/100 g) (Mitchell, 1976), and this results in the swelling characteristic seen in smectite clays (Masliyah *et al*., 2011). The difference between illite and montmorillonite is shown in Figure 7.

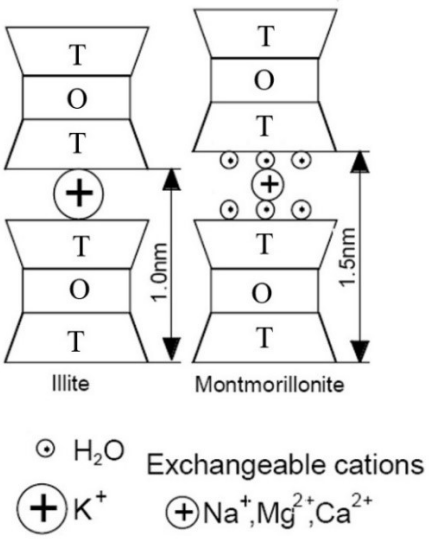

Figure 7. The structure of montmorillonite is similar to that of illite with the exchangeable cations being Na^{+}, Mg^{2+}, and Ca^{2+} rather than K^{+} (Rajagopalan, 2016)

2.1.2.4 Chlorite $(Mg,Fe,Al)_6(Al,Si)_4O_{10}(OH)_8$

Chlorite is a three-layer clay however it is sometimes considered a four-layer clay since its charge compensation occurs through the positively charged brucite layer, in which some Mg^{2+} ions are substituted by Al^{3+} ions. The isomorphic substitution occurs in both the T and O layer and the cation exchange occurs at the same capacity as illite (Masliyah *et al*., 2011; Mitchell, 1976).

2.2 Flocculation of Tailings

Ideally, polymers are added to the MFT to create large flocs. Unlike coagulation, flocculation does not require a reduction in the repulsive electrostatic forces between aggregating particles because the polymer bridge can extend

beyond the range of the electrical double layer repulsion (Masliyah *et al*., 2011). Aggregation by flocculation thus creates more open structures than coagulation where water can be trapped within the small aggregates. The pore structures that are created within large flocs can provide channels for water flow. Previous work on dual polymer flocculation and filtration of MFT has provided visualization of the pore network quite nicely with cryogenic-scanning electron microscopy (cryo-SEM) as shown in Figure 8 (Zhu, 2015).

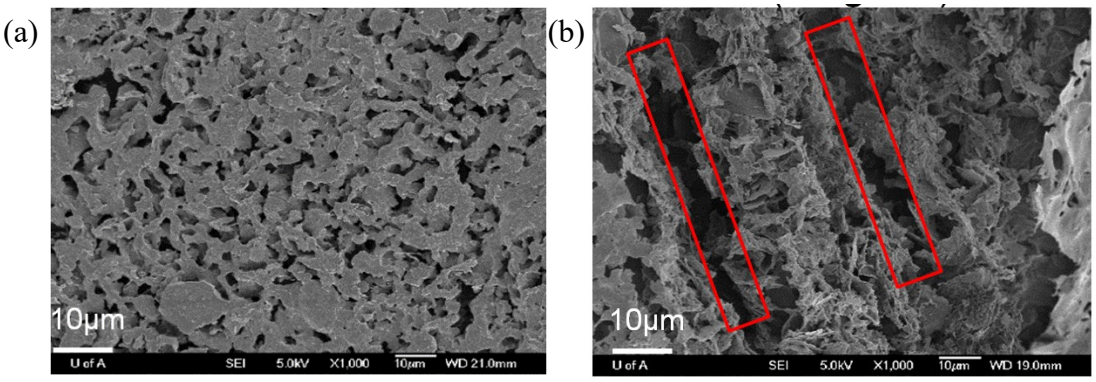

Figure 8. Comparison of (a) untreated MFT and (b) MFT treated with dual polymers A3335 and Alcomer 7115 (Zhu, 2015).

Often in the presence of polymers, compliance with the classical Derjaguin-Landau-Vervey-Overbeek (DLVO) theory is not observed and additional forces must be considered. In addition it has been demonstrated that dramatic increases in rheology, and complex rheological behavior resulted from non-DLVO forces when kaolinite dispersions were mixed with high molecular weight polyethylene oxide (PEO) or high molecular weight anionic poly acrylamides (PAM) (Mpofu *et al*., 2003; Neelakantan, 2016). Flocs and aggregates are influenced by shear; therefore, it is important to consider physical mixing variables such as the duration

and intensity of agitation and the equipment used (Demoz & Mikula, 2012; Farinato & Dubin, 1999). Chemical effects such as pH and polymer additives, and mineralogy of the slurry, as well as colloidal forces such as polymer bridging, steric repulsion, hydrophobic interaction, hydration, hydrodynamic and depletion forces must also be considered in MFT flocculation (Sworska *et al.*, 2000).

Hydrophobic forces arise on surfaces of the clay particles that lack hydrogen bonding acceptors, donors, and polar groups and thus interact poorly with water (Masliyah *et al*., 2011). As a result, the water molecules near the surface become highly ordered which generate forces that are entropic in nature (Masliyah *et al.*, 2011). These forces can extend to a long range, and their magnitude has been experimentally measured and found to be stronger and of a longer range than typical van der Waals interactions, although the nature of the force is still not well understood (Masliyah *et al*., 2011). The attachment of PEO to silica has been described as arising from entropic effects from the displacement of water at the surface (Rubio, 1976).

Numerous studies (e.g., Fan *et al*., 2000; Mpofu *et al*., 2003; Ovenden & Xiao, 2002) have demonstrated that the primary mechanism of flocculation with PAM is through polymer bridging. The bridging mechanism requires that the polymer be of high enough molecular weight and of the right charge density to project itself past the electric double layer allowing it to adsorb on another particle. It has been shown that kaolinite particles bridged by lower charge density polymers produced larger flocs and thus resulted in faster settling rates (Haroon, 2014). Although both PEO and PAM adsorb to kaolinite particles through hydrogen bonding, hydrolyzed

PAMs have lower adsorption due to electrostatic repulsions between anionic pendant groups.

The adsorption of polymers onto clay surfaces can occur in a number of arrangements as shown in Figure 9.

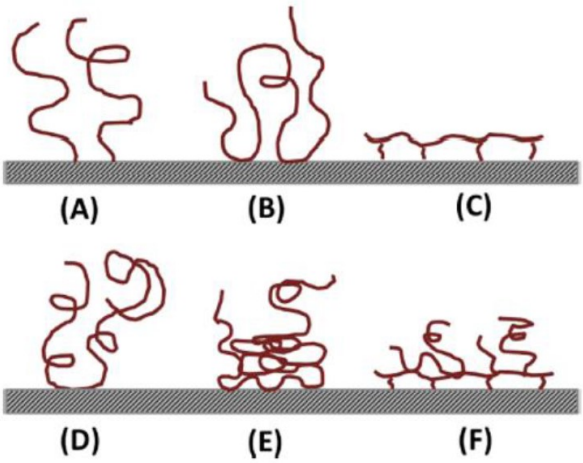

Figure 9. Possible configurations of polymer adsorption on a solid surface: (a) single point attachment; (b) loop adsorption; (c) flat multiple site attachment; (d) random coil; (e) non-uniform segment distribution; and (f) multilayer adsorption (Alagha *et al*., 2013).

The strongest adhesion of the above conformation is the flat multiple site attachment (Fig. 9c), however this conformation may not result in the best flocculation since it reduces bridging of particles and blocks additional adsorption of polymers onto the solid surface (Klein, 2014). The weakest is the single point attachment (Fig. 9a). The random coil attachment is observed with higher molecular weight polymers.

2.2.1 Effect of Solution pH and Electrolytes

The various clays present in MFT have different surface charges (see Section 2.1.2) and different points of zero charge (PZC points) where the surface charge of the clay is neutral. The pH of the solution thus affects what the surface charges of the clays will be. If the pH is adjusted to a point where the surface charges reduce the electric double layer (EDL) repulsions, then attractive van der Waals forces will dominate and more rapid coagulation will occur. The degree of ionization of ionic polymers is also affected by pH, which affect the polymer's adsorption onto the clay surfaces. Along with reducing the surface charges on the clays, another way to reduce the EDL repulsions is to reduce the thickness of the EDL by increasing the salinity of the solution. This relationship is shown in Figure 10 where the electrical potential and the distance over which the EDL is present decreases as the salinity increases.

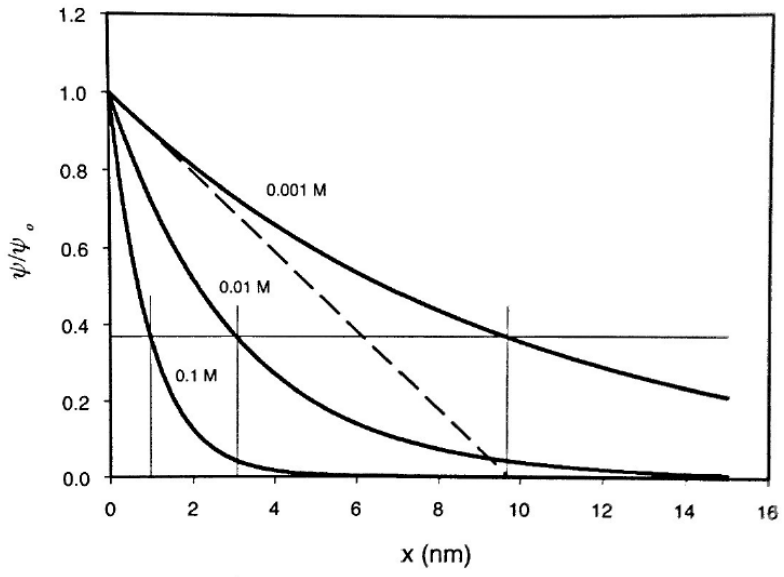

Figure 10. The electric potential (ψ / ψ_o) of the EDL as a function of distance (x) from a charged interface for different 1:1 electrolyte concentrations (Masliyah *et al.*, 2011).

Additionally, the presence of monovalent cations such as Na^{+}, K^{+}, and multivalent cations such as Ca^{2+}, Mg^{2+}, can adsorb onto the surface of oxides and participate in cation exchange thus lowering the surfaces negative charge and lowering repulsive interactions between particles (Masliyah *et al*., 2004). Metal ions such as Al^{3+}, Cu^{2+}, and Fe^{3+} have been added as coagulants due to their role in charge neutralization as well (Long *et al*., 2006; Sworska *et al*., 2000).

2.3 Effect of Residual Bitumen in MFT

Residual bitumen is found in MFT at concentrations between 1-3 wt.%. It was determined by SEM imaging that the bitumen was present as free droplets ranging in size from 1 to 10 μm (Mikula *et al*., 1993). It was also found that bitumen adhered to the edges of the clays, possibly contributing to the stability of MFT. The distribution of residual bitumen in MFT is shown in Figure 11.

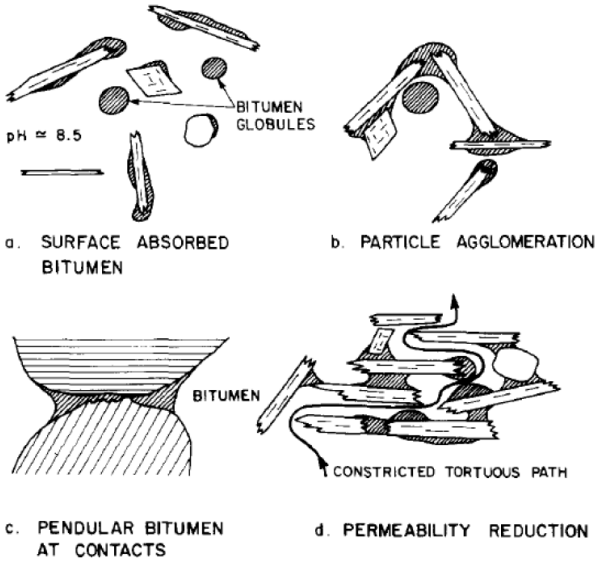

Figure 11. Position and effects of bitumen droplets with respect to clay particles (Scott *et al.*, 1985).

Residual bitumen has a negative impact on the filterability of MFT. It was found that the residual bitumen decreases the hydraulic conductivity of the MFT by combining with ultra-fine particles and blocking pores between particles, thus interfering with water release and consolidation (Suthaker & Scott, 1996; Vedoy & Soares, 2015). It was also found that the presence of bitumen decreased the settling rates of flocculated MFT (Klein, 2014). Work with Al-PAM (a hybrid $Al(OH)_3$-polyacrylamide) has shown that such a polymer is able to flocculate dispersed bitumen droplets along with the fine clays by lowering the bitumen's surface charge, thus increasing adhesion between the droplets. It is hypothesized that coalescing the fine droplets into larger drops would result in less blockage of pores within filter cakes and filter medium (Wang *et al.*, 2010).

2.4 Principles of Tailings Filtration

The formation of a MFT cake through filtration can be described by looking at two filtration models as shown in Figure 12.

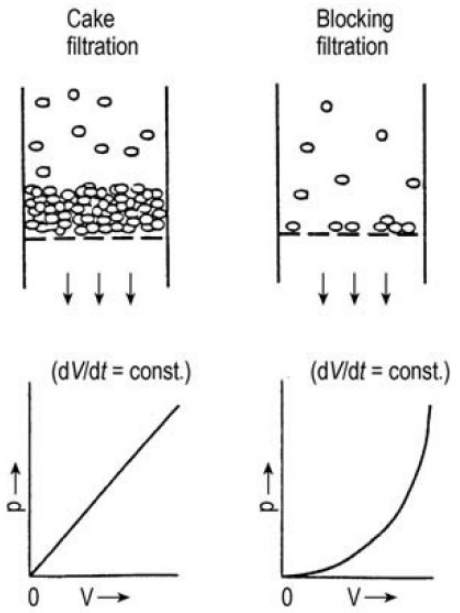

Figure 12. Filtration models showing the filtrate volume (V) accumulation with respect to pressure (p) under constant dV/dt (Ripperger *et al.*, 2000).

In the cake filtration model, it is assumed that rigid particles are deposited on the filter medium as a homogenous porous layer with a constant permeability. As the filtration proceeds, additional layers are deposited. In the blocking filtration model, pores within the filter cake become blocked by migrating fine particles or drops of deformable material, causing a pressure drop.

In the cake filtration model the specific resistance to filtration (SRF) is a calculated variable that quantifies the filterability of a material. The SRF calculation is based on a theoretical filtration model (Coulson *et al*., 1990) that is based on the Darcy's equation:

$$\frac{\mathrm{d}V}{\mathrm{d}t} = \frac{A\Delta P}{\frac{\mu_f(\mathrm{SRF})cV}{A} + \mu_f R} \tag{1}$$

where, V is the volume of the filtrate (m^3) in the filtration time t (s); A is the filter area (m^2); ΔP is the pressure drop (Pa); μ_f is the viscosity of the filtrate (Pa·s); SRF is the specific resistance to filtration of the cake (m/kg); c is the solids concentration of the slurry (kg/m^3); and R is the resistance of the filter media (m^{-1}). The concentration of the slurry c can be calculated in two ways:

$$c_H = \frac{H \cdot A}{V} \tag{2}$$

$$c_m = \frac{m}{V} \tag{3}$$

Using c_H considers the cake height (H) and thus the influence of porosity whereas using c_m considers the mass (m) of the particles in the filter cake with respect to the filtrate volume, thus making it independent of the cake porosity.

Since Darcy's equation assumes that the pressure drop is constant and that the cake is incompressible, Equation 1 can be integrated so that t/V is expressed as:

$$\frac{t}{V} = \frac{\mu_f(\mathrm{SRF})c}{2\Delta P A^2} V + \frac{\mu_f R}{\Delta P A} \tag{4}$$

The slope (b) of the t/V versus V profile thus yields the SRF using:

$$\mathrm{SRF} = \frac{2\Delta P A^2}{\mu_f c} b \tag{5}$$

Once the SRF is determined experimentally, the filtration rate can be calculated from:

$$\frac{\mu_f \mathrm{SRF} c}{2\Delta P A^2} V^2 + \frac{\mu_f R}{\Delta P A} V - t = 0 \tag{6}$$

This relationship has potential benefits in commercial applications where it may be desirable to predict the time it would take to achieve a certain filtrate volume, or a reasonable filter area required for scale up.

In the blocking filtration model, it is more realistic that the blocking may be intermediate rather than complete. Moderate blocking can be described by a generalized model with the following equations (Ripperger *et al.*, 2000):

$$\frac{\mathrm{d}^2 t}{\mathrm{d}V^2} = \mathrm{const} \cdot \left(\frac{\mathrm{d}t}{\mathrm{d}V}\right)^q \tag{7}$$

for constant pressure filtration and

$$\frac{\mathrm{d}(\Delta p)}{\mathrm{d}V} = \mathrm{const} \cdot (\Delta p)^q \tag{8}$$

for constant rate filtration.

The exponent q varies between 0 and 2 to describe the blocking speed where:

q = 0 cake filtration, slow blocking

q = 1 so-called intermediate filtration

q = 3/2 so-called standard blocking filtration

q = 2 complete blocking.

2.5 Micro Computed Tomography for Filter Cake Porosity Analysis

X-ray micro computed tomography (micro-CT) was initially developed for the medical field with the application of imaging tissues and bones. Recently the characterization of pores by micro-CT arises in countless applications with health,

mining, building materials, cosmetics, construction, agriculture, food, and household products. The technique allows for non-destructive and repeated visualization of a sample without the need to chemically or physically alter the sample. X-rays penetrate the sample and the transmission of these waves to a detector depends on the mass density and mass absorption coefficient of the material. From the array of two dimensional (2D) images generated, three dimensional (3D) structures can be reconstructed. In the geological field, micro-CT is used to analyze soil, rocks, and clays for porosity, permeability, and fracture distribution. Specific applications such as determining the network of filter cake pores and phase determination between clays, water, and oil phases have also been studied. Recent work has been able to distinguish pore networks and bitumen and kerogen placement within source rock using krypton to provide contrast in the imaging (Glatz *et al.*, 2016). Other recent work has looked at differentiating the oil phase from water phase within wet sandstone using a resolution of 5.4 µm and iododecane dissolved in the oil phase as a contrast fluid (Khanamiri *et al.*, 2016). It is proposed that the porosity of MFT filter cakes could be visualized, with more advanced progress leading to the potential visualization of bitumen within MFT filter cake pore structures.

3 EXPERIMENTAL MATERIALS AND METHODS

3.1 Polymers and Polymer Solution Preparation

The polymers chosen for this study were selected based on literature and prior testing results in our group (Demoz & Mikula, 2012; Haroon, 2014; Zhu, 2015) and included an anionic polyacrylamide (PAM), a cationic poly(diallyldimethyl-ammonium chloride) (polyDADMAC), and a nonionic polyethylene oxide (PEO). The anionic PAM was from SNF, with a trade name A3335, and had a high molecular weight of 17×10^6 g/mol and an anionic charge density of 30%. It has been reported that polyacrylamides with 20-30% anionic charge density were the most efficient for flocculating Syncrude fine tailings (Xu & Cymerman, 1999). Stock solutions of 0.4 wt.% A3335 were prepared from the polymer powders with de-ionized water. Reagent grade ethanol was added at 0.8 wt.% to extend the life of the polymer stock solution. The solution was agitated with a vortex mixer on "high" setting for 10 minutes at which point the polymer was fully dissolved. All A3335 solutions were used within one week after preparation.

The polyDADMAC polymer was from BASF with a trade name Alcomer 7115. Its molecular weight was specified as between 2×10^5 and 4×10^5 g/mol. The Alcomer 7115 was received in 20 wt.% stock solutions and was diluted to 2 wt.% by de-ionized water for the flocculation tests.

High molecular weight PEO was obtained from Polysciences Inc. and had a molecular weight of 8×10^6 g/mol. It was prepared in stock solutions of 0.2 wt.%

from the polymer powders and de-ionized water. The solution was agitated with a vortex mixer on "high" setting for 10 minutes at which point the polymer was fully dissolved. The PEO solution was used within a few hours of preparation due to the deterioration of its flocculation performance with time that has been observed with high molecular weights of this polymer.

3.2 MFT Samples and MFT Treatment by the Polymers

Samples of Syncrude mature fine tailings (MFT) were obtained from settled tailings ponds produced by the water-based extraction of oil sands ore from a northern Alberta deposit. The MFT sample was collected in 2012. The MFT was found to contain 35.6 wt.% solids, 2.7 wt.% bitumen, and the balance being water, as determined by the Dean-Stark procedures. This analysis was previously carried out by Ying Zhu (Zhu, 2015). Quantitative X-ray diffraction (Q-XRD) analysis determined with good repeatability that the major mineral composition to be kaolinite (36.0 wt.%), illite (30.7 wt.%), quartz (27.4 wt.%), 3.2 wt.% siderite, and 2.6 wt.% K-feldspar. Q-XRD also determined the clay to water ratio to be 0.38 with a 2:1 ratio of clays to non-clays. Q-XRD was chosen for clay to water ratio determination since the methylene blue index (MBI) test has an element of subjectivity. Clay to water ratio is reported rather than solids to water ratio as it has been suggested that the clay species are a large contributor to the MFT dewatering challenge (Kaminsky, 2006, 2014). It has also been found that in such titration methods, the presence of bitumen lowered the MBI (Osacky *et al*., 2015;

Osacky *et al.*, 2014). The particle size distribution was measured with a Mastersizer 3000 particle size analyzer (Malvern, UK) giving a distribution of $D_v(10) < 1.4$ μm, $D_v(50) < 7.8$ μm and $D_v(90) < 32.8$ μm.

The experimental procedure for flocculation tests followed a slightly modified procedure outlined by Syncrude Canada Ltd (Yuan & Siman, 2012). MFT was treated in 500 g batches in an un-baffled 130 mm diameter vessel with a 100 mm diameter 4 blade 45° PBT impeller (D/T = 0.77). A Heidolph RZR 2052 electric stirrer was used to control the impeller speed and record the torque acting on the impeller. Through a series of preliminary tests, the optimal mixing conditions and polymer dosages were determined. A3335 and PEO flocculation tests were dosed at 1000 g/t A3335 and 1500 g/t PEO. A3335 and Alcomer 7115 flocculation tests were dosed at 1000 g/t A3335 and 3000 g/t Alcomer 7115. The polymer dosages (g/t) were based on dry polymer to MFT solids content ratio. The MFT was homogenized for 120 s at 300 rpm before the first polymer addition. The speed was maintained and polymer was injected via a syringe to the impeller tips to avoid local over flocculation. Stirring ceased five seconds after the peak torque was reached. In the case of dual polymer treatment, the second polymer was added five seconds after the torque reached the peak in the same manner as the first polymer. The stirring was stopped five seconds after torque reached a peak after the second addition. The five second delay ensured that the torque was in fact decreasing rather than fluctuating. Initial mixing experiments of the polymers into the MFT showed a decrease in dewatering performance if the polymers were mixed more than 15 seconds past the peak torque.

3.3 Pure Kaolinite Samples and Their Preparation and Treatment

Kaolinite was selected to represent a simplified and ideal clay system to compare against MFT. Although kaolinite only represents just over a third of the mineral composition of MFT (the remainder were mainly quartz and illite), there are several reasons for choosing pure kaolinite rather than a blend. Quartz has not been identified as a contributor to the difficulty of dewatering MFT. High purity illite is not usually as readily available as kaolinite, and the illite samples are not only of a low purity but also supplied as shale rock and needs milling and sizing to simulate the extremely fine size of the illite in the Alberta oil sands, which was impractical. There is abundant literature on the flocculation and filtration of kaolinite systems for comparison. Two powdered kaolinite samples (BASF ASP 600 and BASF ASP 802) were used. The particle size distribution of the kaolinite as well as MFT samples are compared in Table 1 and Figure 13. As can be seen, in terms of average particle size, the BASF ASP 802 kaolinite was closer to the MFT sample.

Table 1. Kaolinite particle size distribution (volume %) comparison to original MFT.

	MFT	BASF ASP 600 Kaolinite	BASF ASP 802 Kaolinite
$D_v(10)$	1.4 μm	0.9 μm	2.4 μm
$D_v(50)$	7.8 μm	4.1 μm	8.4 μm
$D_v(90)$	32.8 μm	13.5 μm	22.7 μm

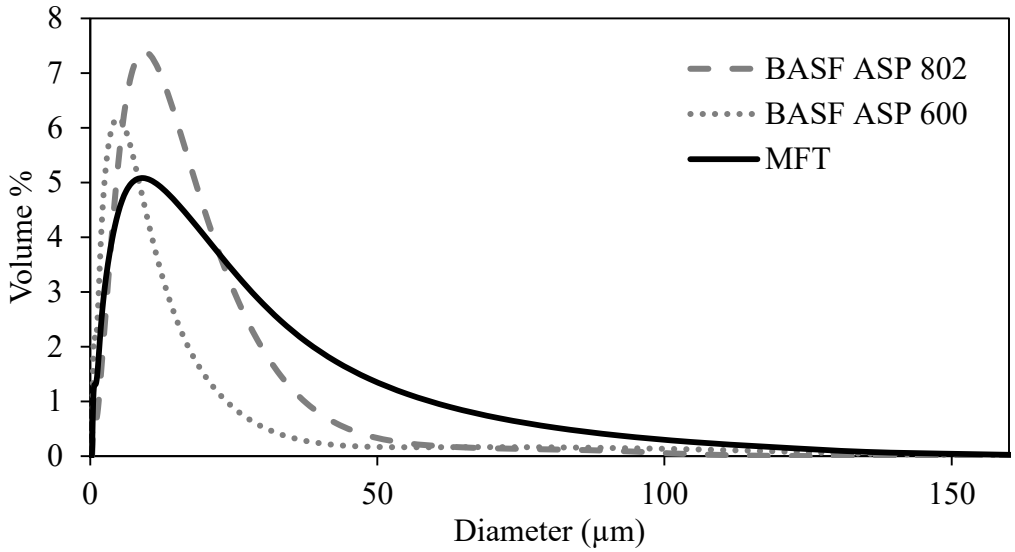

Figure 13. Kaolinite particle size distribution (volume %) comparison to original MFT.

Kaolinite slurries were prepared in 37 wt.% solids concentrations so that they would have a comparable solids concentration to that of the original MFT. The slurries were mixed in 500 g batches and were homogenized for 10 minutes at 300 rpm with a 4 blade 45° PBT impeller (D/T = 0.77) before any additional treatment.

In the flocculation experiments of pure kaolinite, the polymers were added in the same manner as with the MFT as described in *Section 3.2*. Since the kaolinite slurries required significantly less polymer than the MFT, additional water was added to the kaolinite slurry at the lower polymer dosages to eliminate the dilution effect.

3.4 Preparation of Kaolinite/Bitumen Slurry

The kaolinite/bitumen slurry samples were prepared to contain 3 wt.% bitumen so they would be comparable to the original MFT (2.7 wt.% bitumen). It was determined that introducing the bitumen into the kaolinite was the best option for even dispersion. Earlier work had determined that centrifuging (Beckman Coulter Avanti J-30I Centrifuge) MFT at 9900 rpm (17,344 RCF) for 3 hours efficiently separated the MFT into three distinct layers; bottom layer containing the mineral solids, middle layer containing the ultrafine particles and bitumen, and the supernatant containing water and trace amounts of ultrafine particles and bitumen. Canadian Natural Resources Ltd. (CNRL) MFT collected in 2016 was used for supernatant and middle layer collection. CNRL MFT was used due to the large quantities of MFT that was needed for centrifuging and the limited supply of 2012 Syncrude MFT. The whole MFT and bottom layer composition was determined by Dean-Stark, the supernatant composition was determined by dichloromethane extraction, and the middle layer composition was determined by back calculation (Appendix A). The whole MFT contained 28.8 wt.% solids, 3.6 wt.% bitumen, and balanced by water as determined by Dean-Stark extraction. The amount of middle layer needed to provide a 3 wt.% bitumen concentration in a 63 wt.% water slurry was determined (Appendix A). The middle layer, kaolinite, and supernatant were homogenized for 10 minutes at 300 rpm with a 4 blade 45° PBT impeller (D/T = 0.77) before any additional treatment.

3.5 Capillary Suction Time (CST) Measurement

A model 319 multi-purpose CST apparatus (Triton Electronics Ltd., U.K.) was used to measure capillary suction time (CST) to assess the easiness of water release, from which to infer filterability. The CST is the time it takes for the water to pass through the slurry medium and reach two electrode points. All CST measurements were taken in triplicate.

3.6 Filter Press Operation

A SERFILCO 0.02-7PPHM Lab Press was used to produce filter cakes in the assessment of filtration efficiency of each polymer treatment of the MFT or kaolinite slurries. A schematic of the filter press set up is shown in Figure 14.

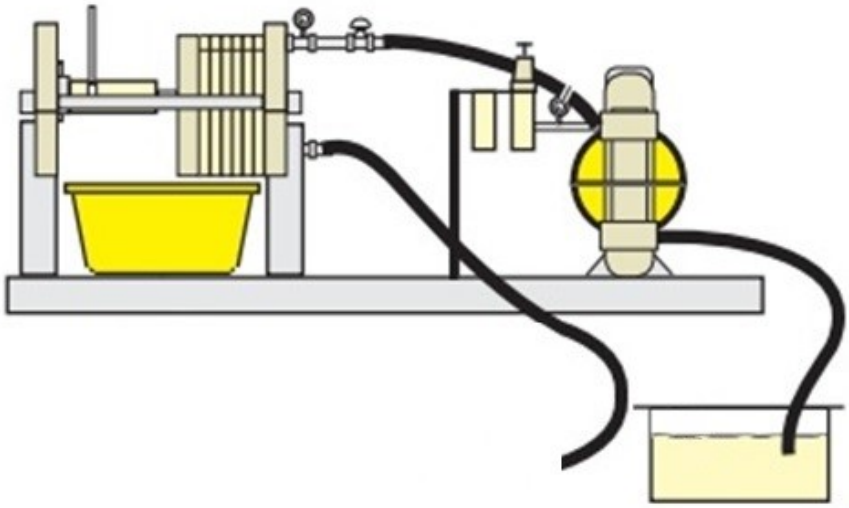

Figure 14. Filter press set up.

The 280 cm^3 plate volume configuration was used yielding a cake thickness of 2.5 cm. The total filter area was 220 cm^2 through a 15 μm mesh polypropylene filter cloth. The pressure was adjusted to 620 kPa and the air diaphragm pump had a capacity of 262 cm^3/s. Two variations of filter press tests were performed in order to assess the effect of shear induced by the pump on the flocculated MFT or kaolinite. In the "standard" filter press test, polymer-treated MFT or kaolinite was pumped through the system. In "preloaded" filter press tests, the filtration chamber between the plates was preloaded with treated MFT or kaolinite, then inserted into the filter press frame. Surplus treated MFT or kaolinite was pumped to the press to make up for the volume loss during the course of filtration. Filtrate volume was recorded as a function of time, from which water release rates were calculated. The filter cakes were removed after one hour of filtration. The amount of MFT or kaolinite that was pumped to the press was taken into account for the net water release (NWR, next section) and filtration rate calculations (Appendix C).

3.7 Determination of Filter Cake % solids and Net Water Release (NWR) Calculation

Filter cake samples were dried for 24 hours in a vacuum oven at 70°C and 80 kPa to obtain the final solids content. The net water release (NWR) is calculated by:

$$NWR = \frac{V_f - V_p}{V_{MFT}} \tag{7}$$

where V_f is the filtrate volume, V_p is the volume of water that is added to the system via polymer addition, and V_{MFT} is the volume of water that is contained in MFT (82 vol.% or 63 wt.%). Full NWR calculations are described in Appendix C.

3.8 Standard Deviations

The standard deviation on the CST and solids content measurements were determined in this study. The CST measurements were always taken in triplicate so that an average and a standard deviation for each test could be calculated. In cases where repetitions of the same test were performed, an average of the standard deviations was also calculated. For example, if one test (in triplicate) was repeated four times an average of the four standard deviations was taken.

To determine the standard deviation associated with the filter press, a standard deviation was determined for the MFT tests and a standard deviation was determined for the kaolinite tests. Two of the filter press tests with the MFT (1000 g/t A3335 + 3000 g/t Alcomer 7115, and 1000 g/t A3335 + 1500 g/t PEO) and two of the kaolinite filter press tests (control and 50 g/t A3335 + 150 g/t Alcomer 7115) were carried out in triplicate (total of four tests repeated three times each). The standard deviation on the final cake solids content (wt.%) was calculated for each test. An average standard deviation was calculated for the MFT tests (s = ±1.8 wt.%) and an average standard deviation was calculated for the kaolinite tests (s = ±0.35 wt.%). It was assumed that all MFT filter press trials had a standard deviation

of ±1.8 wt.%, and all kaolinite filter press trials had a standard deviation of ±0.35 wt.%.

3.9 Micro Computed Tomography Imaging and Analysis

3.9.1 Scanning and Image Processing

Micro computed tomography (micro-CT) scanning was carried out with a Bruker Skyscan® 1076 *in-vivo* micro-CT imager (Skyscan NV, Kartuisersweg, BE) capable of imaging pixel sizes of 9, 18, and 35 μm. All scans of the filter cakes and phantoms were run at 9 μm resolution under the same voltage (100 kV), current (100 μA), rotation step (0.5°) for a full 360° scan. A phantom scan is a scan of a material with known bone mineral density (BMD) and is used for calibration. BMD is defined as the volumetric density of calcium hydroxyapatite (CaHa) in terms of g/cm^3. Reconstruction was done using Skyscan® NRecon program. Figure 15 shows the three dimensional reconstruction of the air/water phantom scan. Figure 15 c shows the original image and Figure a, b, d, e, shows the x, y, and z, planes of the reconstruction.

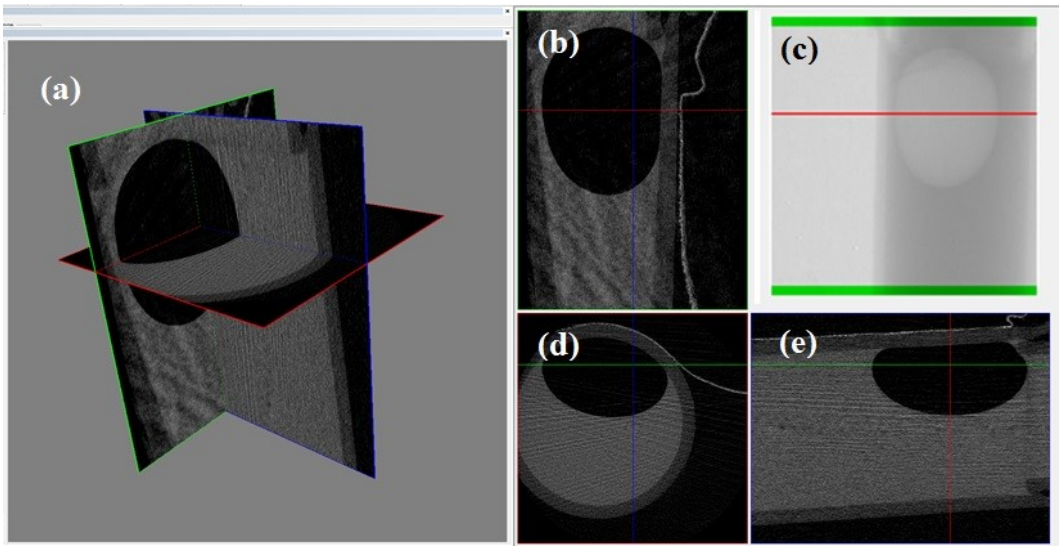

Figure 15. Three dimensional reconstructed micro CT images of the air-water calibration phantom displayed in Skyscan® Data Viewer. (a) combined view of all planes (b) x-plane (c) original micro CT image (d) z-plane (e) y-plane.

Two exposure settings (4712 ms and 8246 ms) were automatically chosen by the instrument to fit a suitable attenuation. Attenuation is a measure of how easily the material is penetrated by the X-ray (radiodensity) and is a function of X-ray energy and the density and composition of the material being scanned. A higher attenuation coefficient corresponds to a denser material and a lighter grey scale value. Since two exposure settings were used, two bone mineral density phantoms with BMD values of 250 and 750 were scanned at the different exposures for calibration. One air/water phantom was also scanned at 4712 ms for cross calibration. Filter cake scans were calibrated with the BMD phantoms by calibrating the attenuation coefficient with the known BMD values, and one MFT filter cake was cross calibrated with the air/water phantom by calibrating the grey scale values with Hounsfield Units (HU). A HU is another unit for radiodensity and is a linear transformation of the attenuation coefficients. At standard

temperature and pressure, water has a radiodensity of 0 HU and air has a radiodensity of -1000 HU. No difference was found between the calibration methods.

Analysis was carried out with vendor supplied bone morphometric software (Skyscan® CTAn and CTVol). Cylindrical volumes of interest (VOI's) for all samples were chosen to be 20.7 mm^3 with diameters of 3 mm. VOI's were also carefully selected to omit any ring artifact. The corruption of images by artifacts is difficult to avoid at high resolution, and reducing or removing such interferences would inhibit quantitative analysis post processing (Sijbers & Postnov, 2004). De-speckling is typically applied to images for smoothening, however it was not applied in these scans since the estimated pore size was close to the limit of resolution.

3.9.2 Binary Segmentation and Threshold Assignment

The reconstructed images contain 256 grey scale values from 0 to 255. For morphometric analysis, a binarised image is needed. Through segmentation, a pixel is either assigned a binary value of 0 (black) or 1 (white). Black pixels represent voids and white pixels represent objects. For segmentation, a threshold value must be assigned. Pixels with grey scale values greater than the threshold become white and pixels with grey scale values less than the threshold become black. Typically, a contrast fluid or agent is used when preparing samples whose structures are close to the limit of resolution, densities are close, or the attenuation of the phases to be distinguished are similar. The contrast fluid aids in the segmentation process. In

these scans, all three of the aforementioned issues were applicable, with the pore sizes hovering around 10 µm in diameter, the bitumen and water having a similar density, and having scans where the attenuation range being narrow. In this case, the threshold to distinguish pores and solids were assigned manually based on three considerations; large differences (>5) between grey scale units of neighboring pixels, grey scale histogram patterning across profiles of slices, and visual identification of pores and matching to grey scale values. Figure 16 shows the binary segmentation of a MFT filter cake scan. In depth description and calculation of threshold assignments is covered in Appendix B.

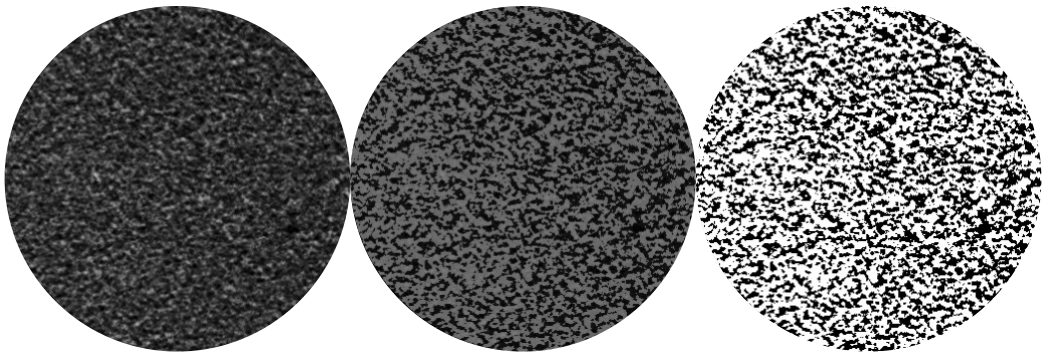

Figure 16. Application of binary threshold to filter cake of MFT treated with 1000 g/t A3335 + 3000 g/t Alcomer 7115. (a) original grey scale reconstructed image (b) overlay of binary image on original image (c) binary image where black represents the pores and white represents the solids.

Grey scale value histograms were calculated from the dataset averages rather than individual images. Porosity results were calculated from 3D analysis since 2D analysis of each slice independently greatly overestimated the closed porosity values and did not represent pore connectivity. A closed pore is defined as a connected assemblage of black voxels (the 3D depiction of a pixel) that is fully

surrounded on all sides by white voxels (solid object). In contrast, an open pore is defined as space within a solid object or between solid objects that has any connection in 3D to the space outside the object. Figure 17 shows how a void might appear as a closed pore in 2D (right), but considering 3D arrangement the "closed" pore is in fact connected to additional void outside of the object.

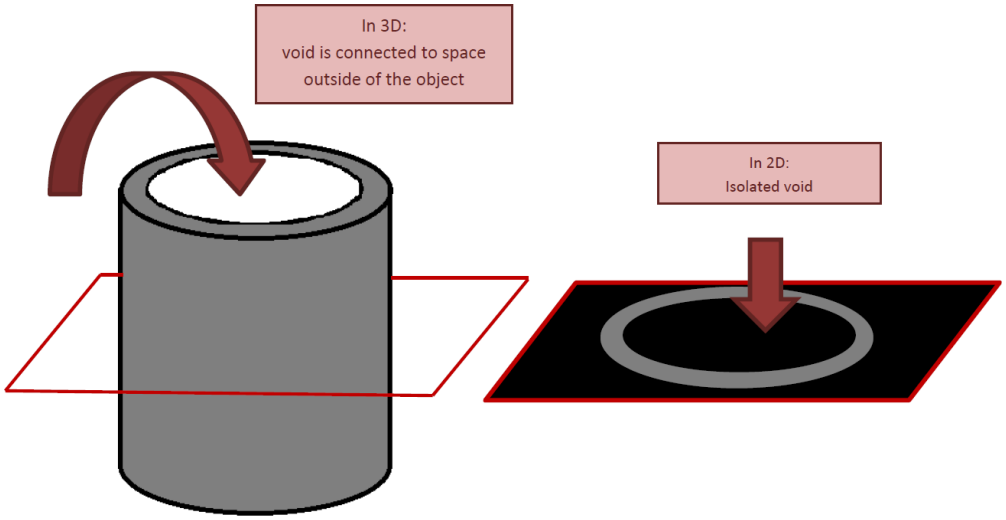

Figure 17. Schematic showing that a closed pore in 2D space cannot be assumed closed in 3D space.

3.10 Mixing Considerations

The incorporation of a viscous high molecular weight polymer solution into MFT poses challenges. The polymer solution must be evenly distributed in the dense slurry without being over-sheared. It has been noted that the flocculation performance of high molecular weight PAMs and PEOs is influenced by the amount of shear that the polymers are exposed to (Mpofu *et al.*, 2003; Neelakantan, 2016; McFarlane *et al.*, 2005). It would be beneficial to estimate and optimize the

mixing behavior and energy dissipation within the system for experimental design and scale-up.

The simulation and experimental study of dispersed solid multiphase flow in stirred tanks has been investigated over the years, however little work has been done on concentrated slurries with very fine particles. Furthermore, the inclusion of a viscous tertiary phase has not yet been simulated even though such scenarios are prevalent in areas such as water treatment, mineral processing, and personal/home care products.

A numerical approach based on computation fluid dynamics (CFD) principles was considered in this work. Direct comparisons to experimental data could not be drawn however due to the complexity of the experimental system and the limitations of the numerical models and resources. Details of the simulation methods and model descriptions are outlined in Appendix E. The results of the simulations are also outlined in Appendix E.

4 RESULTS AND DISCUSSION

4.1 Mature Fine Tailings

4.1.1 CST Results

The CST results are reported in Figure 18. The MFT was treated by single and dual polymer treatments. All three dual polymer treatments yielded significantly shorter CSTs than single polymer treatments, signifying that the water in the treated MFT was more readily removable. The A3335 treatment alone gave a CST of 1716 s (± 168 s), and the CST was decreased to 407 s (± 27 s) for the A3335 + PEO pair and to 121 s (± 7 s) for the A3335 + Alcomer 7115 pair. The addition of PEO to Alcomer 7115 treated MFT decreased the CST from 1228 s (± 105 s) to 387 s (± 43 s). The untreated MFT had a CST of 3075 s (± 180 s).

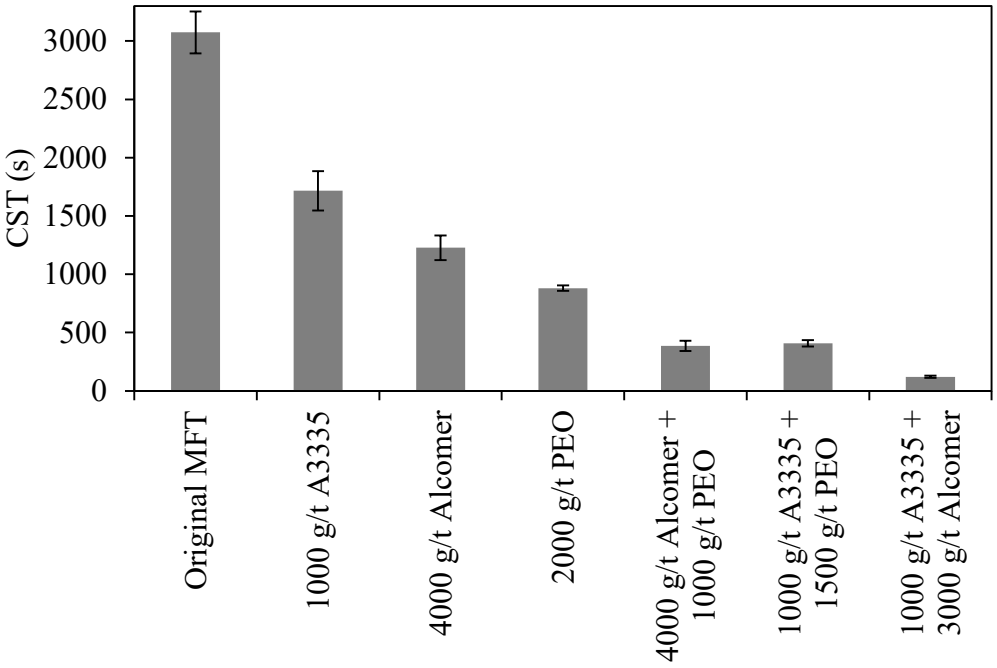

Figure 18. CST results of single and dual polymer treated MFT. The reported CST was the average of three measurements, and the standard deviation of the measurements ranged from 7 to 180 s, shown by the error bars in the diagram.

CST is often used as a quick predictor for ease of dewatering and as an indicator of filterability performance. Although it is a useful tool for quickly and cost-effectively assessing the potential filtration performance of a flocculant-treated slurry, there are other factors that affect the filterability of flocculated slurry that cannot be captured by CST. In MFT, residual bitumen exists between clay particles and it is suggested that the bitumen may migrate during filtration to clog pores and channels that water would otherwise be able to exit through (Klein, 2014). It is known that the floc strength varies depending on the polymer(s) used and thus it could be suggested that the pore strength may vary as a result (McFarlane *et al.*, 2005; Mpofu *et al*., 2003; Neelakantan, 2016). Depending on the filtration

technique used, hydraulic conductivity may not be maintained and the pores may undergo restructuring or collapse thereby hindering the water release.

4.1.2 Filter Cake Solids Content Results

Figure 19 displays the results of the final solids content of the filter cakes produced by the filter press. The results had good repeatability, with a standard deviation of 1.8 wt.% solids when performed on identical batches of MFT (see *Section 3.8* for standard deviation reporting). The filter press forms a solid cake when solids content exceeds 50 wt.%. Dual polymer treatment increased the final solids content of the cake in both the A3335 + PEO and A3335 + Alcomer 7115 cases in comparison to the single polymer treatment and the untreated MFT. Solid filter cakes were formed only when dual polymer treatment was used. It should be noted that all flocculated MFT had higher initial water content due to water introduced through polymer addition. The dual polymer treatment with A3335 + PEO yielded the highest final solids content of 60 wt.%, yet it is interesting to note that it did not have the lowest CST (Fig. 18). Previously Zhu reported that with A3335 + Alcomer 7115, lower CST corresponded to better filterability and consequently higher final solids contents in the filter cake (Zhu, 2015). The discrepancy prompted the investigation into additional factors that affect the dewaterability of A3335 + PEO treated MFT.

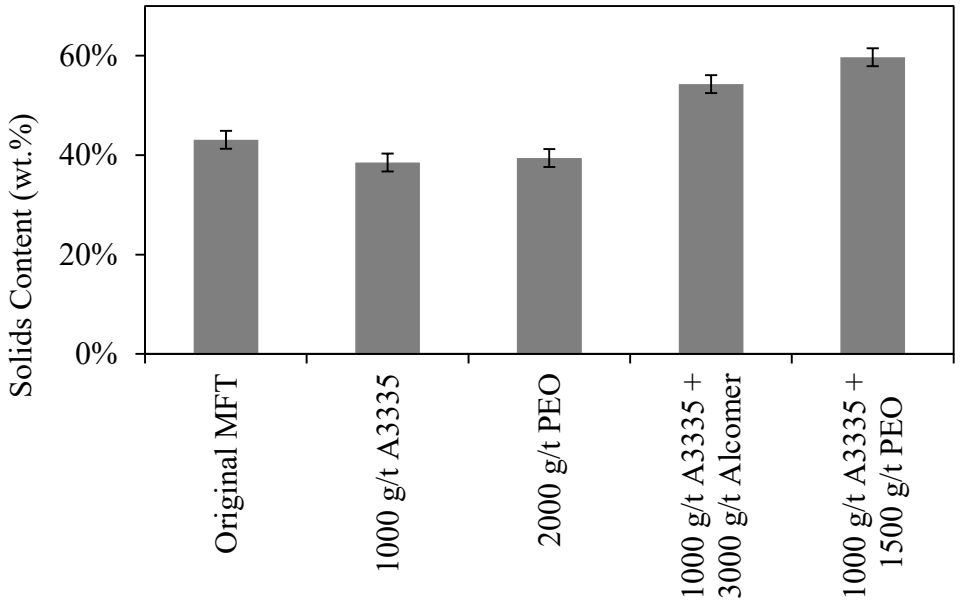

Figure 19. Final solids content of filter cakes produced from single and dual polymer treated MFT. Standard deviation of the filter cakes was 1.8 wt.% solids.[1]

4.1.3 Shear Effect on PAM and PEO flocculated MFT

It is known that PAM and PEO flocs respond to shear differently. The effect of shear energy on kaolinite flocculated with high molecular weight PEO and high molecular weight anionic PAM has been investigated (McFarlane *et al*., 2005; Mpofu *et al.*, 2003; Neelakantan, 2016). It is also known that the air diaphragm pump used to pump the polymer-treated MFT to the filter press plates and the transport through the hoses exposed the flocs to shear energy; however, it is unquantified. To assess the effect of shear imposed by the filter press operation itself, the treated MFT was preloaded onto plates before filtration for comparison.

[1] See *Section 3.8* on standard deviation reporting.

Figure 20 shows the filter cake solids content results obtained from the low and high shear tests.

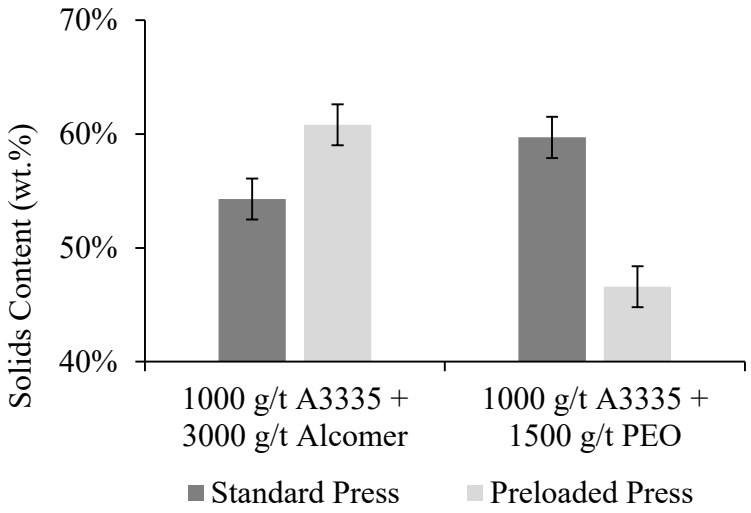

Figure 20. Comparison of final solids content of filter cakes produced from either low shear (preloaded plate) trials or high shear (standard press) trials. Standard deviation of the filter cakes was 1.8 wt.% solids.[1]

A3335 + Alcomer 7115 in lower shear tests produced higher filter cake solids content (61 wt.%) whereas A3335 + PEO in higher shear tests produced higher solids content (60 wt.%). The results shown in Figure 20 show that the exposure to the diaphragm pump does have an effect on the final solids content of the filter cake.

It has been reported that when kaolinite was flocculated with high molecular weight PAM, the flocs showed significant breakage when subjected to moderate shear. Under the same conditions, flocs produced from kaolinite dispersions flocculated with PEO underwent densification without breakage. It was further found that under high shear environments (1000 kJ/m^3), PEO flocs underwent

[1] See *Section 3.8* on standard deviation reporting.

densification as well as restructuring. PEO flocs increased dramatically in size and the volume of fine particles reduced as they bridged into larger flocs. Flocs break-down eventually resulted under excessive amounts of shear energy (7000 kJ/m^3) (Neelakantan, 2016). Flocs created with anionic PAM fragmented at lower shear (200 kJ/m^3), and the addition of a cationic polymer in a dual polymer treatment further lowered the tolerance of the flocs to shear energy (Neelakantan, 2016). It has also been reported that PEO has a much stronger dose dependence on yield stress than polyacrylamides. At doses of 500 g/t of PEO or more in 40 wt.% slurries of kaolinite, it was found that non-DLVO forces had become dominant and were responsible for the dramatic increases in yield stress (Mpofu *et al*., 2003). Structurally, PEO is completely linear and there is freedom of rotation about any axis as all the carbon and oxygen atoms are sp^3-hybridized, resulting in a highly elastic structure compared to polyacrylamides. This structure allows the polymer to re-conform more easily. Carboxylate and amide (-COO^- and -$CONH_2$ respectively) functional groups on polyacrylamides are sp^2-hybridized so there is no freedom to rotate about carbon-oxygen and/or carbon-nitrogen bonds due to electron delocalization thus fixing them in a plane and making them somewhat "bulky" (Bruice, 2012).

Additionally, the CST was measured for the flocculated MFT before and after pumping through the diaphragm pump on the filter press. Figure 21 shows that MFT flocculated with A3335 + PEO produced shorter CST after being pumped whereas MFT flocculated with A3335 + Alcomer 7115 produced better CST before being pumped.

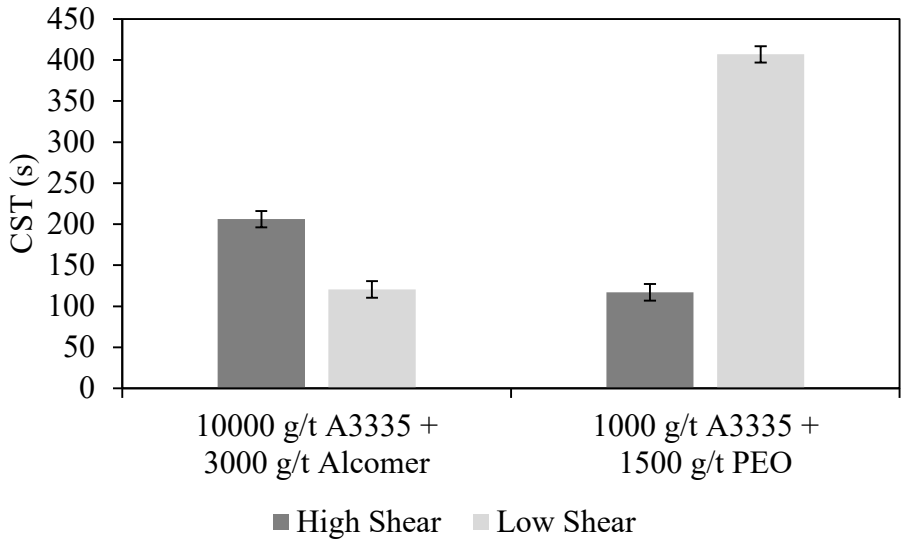

Figure 21. Comparison of CST results of flocculated MFT exposed to either high shear (after pump) or low shear (before pump) (n=3, s=10 s).

The MFT treated with A3335 + PEO benefited from additional shear whereas the MFT treated with A3335 + Alcomer 7115 suffered from the additional shear.

It is estimated through simplified mixing equations (9) and (10) that the shear energy applied through mixing when the polymers were originally added to the MFT was approximately 130 kJ/m^3:

$$P = \rho \times N_P \times N^3 \times D^5 \tag{9}$$

$$E = \frac{P \times t}{V} \tag{10}$$

where power P (W) is a function of slurry density ρ (1230 kg/m^3), impeller power number N_P (PBT = 1.27), impeller speed N (5 s^{-1}), and impeller diameter D (0.1 m). Mixing energy E (J/m^3), is a function of power and time t (45 s), normalized by volume V (6.8×10^{-4} m^3).

4.1.4 Filtration Results

Net water release (NWR) results were obtained and are shown in Figure 22. All dual polymer treatments have an initial negative NWR due to water added through polymer addition. The absolute water release rate was also calculated as shown in Figure 23.

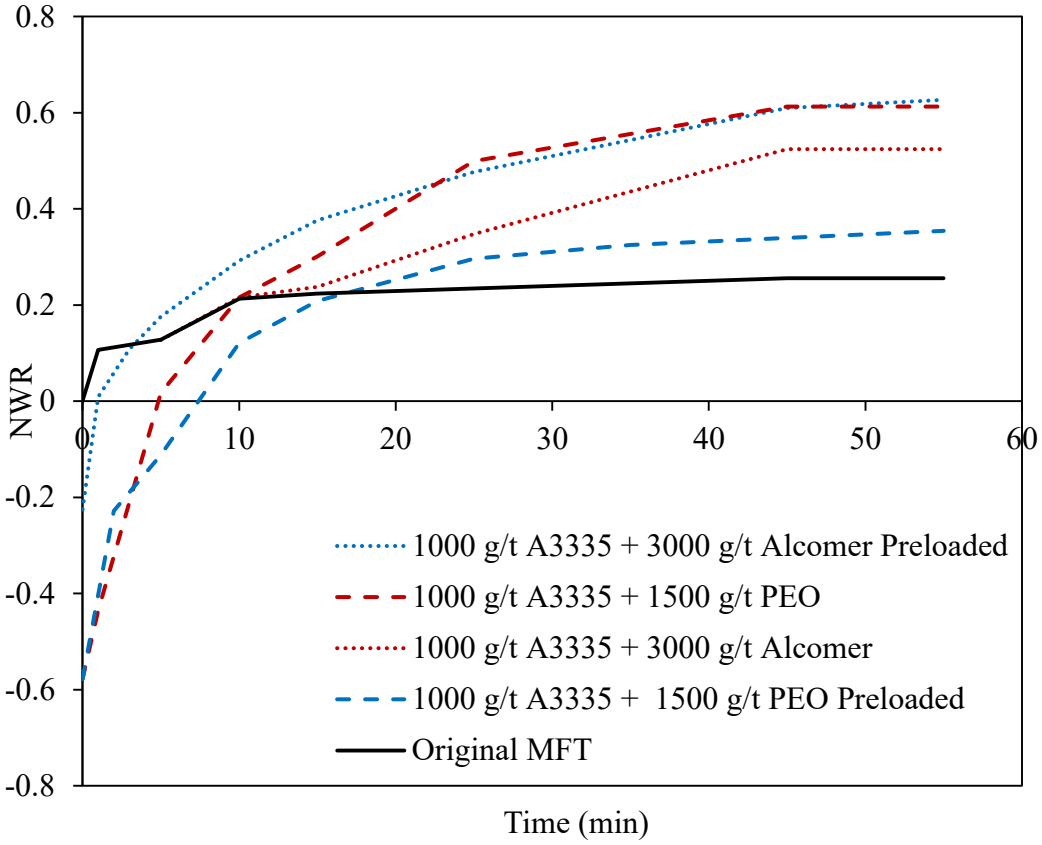

Figure 22. Net water release (NWR) from various dual polymer treatments of MFT.

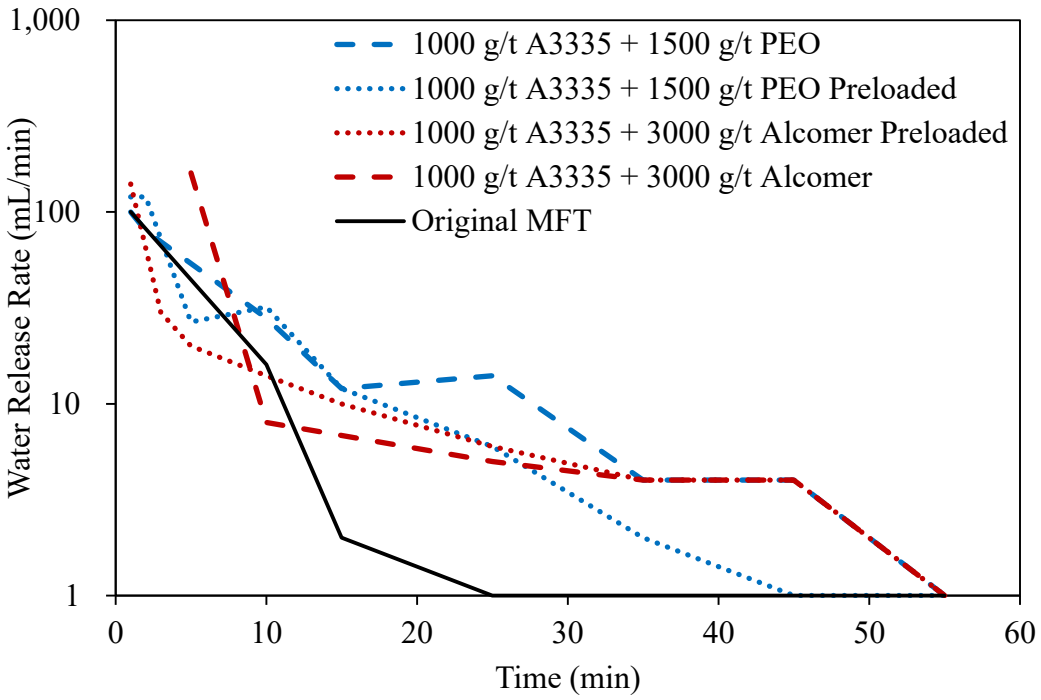

Figure 23. Water release rate from various dual polymer treatments of MFT.

The best NWR results were observed with the A3335 + Alcomer 7115 treatments preloaded, and the A3335 + PEO treatment under standard filter press operation. The A3335 + PEO flocculated MFT preloaded into the filter press plates performed the poorest in dewatering. This coincides with the solids content results (Fig. 19 and 20) achieved by the treatments.

The A3335 + PEO flocculated MFT (run under standard and preloaded filter press conditions) showed the fastest initial water release rates in the first ten minutes of filtration. This can be rationalized by the fact that more water was added with the PEO solution (0.2 wt.% stock) than the Alcomer 7115 solution (2 wt.% stock). After 35 minutes however, the water release rates for all tests except for the preloaded A3335 + PEO treatment and untreated MFT were equal. At this point, the preloaded A3335 + PEO test had the second lowest water release rate and the

untreated MFT had the lowest water release rate. This supports the final solids content results shown in Figures 19 and 20 where A3335 + PEO preloaded had a filter cake solids content of 46.6 wt.% and the untreated MFT had a filter cake solids content of 43.1 wt.%.

The initial specific resistance to filtration (SRF) was calculated based on the Darcy's equation outlined in *Section 2.4*. Since the SRF can be calculated by taking the slope of the *t/V* vs *V* profile, only the initial SRF could be calculated due to the loss of linearity as the filtration progressed. The initial SRF period is the first ten minutes of filtration. Possible causes for deviation from linearity are outlined in Figure 24.

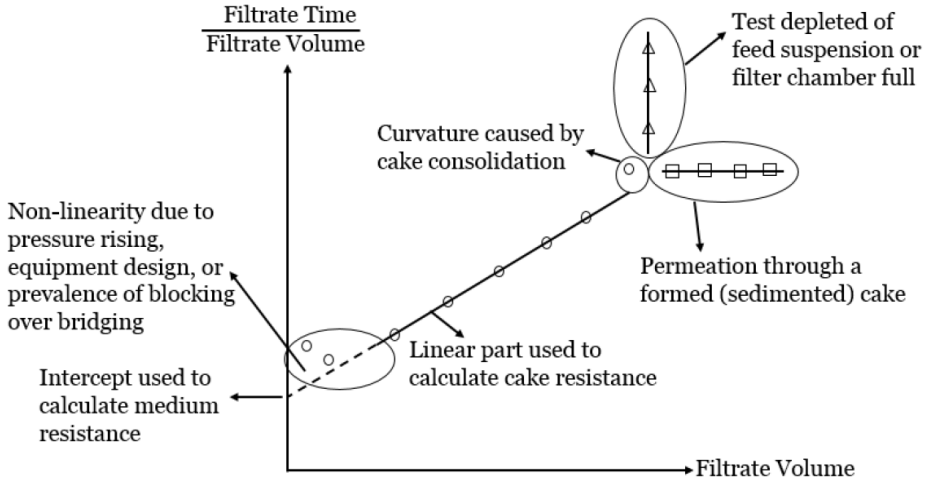

Figure 24. Possible causes for non-linearity in the *t/V* versus *V* plot (Tarleton & Wakeman, 2007).

The *t/V* versus *V* plot for MFT treated with 1000 g/t A3335 + 3000 g/t Alcomer 7115 preloaded into the filter press is shown in Figure 25 with the linear portion of the profile highlighted and trend line equation generated using Microsoft Excel. Similar plots were obtained for the other samples.

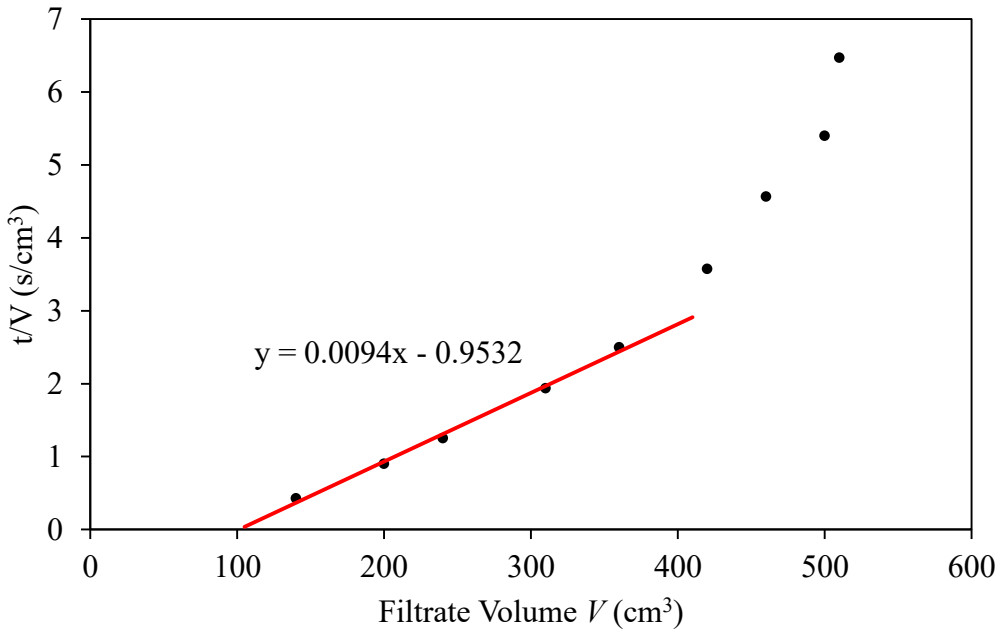

Figure 25. The *t/V* versus *V* plot for MFT treated with 1000 g/t A3335 + 3000 g/t Alcomer 7115 preloaded into the filter press.

The assumption was made that the initial filtration followed the cake filtration model, but in reality the t/V versus V plot reveals that the filtration process is likely a combination of cake filtration and blocking filtration (Fig. 12). It is also assumed that pressure acting on the filter plates was constant during the initial filtration period. The concentration *c* was calculated based on the mass definition (Equation 3) for each test. Given that the viscosity of the filtrate was 0.8937 mPa·s, the filtration area was 0.022 m^2, and the change in pressure was 519.2 kPa (620.5-101.3 kPa), the following SRF values were calculated as shown in Figure 26. Full calculations are presented in Appendix C.

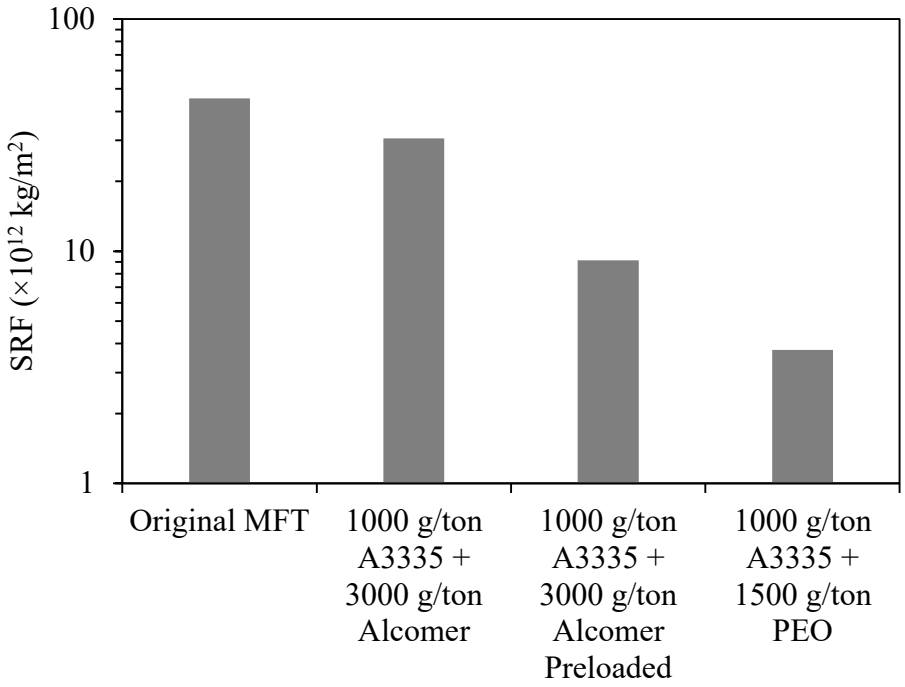

Figure 26. The specific resistance to filtration for MFT treated with 1000 g/t A3335 + 3000 g/t Alcomer 7115, and 1000 g/t A3335 and 1500 g/t PEO.

A lower SRF value corresponds to better filtration. The calculated SRF values correspond well to the CSTs, filter cake solids contents, and water release results. The MFT had the highest SRF value of 45.5×10^{12} kg/m^2, which correlates to the high CST result of 3075 s and low filter cake water release and solids content. The two lowest SRF values were for the MFT treated with the A3335 + Alcomer 7115 preloaded into the filter plates (9.1×10^{12} kg/m^2) and the MFT treated with the A3335 + PEO (3.8×10^{12} kg/m^2), which had the lowest CSTs and highest filter cake solids content water release results of all tests conducted in this work.

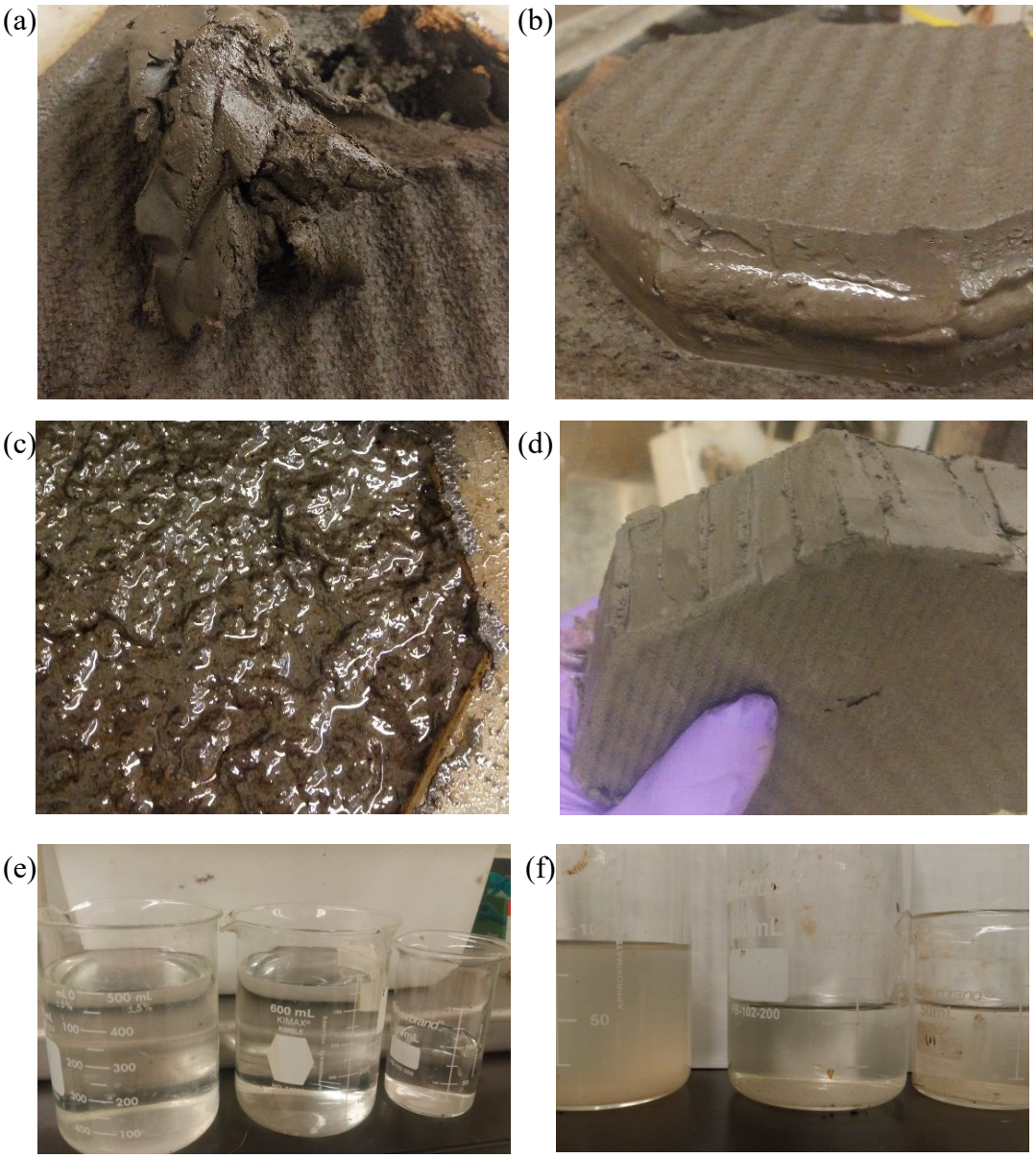

Figure 27. Filter cakes and filtrate from filter press tests: (a) Filter cake from MFT treated by 1000 g/t A3335 + 1500 g/t PEO. (b) Filter cake from MFT treated by 1000 g/t A3335 + 3000 g/t Alcomer 7115. (c) Filter cake from MFT treated by 1000 g/t A3335 + 1500 g/t PEO and preloaded to filter press. (d) Filter cake from MFT treated by 1000 g/t A3335 + 3000 g/t Alcomer 7115 and preloaded to filter press. (e) filtrates from dual polymer treatments (both A3335+Alcomer 7115 and A3335+PEO). (f) filtrates from untreated MFT.

Figure 27 shows the appearance of the filter cakes and filtrates obtained from the dual polymer treatment of MFT. The A3335 + PEO treated MFT filtered under

standard filter press conditions and the A3335 + Alcomer 7115 treated MFT filtered on preloaded plates both produced solid cakes (Fig. 27a and 27d). The A3335 + Alcomer 7115 treated MFT filtered under standard filter press conditions produced a non-homogeneous cake that was wet in the middle (Fig. 26b). The A3335 + PEO treated MFT filtered on preloaded plates was not able to produce a solid cake and the flocs appeared relatively unchanged after an hour of filtration (Fig. 27c). This result supports the poor solids content, NWR and water release rate observed (Fig. 21, 22 and 23). Filter press filtration of dual polymer treated MFT produced filtrates of better clarity than untreated MFT (compare Figs. 27e and 27f). This is attributed to better fines capture during flocculation through the polymer bridging of fine particles.

4.2 Kaolinite

Two kaolinite samples, BASF ASP 600 ($D_v(90)$ = 13.5 μm) and BASF ASP 802 ($D_v(90)$ = 22.7 μm) were tested and compared to represent a simplified and ideal clay system with respect to MFT.

4.2.1 CST Results

The CSTs of the treated and untreated ASP 600 and ASP 802 kaolinite are reported in Figure 28. The finer ASP 600 kaolinite produced shorter CST times in all of the tests.

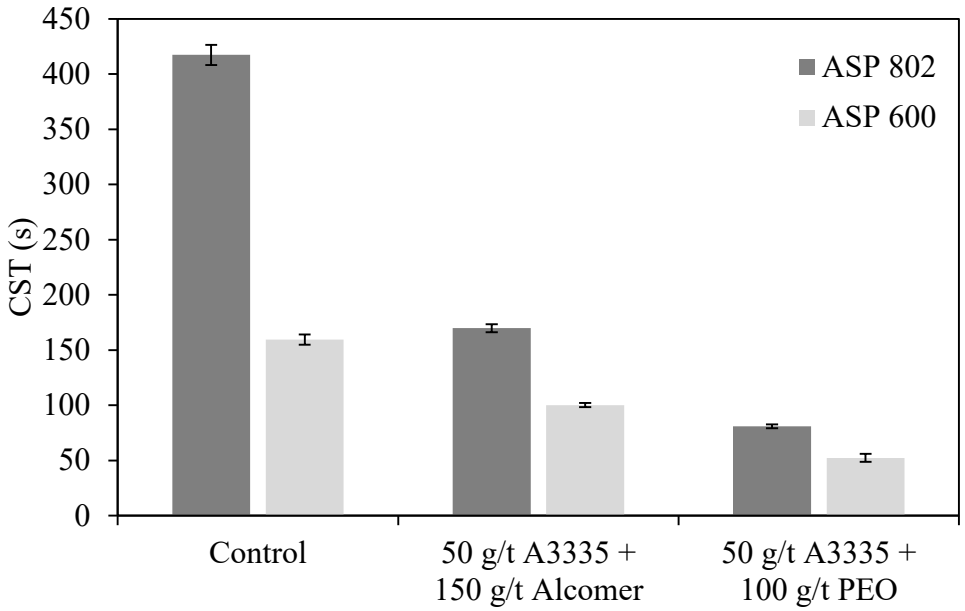

Figure 28. CST results of untreated (control) and dual polymer treated kaolinite. All tests repeated in triplicates, and the standard deviation ranged from 2 to 13 s.

In comparison to the untreated MFT (CST = 3075±180 s), both of the untreated kaolinite slurries had CST values an order of magnitude less (ASP 802 CST = 417±9 s, ASP 602 CST = 159±5 s). Kaolinite treated with the optimal dosage of polymers had comparable CST values to that of MFT treated with the polymers at a higher dosage. In both the MFT and the kaolinite, the dual polymer treatment with A3335 and PEO yielded lower CST values than the A3335 and Alcomer 7115.

4.2.2 Filter Cake Solids Content Results

The solids content results for ASP 600 and ASP 802 kaolinite are reported in Figure 29.

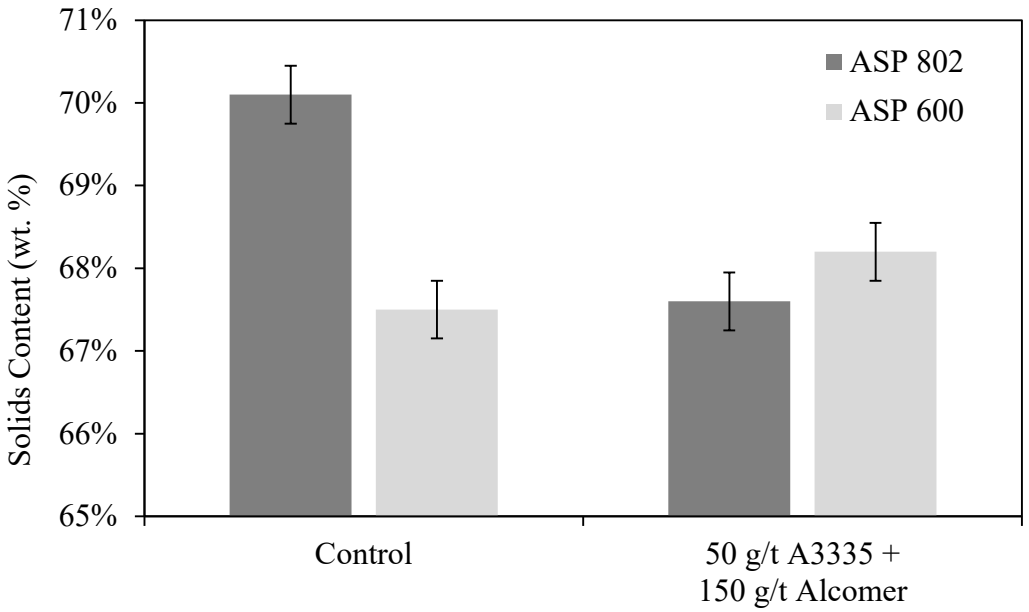

Figure 29. Comparison of cake solids content results of the two different kaolinite samples untreated (control) and treated with dual polymers. Standard deviation of the filter cakes was 0.35 wt.% solids.[1]

Without the use of polymer flocculants, the filter cake of ASP 802 kaolinite contained higher final solids content after filter press filtration than the ASP 600 kaolinite (solid content was 70.1±0.35% for ASP 802 and 67.5±0.35% for ASP 600. The addition of polymer however only improved the final cake solids content with the ASP 600 kaolinite (68.2±0.35%). Interestingly the cake produced from the untreated ASP 802 kaolinite seemed to exhibit "thinning" behavior over time: the cake appeared to be solid upon removal from the filter press, however once the cake was left to stand, it lost the rigid structure and "melted" as shown in Figure 30. This could be attributed to the coarser particle sizes of the ASP 802 kaolinite.

[1] See *Section 3.8* on standard deviation reporting.

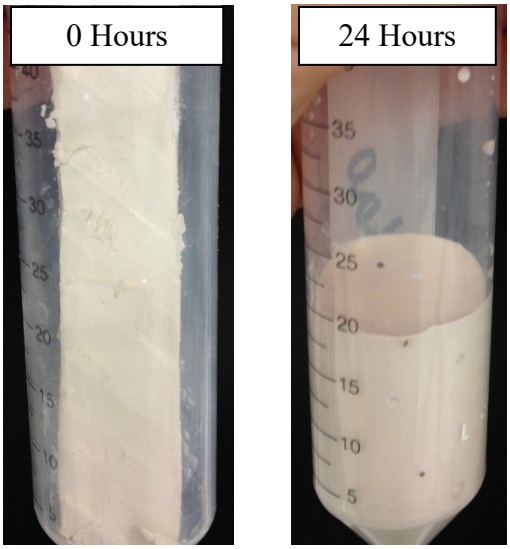

(a) (b)

Figure 30. (a) Untreated ASP 802 kaolinite cake as taken immediately from the filter press (b) untreated ASP 802 kaolinite cake left overnight.

When the ASP 802 kaolinite was treated with 50 g/t A3335 and 150 g/t Alcomer 7115 the cake was able to maintain its structure, however it resulted in a lower solids content (67.6±0.35%) than the untreated ASP 802 kaolinite. Due to this behaviour, the ASP 600 kaolinite was selected for further filtration tests. Figure 31 reports the solids content results of ASP 600 kaolinite treated with the same polymer dosages that were used on MFT (i.e., higher dosages than reported in Figure 29). From the filter cake solids content results shown in Figure 31, it is apparent that the overdosing had an adverse effect.

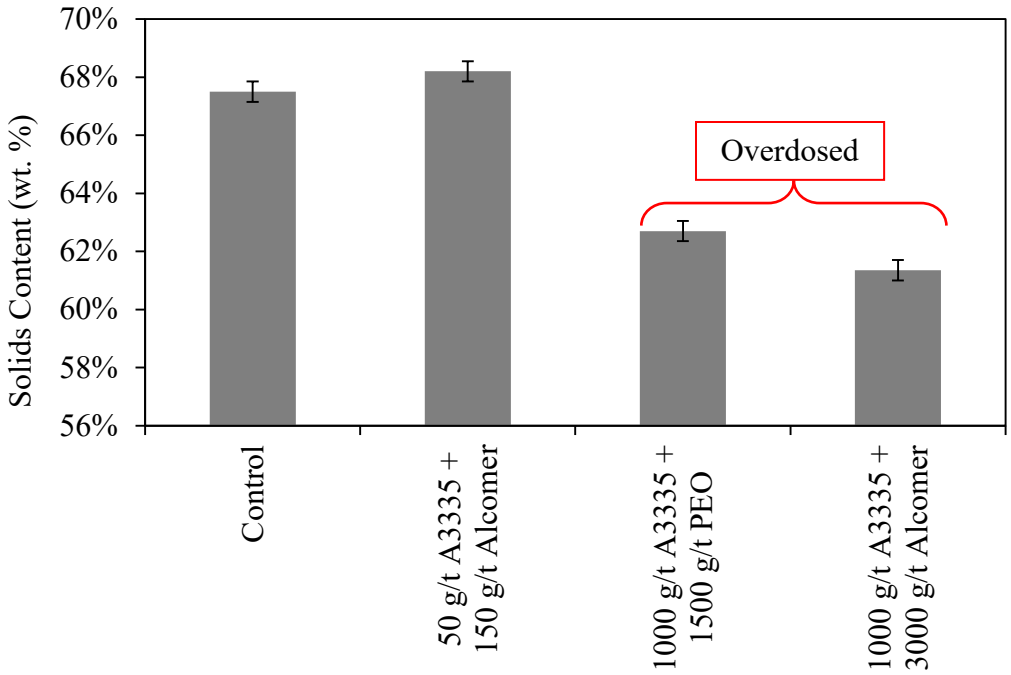

Figure 31. Cake solids content results of untreated (control) and dual polymer treated ASP 600 kaolinite (n=3, s=0.35%). Standard deviation of the filter cakes was 0.35 wt.% solids.[1]

4.2.3 Water Release

The NWR and absolute water release rates for ASP 600 kaolinite are reported in Figures 32 and 33, respectively. After one hour the overdosed kaolinite treated with 1000 g/t A3335 + 3000 g/t Alcomer 7115 resulted in the lowest NWR and the untreated kaolinite resulted in the highest NWR. It should be noted that after one hour however, the water release rate for the untreated kaolinite had reached 0 mL/min whereas the kaolinite treated with the ideal concentration of polymers (50 g/t A3335 + 150 g/t Alcomer) still had a water release rate of 3.3 mL/min. This suggests that with a filtration time longer than one hour, the final solids content of

[1] See *Section 3.8* on standard deviation reporting.

the kaolinite treated with the ideal dosage of polymer would achieve a final solids content greater than the untreated kaolinite.

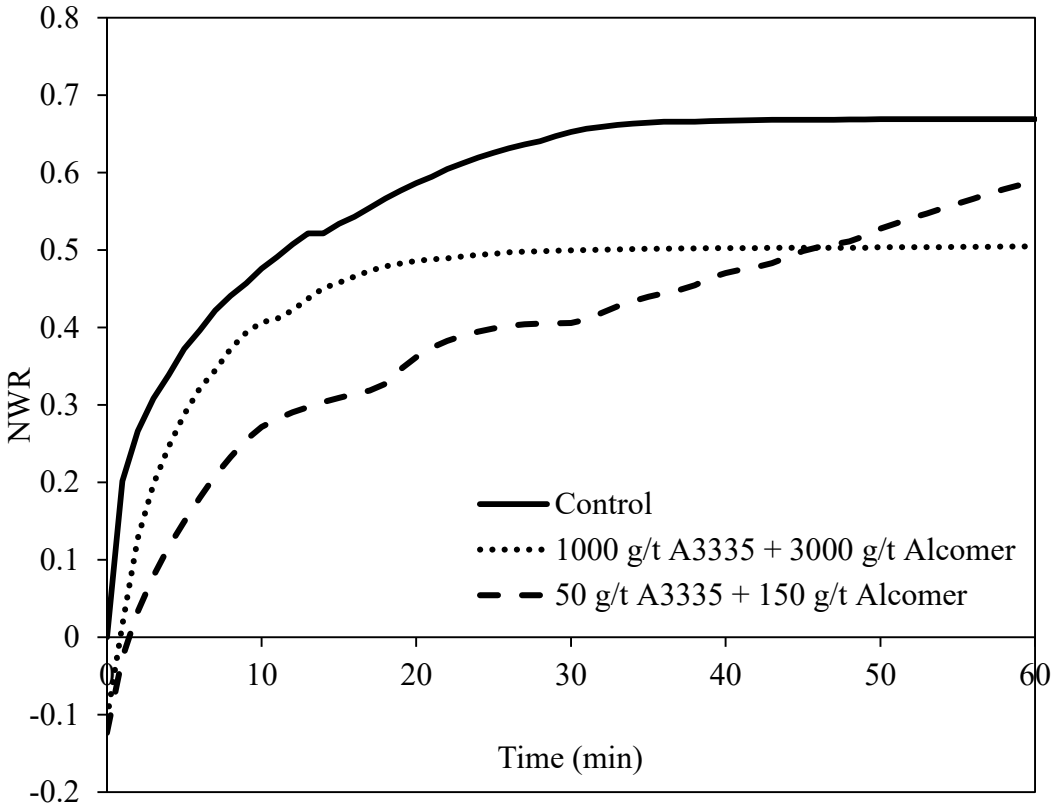

Figure 32. Comparison of net water release results of the treated and untreated (control) ASP 600 kaolinite samples.

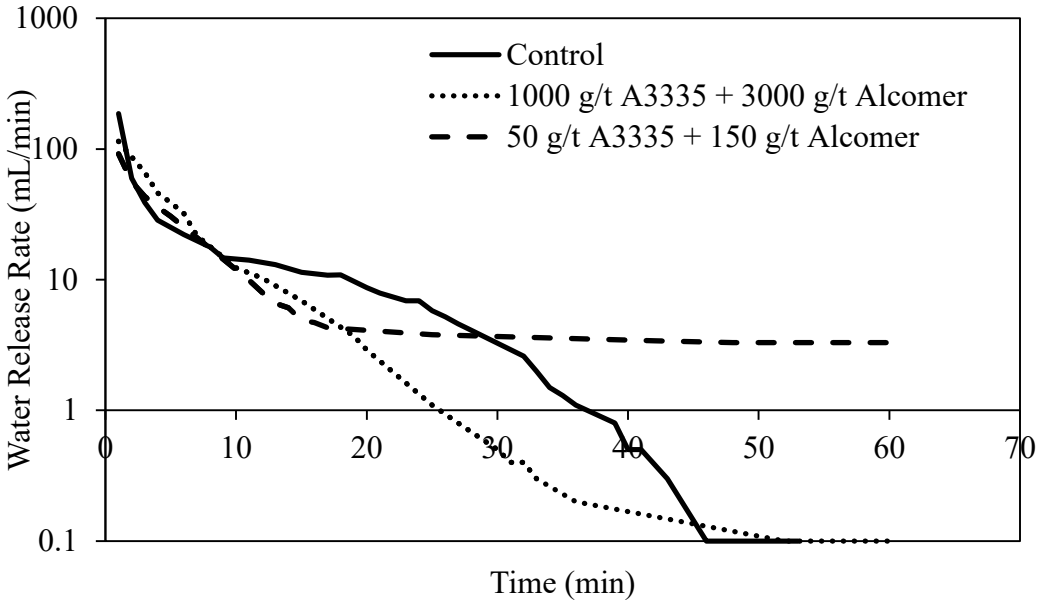

Figure 33. Comparison of absolute water release rates of treated and untreated (control) ASP 600 kaolinite samples.

The calculated initial SRF values for ASP 600 kaolinite are reported in Figure 34. The initial SRF period is in the first ten minutes of filtration.

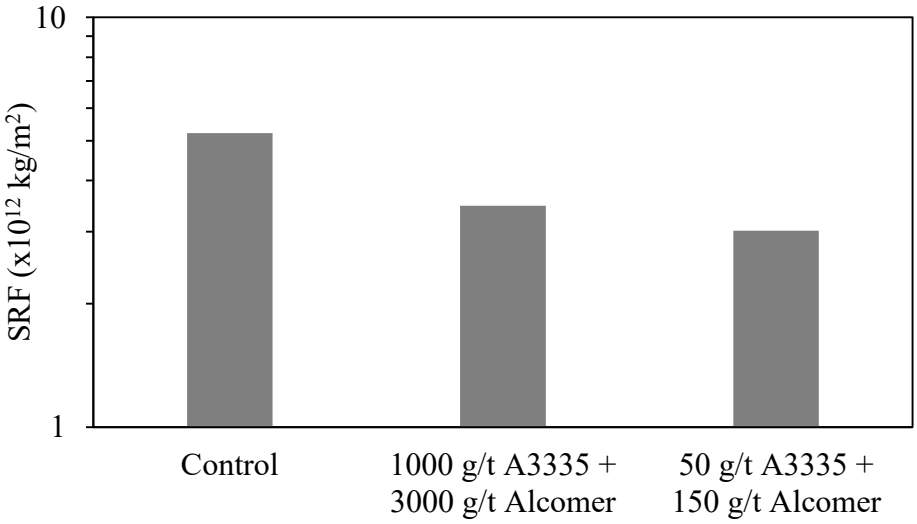

Figure 34. Comparison of initial specific resistance to filtration of treated and untreated (control) ASP 600 kaolinite samples.

The higher initial SRF for the untreated kaolinite (5.2×10^{12} kg/m^2) corresponds to the lower filter cake solids content and high CST values that were observed. The kaolinite treated with either the low optimal dosage of polymer or the overdosed high dosage resulted in similar initial SRF values (3.0×10^{12} and 3.5×10^{12} kg/m^2) considering SRF values are typically compared on an order of magnitude difference. Although both the high and low dosages of A3335 + Alcomer 7115 resulted in similar SRF values, the lower dosage of polymer produced a *t/V* versus *V* plot that maintained a shallower slope over a longer period of time than the higher dosage of polymer (Figure 35).

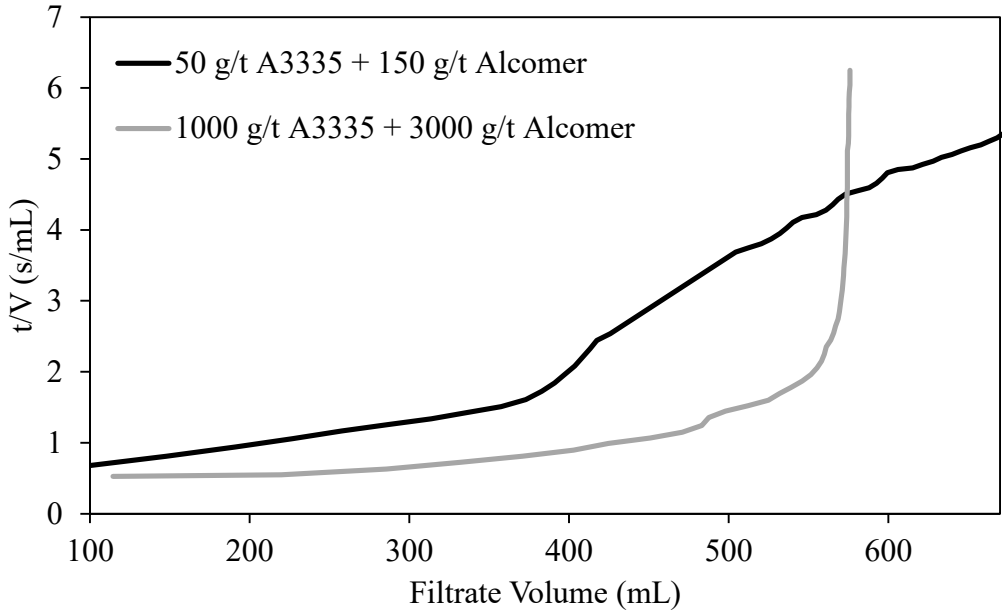

Figure 35. Comparison of *t/V* versus *V* profiles for the different dosages of polymer on ASP 600 kaolinite.

This helps explain why the NWR for the kaolinite treated with 50 g/t A3335 + 150 g/t Alcomer 7115 observed in Figure 32 continues to increase past the 60-minute mark rather than leveling off as with the other two tests, and its higher water release rate as seen in Figure 33.

4.3 Kaolinite Mixed with 3 wt.% Bitumen (Kaolinite/Bitumen)

The polymer pair of A3335 and Alcomer 7115 was selected for the kaolinite/bitumen tests since this pair produced more consistent results than the A3335 and PEO pair. The ASP 600 kaolinite was chosen for the kaolinite/bitumen slurry due to the explanation provided in Section 4.2.2.

4.3.1 CST Results

The CST results of treated and untreated kaolinite/bitumen samples are reported in Figure 36 together with the CST values for MFT and kaolinite.

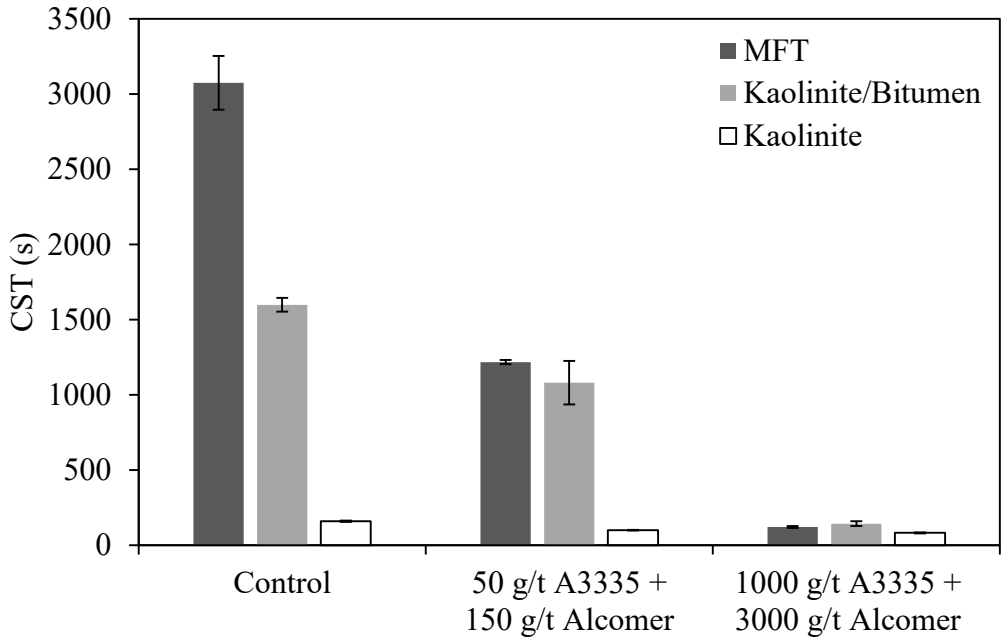

Figure 36. CST comparisons between dual polymer treated and untreated kaolinite/bitumen and previous MFT and kaolinite. The reported values were averages of triplicates and the standard deviation ranged from 2 to 180 s.

Untreated kaolinite/bitumen sample had a much higher CST (1600±46 s) than the kaolinite alone (159±5 s) but was less than the MFT (3075±180 s). When kaolinite/bitumen was treated with the low dosage of polymers that was used on the kaolinite, it responded poorly (1080±145 s) and similarly to MFT treated with the same dosage (1220±14 s). The kaolinite/bitumen had short CST times (142±16 s) comparable to the MFT when treated with the higher dosage of A3335 + Alcomer 7115 (121±7 s). Although overdosed, it is expected that kaolinite treated with the higher dosage of A3335 + Alcomer 7115 would also yield a short CST (82±3 s) as reported earlier in this thesis.

4.3.2 Filter Cake Solids Content Results

The solid contents in the filter cakes generated from the treated and untreated kaolinite/bitumen samples are reported in Figure 37 together with MFT and kaolinite.

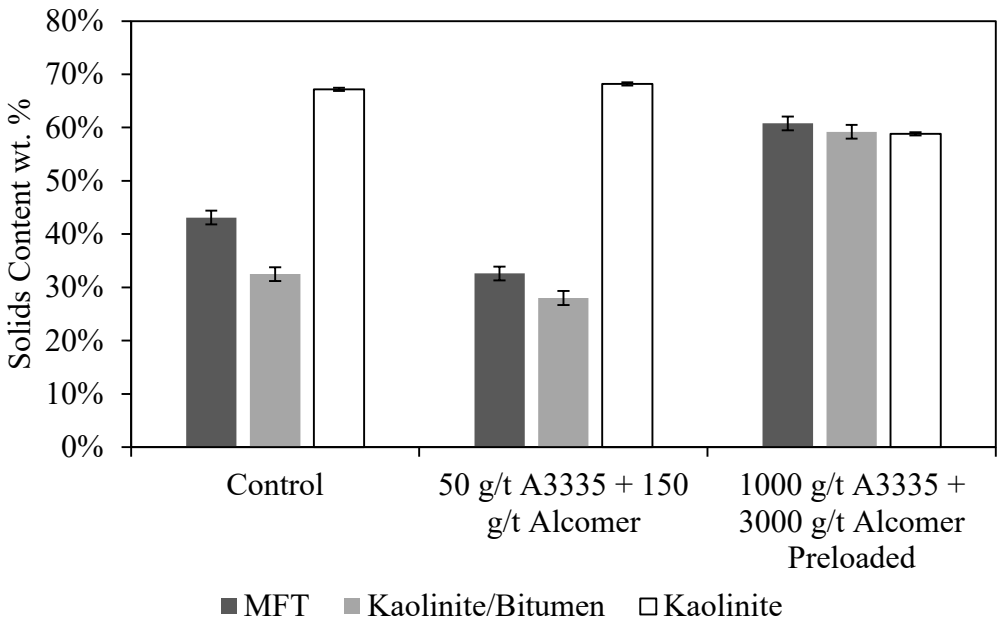

Figure 37. Comparison of final solids content of filter cakes produced from either MFT, kaolinite/bitumen mixture, or pure kaolinite. Standard deviation of the MFT and kaolinite/bitumen filter cakes was 1.8 wt.% solids and the standard deviation of the kaolinite filter cakes was 0.35 wt.% solids.[1]

With the filter press, a cake is formed at a solids content of just over 50 wt.%. The kaolinite/bitumen behaved similar to the MFT in the filter press tests in that only the kaolinite/bitumen treated with 1000 g/t A3335 + 3000 g/t Alcomer 7115 was able to form a cake (59.2±1.8 wt.%). Although a similar trend was observed between the kaolinite/bitumen and MFT, overall the kaolinite/bitumen performed slightly poorer in terms of final solids content results despite having shorter CSTs (see Figure 36).

[1] See *Section 3.8* on standard deviation reporting.

4.3.3 Water Release

The NWR and absolute water release rate of kaolinite/bitumen treated with 1000 g/t A3335 + 3000 g/t Alcomer 7115 is compared against similar treatments on MFT and kaolinite in Figures 38 and 39.

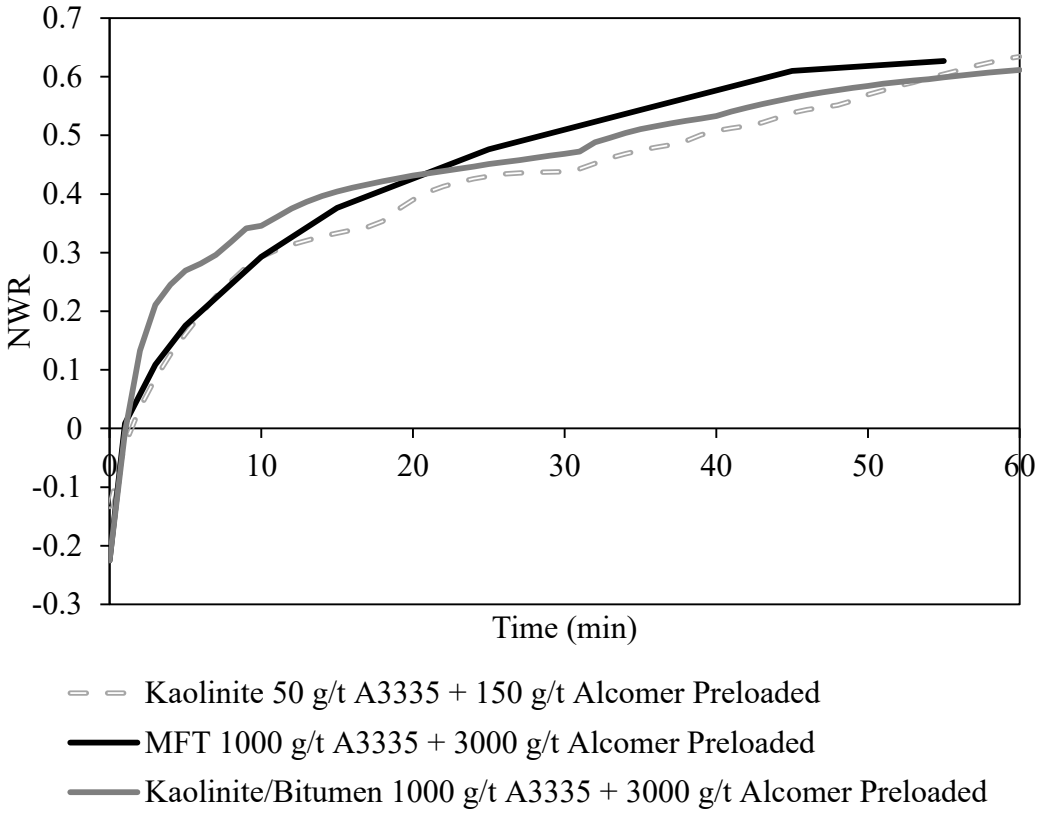

Figure 38. Comparison of NWR for different slurries treated with A3335 and Alcomer 7115.

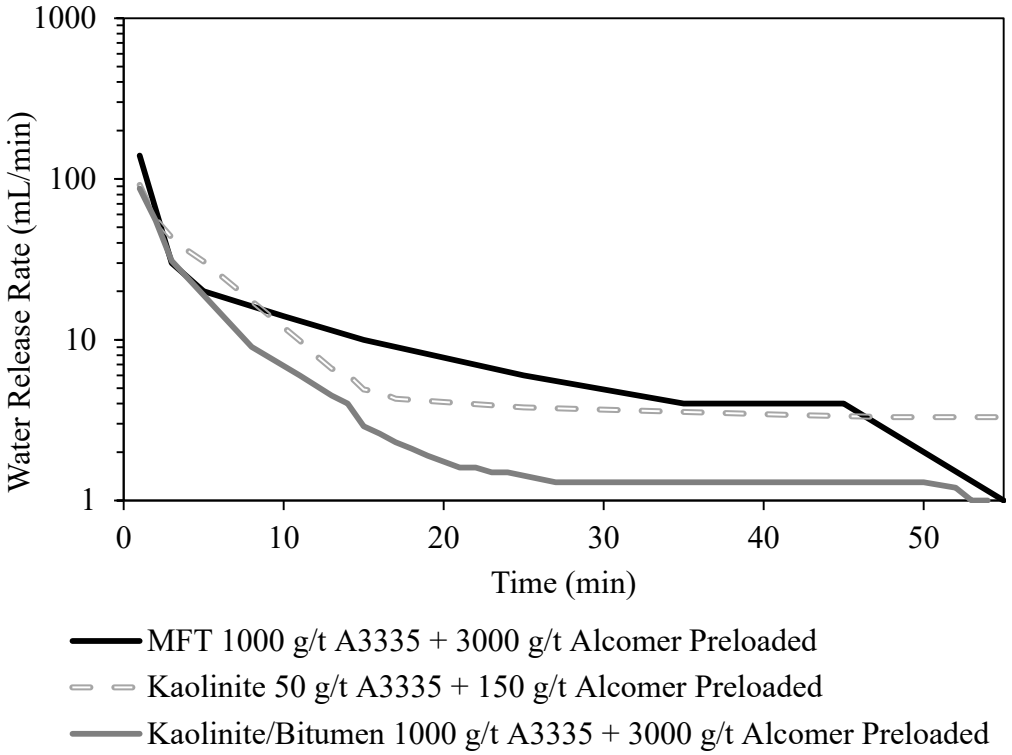

Figure 39. Comparison of absolute water release rates for different slurries treated with A3335 and Alcomer 7115.

The NWR behavior of the three slurries are similar when treated with the optimal dosage of polymer. This corresponds well to the solids content results that are reported in Figure 37. The water release rate data also correlates well with the solids content results since the kaolinite/bitumen treated with the A3335 + Alcomer 7115 had both the lowest water release rate and solids content in the filter cake.

The initial SRF for the kaolinite/bitumen treated with 1000 g/t A3335 + 3000 g/t Alcomer 7115 is compared against similar treatments with MFT and kaolinite in Figure 40.

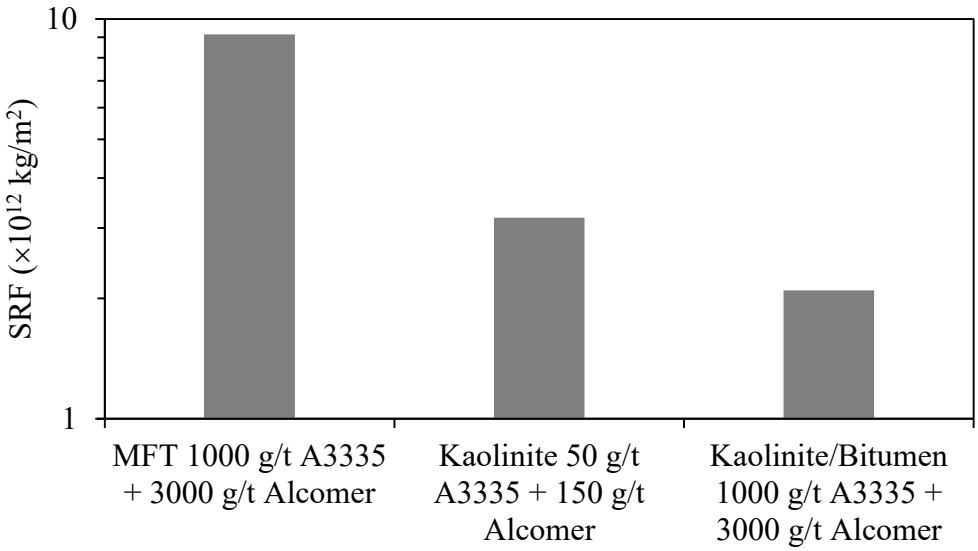

Figure 40. Comparison of SRF values for different slurries treated with A3335 and Alcomer 7115.

The kaolinite/bitumen treated with A3335 + Alcomer 7115 produced an SRF on the same order of magnitude as both the MFT and kaolinite treated with A3335 + Alcomer 7115.

Accurate filtrate data could not be obtained for the untreated kaolinite/bitumen slurry. It was observed that with the absence of polymers two phenomena happened. Firstly, when the filter plates were opened up, there was a noticeable amount of bitumen adhered to the filter cloth when the kaolinite/bitumen slurry was untreated. If the kaolinite/bitumen slurry was treated with the high dosage of polymers, then the filter cloth appeared quite clean with no noticeable bitumen. The appearance of the filter cloths is shown in Figure 41.

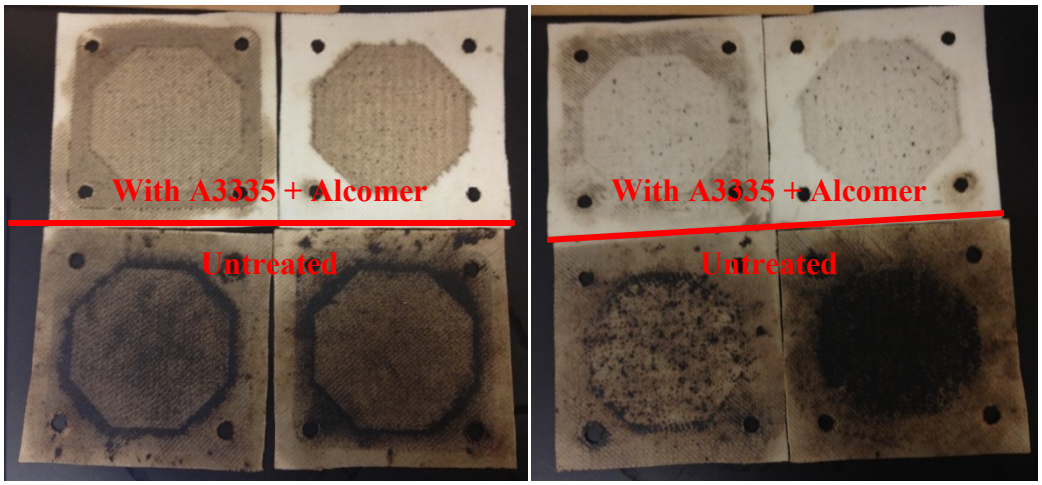

(a) (b)

Figure 41. Visual comparison between filter cloths. The top cloths are from the kaolinite/bitumen slurry treated with A3335 + Alcomer 7115 and the bottom cloths are from the untreated kaolinite/bitumen. (a) inside surface, and (b) outside surface

It is hypothesized that the added A3335 + Alcomer 7115 may interact with the bitumen and assist in preventing the bitumen from binding to the filter cloth. It is likely that this is observed more clearly with the kaolinite/bitumen slurry than with the MFT since although the kaolinite/bitumen slurry is homogenized, the bitumen may not be as well dispersed as with the MFT or coated on the clay surface as in MFT.

The second observation was that in the absence of polymers, the filtrate had a very high solids content of 30 wt.%. The filter cloth is a woven polypropylene mesh that can filter down to 15 µm. With flocculated kaolinite, MFT, or kaolinite/bitumen, the mesh size of the filter cloth is sufficient to block the flocculated solids resulting in clean filtrate. With the untreated MFT or kaolinite, the combination of cake filtration and blocking filtration allows small amounts of solids to enter the filtrate but it blocks further solids from passing through as the

filtration progresses. It is hypothesized that with the untreated kaolinite/bitumen, the particles are dispersed by the anionic species in the process water introduced with the residual bitumen, such that the particle layer deposited on the filter cloth is not sufficient to prevent solids from entering the filtrate. Figure 42 compares the filtrates from the various tests.

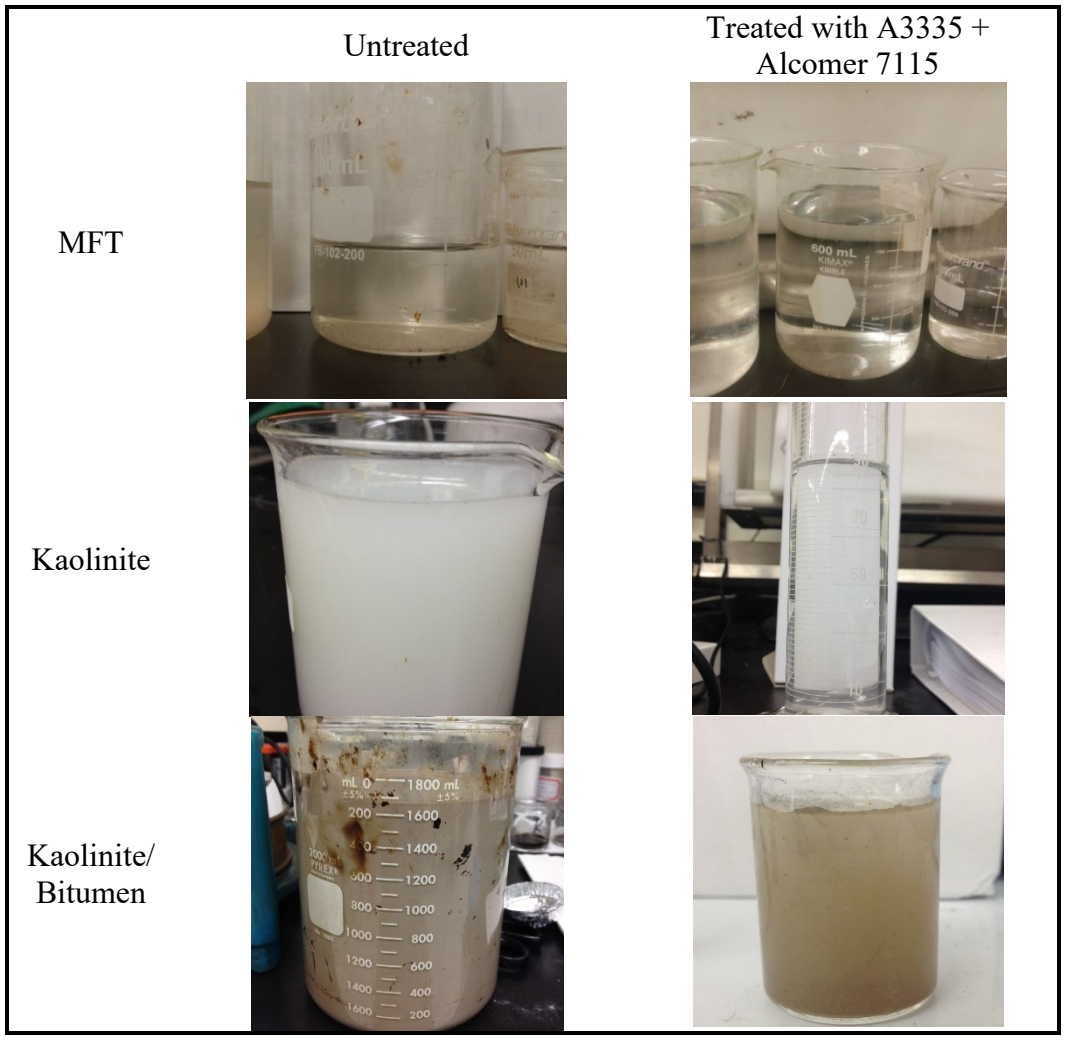

Figure 42. Visual comparison between filtrates of the different treatments.

When untreated kaolinite/bitumen was compared with untreated MFT, it was found that the layer deposited on the filter cloth was much “looser” and had lower solids

content in the kaolinite/bitumen case (kaolinite/bitumen = 51.1 wt.%, MFT = 60.8 wt.%).

4.4 Micro-CT Porosity Analysis

Filter cake porosity obtained from the micro-CT data is reported in Figure 43 and compared against the corresponding solids content results. Porosity values were calculated based on binary thresholds assigned as described in Appendix B. The total porosity was essentially equivalent to the open porosity since the closed porosity values were negligible (<0.008%).

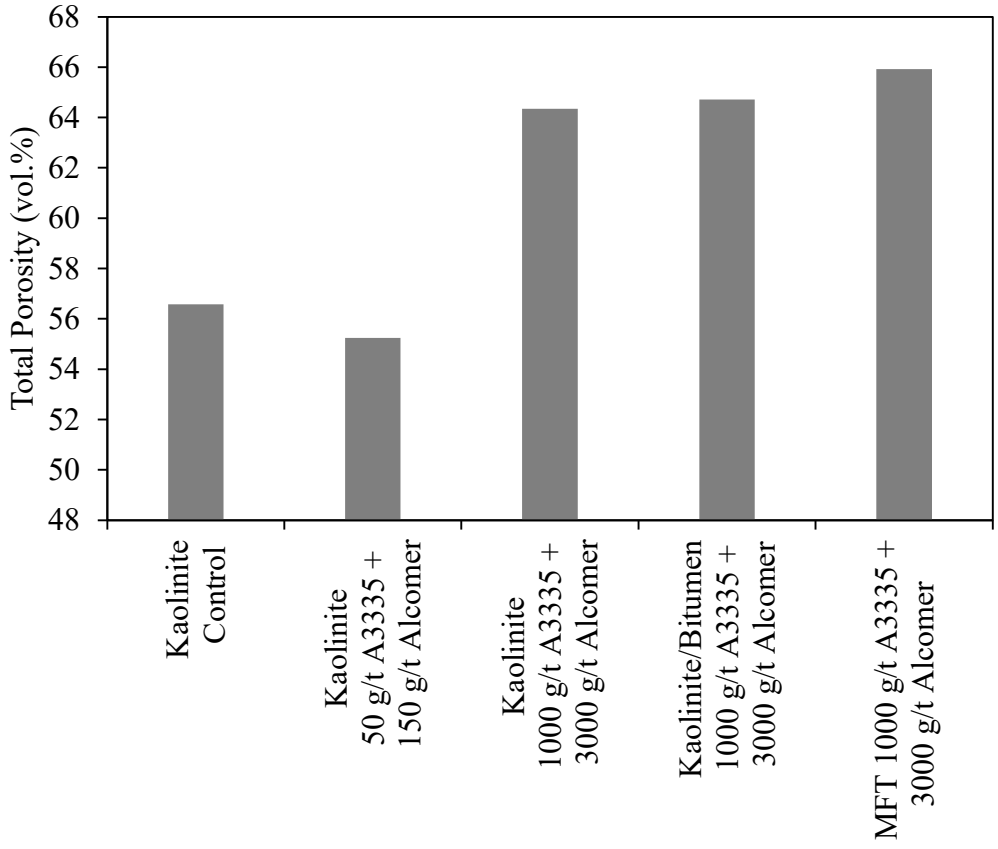

Figure 43. Comparison of filter cake porosities determined from micro-CT imaging.

The porosity values calculated from the micro-CT data corresponded well to the solids content of the filter cakes. Greater porosity correlated to lower solids content, which was observed across all samples. Furthermore, the porosity corresponded well with MFT solids content and water volume fraction data (Fig. 44). For example, the MFT filter cake treated with 1000 g/t A3335 + 3000 g/t Alcomer 7115 had a solids content of 59.8 wt.% (corresponding to 63.6 vol.% water, see Fig. 44 and Appendix D for calculation) and a porosity of 65.9 vol.%.

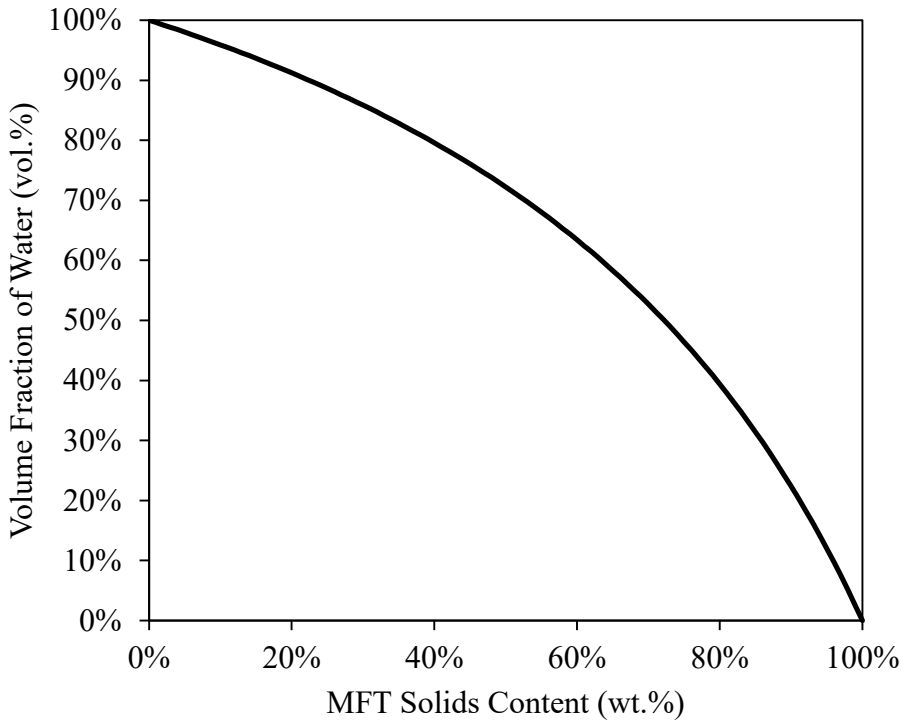

Figure 44. Relationship between MFT solids content and volume fraction of water.

It should be noted however that the pores within the filter cake may not be completely filled with water. The pores may be partially filled with water and include air spaces or residual bitumen. If only a portion of the pores are filled with water, then the porosity values obtained from the micro-CT analysis underestimate the actual solids content. For example, if the MFT filter cake treated with the

A3335 + Alcomer 7115 had a porosity of 65.9 vol.% (yielding a solids content of 57.4 wt.%), but 5 vol.% of the porosity was air rather than water, then the final solids content would be 59.8 wt.%.

The pore connectivity calculated from the micro-CT data is reported in Figure 45. Connectivity is calculated by using an algorithm that clusters connected voxels of porosity using a voxel neighborhood connectivity requirement of 6 (Mendoza *et al*., 2007).

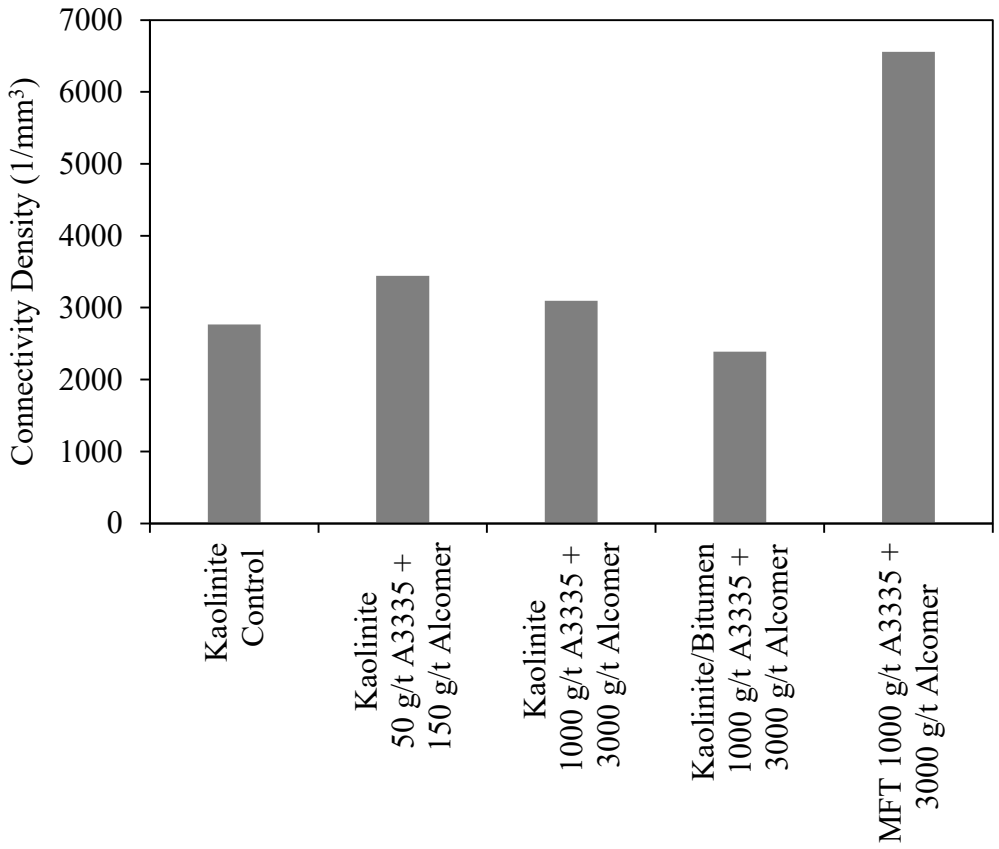

Figure 45. Comparison of filter cake pore connectivity densities determined from micro-CT imaging.

The increase of connectivity density was noticeable with the dual polymer treated MFT. This supports the theory that dual polymer flocculation bridges smaller flocs

to form larger flocs thus creating larger channels for water to be released through. However, there was only a slight increase in connectivity density for the dual polymer treated kaolinite. The overdosed kaolinite likely produced lower connectivity due to excess polymer saturating the system. It is possible that the kaolinite/bitumen slurry treated with A3335 + Alcomer 7115 likely exhibited low connectivity due to poorly dispersed bitumen droplets "plugging" the pores. Since untreated MFT was not able to form a cake with the filter press, no direct comparison can be drawn for the dual polymer flocculation of MFT. The increased connectivity density obtained by micro-CT for the dual polymer treated MFT cake raises the question as to why we do not see more water removed and a higher solids content. There are still factors that need to be investigated such as how the polymer treatment affects bitumen distribution. With the techniques used in this analysis, the residual bitumen was not able to be visualized.

5 CONCLUSIONS AND RECOMMENDATIONS

Two stage flocculation of Alberta oil sands mature fine tailings (MFT) using the anionic-cationic A3335 + Alcomer 7115 pair and the anionic-nonionic A3335 + PEO pair performed better than single polymer treatments in terms of lower CST and higher final solids content of filter press cakes. Preloaded filter plate tests suggested that the flocs produced by the two-stage treatment with A3335 + Alcomer 7115 appeared to be more shear sensitive whereas the A3335 + PEO flocs appeared to be more shear resistant.

The addition of residual bitumen to kaolinite showed that residual bitumen has an adverse effect on the dewatering of kaolinite. Not only did the addition of bitumen lengthen CST, lower filter cake solids content, and decrease filtration efficiency, but it also resulted in high solids content in the filtrate and considerable soiling of the filter cloths with bitumen.

Without the use of a contrast agent, differentiation between water and bitumen phases could not be achieved in micro-CT imaging. However, using the assumption that the pores consisted of air, water, and/or bitumen, the porosity values calculated from the micro-CT scans of the filter cakes corresponded well with the solids content and calculated volume ratio of water. The calculated connectivity density of the pores within the filter cakes of MFT treated by the polymers suggested that the length of the pores increased with dual polymer treatment by A3335 and Alcomer 7115. However, more studies are necessary to

explain why the water was not continuously removable at the high degree of pore connectivity.

Suggestions for further study include the visualization of pore structure before and after filtration, the visualization of residual bitumen during stages of flocculation and filtration, and the investigation of polymer interaction with residual bitumen in order to find more effective polymers to alleviate the detrimental effect of the residual bitumen in the oil sands tailings on dewatering.

References

AER. (2015). ST98: Alberta's Energy Reserves & Supply/Demand Outlook – ST98 2015 Infographic. Alberta Energy Regulator. Retrieved from https://www.aer.ca/documents/sts/ST98/ST98-2015_Infographic.pdf

AER. (2016). ST98: Alberta's Energy Reserves & Supply/Demand Outlook – ST98 2016 Infographic. Alberta Energy Regulator. Retrieved from http://www1.aer.ca/st98/data/executive_summary/ST98-2016_Infographic.pdf

AESRD, & AER. (2015, April 4). OSIP - Data Library [Text]. Retrieved September 21, 2016, from http://osip.alberta.ca/library/Dataset/Details/542

Alagha, L., Wang, S., Yan, L., Xu, Z., & Masliyah, J. (2013). Probing Adsorption of Polyacrylamide-Based Polymers on Anisotropic Basal Planes of Kaolinite Using Quartz Crystal Microbalance. *Langmuir*, *29*(12), 3989–3998. https://doi.org/10.1021/la304966v

Alamgir, A., Harbottle, D., Masliyah, J., & Xu, Z. (2012). Al-PAM Assisted Filtration System for Abatement of Mature Fine Tailings. *Chemical Engineering Science*, *80*, 91–99. https://doi.org/10.1016/j.ces.2012.06.010

Bauer, A. (2013). *Identification of Oil Sands Naphthenic Acid Structures and Their Associated Toxicity to Pimephales promelas and Oryzias latipes* (MSc Thesis). University of Waterloo, Waterloo, ON. Retrieved from https://uwspace.uwaterloo.ca/bitstream/handle/10012/7297/Bauer_Anthony.pdf?sequence=1

Beier, N., & Sego, D. (2008). *The Oil Sands Tailings Research Facility* (pp. 72–77). Geotechnical News. Retrieved from http://www.infomine.com/library/publications/docs/Beier2008.pdf

Bruice, P. Y. (2012). *Organic Chemistry* (7 edition). Boston: Pearson.

CAPP. (2016a). Oil Sands History and Milestones. Retrieved August 16, 2016, from http://www.canadasoilsands.ca/en/what are the oil sands/oil sands history and milestones

CAPP. (2016b). Tailings Ponds. Retrieved August 16, 2016, from http://www.canadasoilsands.ca/en/explore topics/tailings ponds

Clark, K. A. (1939). The Hot Water Method for Recovering Bitumen from Bituminous Sand. Alberta Research Council.

Coulson, J. M., Richardson, J. F., Backhurst, J. R., & Harker, J. H. (1990). *Chemical Engineering: Particle Technology & Separation Processes* (4 edition, Vol. 2). Butterworth-Heinemann.

Demoz, A., & Mikula, R. J. (2012). Role of Mixing Energy in the Flocculation of Mature Fine Tailings. *Journal of Environmental Engineering*, *138*(1), 129–136. https://doi.org/10.1061/(ASCE)EE.1943-7870.0000457

Fan, A., Turro, N. J., & Somasundaran, P. (2000). A Study of Dual Polymer Flocculation. *Colloids and Surfaces A: Physicochemical and Engineering Aspects*, *162*(1–3), 141–148. https://doi.org/10.1016/S0927-7757(99)00252-6

Farinato, R. S., & Dubin, P. L. (Eds.). (1999). *Colloid-Polymer Interactions: From Fundamentals to Practice* (1 edition). New York: Wiley-Interscience.

Glatz, G., Castanier, L. M., & Kovscek, A. R. (2016). Visualization and Quantification of Thermally Induced Porosity Alteration of Immature Source Rock Using X-ray Computed Tomography. *Energy & Fuels*. https://doi.org/10.1021/acs.energyfuels.6b01430

Haroon, M. H. (2014). *Flocculation and Dewatering of Kaolinite Suspensions and Oil Sands Mature Fine Tailings Using Dual Polymers* (MSc Thesis). University of Alberta, Edmonton, AB, Canada.

Hunter, R. J. (2000). *Foundations of Colloid Science* (Second Edition edition). Oxford ; New York: Oxford University Press.

Kaminsky, H. (2006). Fundamental Particle Size of Clay Minerals in Athabasca Oil Sands Tailings. *Clay Science*, *12*, 217–222.

Kaminsky, H. (2014). Demystifying the Methylene Blue Index. Presented at the 4th International Oil Sands Tailings Conference, Banff, AB, Canada.

Kelly, E. N., Schindler, D. W., Hodson, P. V., Short, J. W., Radmanovich, R., & Nielsen, C. C. (2009). Oil Sands Development Contributes Elements Toxic at Low Concentrations to the Athabasca River and Its Tributaries. *Proceedings of the National Academy of Sciences of the United States of America*, *106*. Retrieved from http://www.pnas.org/content/107/37/16178.full.pdf

Khanamiri, H. H., Torsæter, O., & Stensen, J. Å. (2016). Effect of Calcium in Pore Scale Oil Trapping by Low Salinity Water and Surfactant EOR at Strongly Water Wet conditions: In Situ Imaging by X-Ray Microtomography. *Energy & Fuels*. https://doi.org/10.1021/acs.energyfuels.6b01236

Klein, C. G. (2014). *Effect of Residual Bitumen on Polymer-assisted Flocculation of Fluid Fine Tailings* (MSc Thesis). University of Alberta, Edmonton, AB, Canada.

Konan, K. L., Peyratout, C., Bonnet, J.-P., Smith, A., Jacquet, A., Magnoux, P., & Ayrault, P. (2007). Surface Properties of Kaolin and Illite Suspensions in Concentrated Calcium Hydroxide Medium. *Journal of Colloid and Interface Science*, *307*(1), 101–108. https://doi.org/10.1016/j.jcis.2006.10.085

Liu, J. K., Lane, S. J., & Cymbalisty, L. M. (1980, September 30). Filtration of Hot Water Extraction Process Whole Tailings. Retrieved from http://www.google.com/patents/US4225433

Long, J., Xu, Z., & Masliyah, J. H. (2006). Adhesion of Single Polyelectrolyte Molecules on Silica, Mica, and Bitumen Surfaces. *Langmuir*, *22*(4), 1652–1659. https://doi.org/10.1021/la052757f

Masliyah, J. H., Czarnecki, J., & Xu, Z. (2011). *Handbook on Theory and Practice of Bitumen Recovery from Athabasca Oil Sands* (1st edition). Kingsley Knowledge Publishing.

Masliyah, J., Zhou, Z. J., Xu, Z., Czarnecki, J., & Hamza, H. (2004). Understanding Water-Based Bitumen Extraction from Athabasca Oil

Sands. *The Canadian Journal of Chemical Engineering*, *82*(4), 628–654. https://doi.org/10.1002/cjce.5450820403

McFarlane, A. J., Addai-Mensah, J., & Bremmell, K. (2005). Rheology of Flocculated Kaolinite Dispersions, *17*(4), 181.

Mendoza, F., Verboven, P., Mebatsion, H. K., Kerckhofs, G., Wevers, M., & Nicolaï, B. (2007). Three-Dimensional Pore Space Quantification of Apple Tissue using X-ray Computed Microtomography. *Planta*, *226*(3), 559–570. https://doi.org/10.1007/s00425-007-0504-4

Mikula, R. J., Lam, W. W., & Payette, C. (1993). Proceedings of Oil Sands – Our Petroleum Future. In *Our Petroleum Future*. Edmonton, AB, Canada.

Mitchell, J. K. (1976). *Fundamentals of soil behavior*. Wiley.

Mpofu, P., Addai-Mensah, J., & Ralston, J. (2003). Investigation of the Effect of Polymer Structure Type on Flocculation, Rheology and Dewatering Behavior of Kaolinite Dispersions. *International Journal of Mineral Processing*, *71*(1–4), 247–268. https://doi.org/10.1016/S0301-7516(03)00062-0

Neelakantan, R. (2016). *Effect of Shear Energy Input on the Rheology of Flocculant-Dosed Kaolinite Suspensions* (MSc Thesis). University of Alberta, Edmonton, AB, Canada.

Nix, P. G., & Martin, R. W. (1992). Detoxification and Reclamation of Suncor's Oil Sand Tailings Ponds. *Environmental Toxicology and Water Quality*, *7*(2), 171–188. https://doi.org/10.1002/tox.2530070208

Osacky, M., Geramian, M., Ivey, D. G., Liu, Q., & Etsell, T. H. (2015). Influence of Nonswelling Clay Minerals (Illite, Kaolinite, and Chlorite) on Nonaqueous Solvent Extraction of Bitumen. *Energy & Fuels*, *29*(7), 4150–4159. https://doi.org/10.1021/acs.energyfuels.5b00269

Osacky, M., Geramian, M., Liu, Q., Ivey, D. G., & Etsell, T. H. (2014). Surface Properties of Petrologic End-Members from Alberta Oil Sands and Their Relationship with Mineralogical and Chemical Composition. *Energy & Fuels*, *28*(2), 934–944. https://doi.org/10.1021/ef402150z

Ovenden, C., & Xiao, H. (2002). Flocculation Behavior and Mechanisms of Cationic Inorganic Microparticle/Polymer Systems. *Colloids and Surfaces A: Physicochemical and Engineering Aspects*, *197*(1), 225–234. https://doi.org/10.1016/S0927-7757(01)00903-7

Pembina Institute. (2010). Federal Parliamentary Committee Hearing on Water and the Oil Sands. Written Submission. Retrieved from https://www.pembina.org/reports/oil-sands-and-water-submission.pdf

Rajagopalan, R. (2016). Silicates. Retrieved September 21, 2016, from http://ramaseshan.com/MMT.php

Ripperger, S., Gösele, W., & Alt, C. (2000). Filtration, 1. Fundamentals. In *Ullmann's Encyclopedia of Industrial Chemistry*. Wiley-VCH Verlag GmbH & Co. KGaA. Retrieved from http://onlinelibrary.wiley.com/doi/10.1002/14356007.b02_10.pub2/abstract

Scott, J., Dusseault, M. B., & David Carrier, W. (1985). Behavior of the Clay/Bitumen/Water Sludge System from Oil Sands Extraction Plants.

Applied Clay Science, *1*(1), 207–218. https://doi.org/10.1016/0169-1317(85)90574-5

Sijbers, J., & Postnov, A. (2004). Reduction of Ring Artifacts in High Resolution Micro-CT Reconstructions. *Physics in Medicine and Biology*, *49*(14), 247–255.

Sobkowicz, J. (2012). *Oil Sands Tailings Technology Deployment Roadmaps Project Report – Volume 1 Project Summary* (No. 17-235–22) (p. 243). Alberta Innovates - Energy and Environment Solutions.

Steward, G. (2015, September 4). Tailings Ponds a Toxic Legacy of Alberta's Oilsands | Toronto Star. Retrieved September 21, 2016, from https://www.thestar.com/news/atkinsonseries/2015/09/04/tailings-ponds-a-toxic-legacy-of-albertas-oilsands.html

Suthaker, N. N., & Scott, J. D. (1996). Measurement of Hydraulic Conductivity in Oil Sand Tailings Slurries. *Canadian Geotechnical Journal*, *33*(4), 642–653. https://doi.org/10.1139/t96-089-310

Sworska, A., Laskowski, J. S., & Cymerman, G. (2000). Flocculation of the Syncrude Fine Tailings: Part I. Effect of pH, Polymer Dosage and Mg2+ and Ca2+ Cations. *International Journal of Mineral Processing*, *60*(2), 143–152. https://doi.org/10.1016/S0301-7516(00)00012-0

Tarleton, E. S., & Wakeman, R. J. (2007). *Solid/Liquid Separation Equipment Selection and Process Design /* (1st ed.). Oxford : Butterworth-Heinemann,.

Van Olphen, H. (1977). *An Introduction to Clay Colloid Chemistry* (2nd Edition edition). New York: John Wiley & Sons.

Vedoy, D. R. L., & Soares, J. B. P. (2015). Water-Soluble Polymers for Oil Sands Tailing Treatment: A Review. *The Canadian Journal of Chemical Engineering*, *93*(5), 888–904. https://doi.org/10.1002/cjce.22129

Wang, X. (Tara), Feng, X., Xu, Z., & Masliyah, J. H. (2010). Polymer Aids for Settling and Filtration of Oil Sands Tailings. *The Canadian Journal of Chemical Engineering*, *88*(3), 403–410. https://doi.org/10.1002/cjce.20283

Xu, Y., & Cymerman, G. (1999). Flocculation of Fine Oil Sand Tails. Polymers in Mineral Processing. In *Proceedings of the UBC-McGill Bi-Annual International Symposium on Fundamentals of Mineral Processing* (Vol. 3, pp. 591–604). Quebec City, QC, Canada.

Xu, Y., Dabros, T., & Kan, J. (2008). Filterability of Oil Sands Tailings. *Process Safety and Environmental Protection*, *86*(4), 268–276. https://doi.org/10.1016/j.psep.2008.04.005

Yuan, S., & Siman, R. (2012). *Procedures for Validation of Flocculants for High Density FFT with a 125-mm Dynamic Mixing Tank* (Internal Report of the Tailings Environmental Priority Area of Canada's Oil Sands Innovation Alliance No. Rev 4). Research and Development Syncrude Canada Ltd.

Zhu, Y. (2015). *Cationic and Anionic Dual Polymer Pairs for Mature Fine Tailings Flocculation and Dewatering* (MSc Thesis). University of Alberta, Edmonton, AB, Canada.

APPENDIX A – PREPARATION OF KAOLINITE/BITUMEN SLURRY

Part 1: Composition of Centrifuged MFT Layers

MFT centrifuged at 9900 rpm for three hours formed three distinct layers; supernatant, middle layer, and bottom layer.

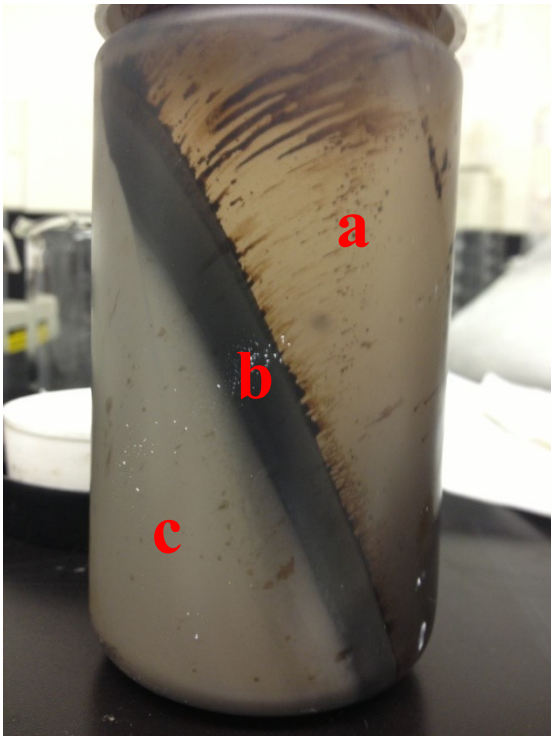

Figure 46: Centrifuged MFT (a) supernatant, (b) middle layer, (c) bottom layer.

For the purpose of extracting the middle layer and the supernatant, MFT from CNRL was used.

- The MFT was treated with the Dean Stark extraction to determine the solids, water, and bitumen content.
    - Moisture content mass balance from oven drying was used to confirm solids content
- Centrifuge CNRL MFT to create supernatant, middle layer (ML), and bottom layer (BL)
    - CNRL MFT was centrifuged in batches of six, 250 mL centrifuge bottles at 9900 rpm (17,344 RCF) for 3 hours in a Beckman Coulter Avanti J-30I Centrifuge.
- Determine compositions of supernatant, ML, and BL
    - Bitumen content of supernatant was determined by dichloromethane (DCM) extraction with a separatory funnel, solids was assumed to be negligible
    - Solids, water, and bitumen content of BL was determined by Dean Stark
    - Solids, water, and bitumen content of ML was determined by back calculation

Table 2. MFT, supernatant, ML, and BL composition results

	Method	% of Whole MFT	Water	Solids	Bitumen
Whole CNRL MFT	Dean Stark	N/A	67.6%	28.8%	3.6%
Supernatant	DCM extraction	50.5%	99.94%	Assume N/A	0.06%
Bottom Layer	Dean Stark	29.5%	30.8%	69.2%	0%
Middle Layer	Back Calculation	20%	40.2%	41.9%	17.9%

Part 2: Middle Layer and Supernatant Needed to Make a 3 wt. % Bitumen and Kaolinite Slurry

Calculation 1: Calculation of middle layer and supernatant needed for a 63 wt% water kaolinite slurry with 3.4 wt% bitumen content

Amount of bitumen needed for 500 g of kaolinite slurry

$$bit = 0.034 \times 500\,\text{g}$$
$$= 17\,\text{g}$$

Amount of ML needed for 17 g of bitumen

$$ML = \frac{17\,\text{g}}{0.18}$$
$$= 94\,\text{g}$$

Amount of water in 94 g of ML

$$water_{ML} = 94\,\text{g} \times 0.4$$
$$= 37.6\,\text{g}$$

Amount of supernatant needed for a 37 wt% solids slurry

$$water_{total} = 500\,\text{g} \times 0.63$$
$$= 315\,\text{g}$$
$$\text{supernatant} = 315\,\text{g} - 37.6\,\text{g}$$
$$= 277.4\,\text{g}$$

APPENDIX B – BINARY THRESHOLD ASSIGNMENT OF MICRO CT IMAGES

Part 1: Threshold Determination of MicroCT Scans (example taken from scan of filter cake of MFT treated with 1000 g/t A3335 + 3000 g/t Alcomer 7115)

- The differentiation between bitumen and water phase was not possible without the use of a contrast fluid.
- Threshold was determined between solid and non-solid (pore space filled by either air, water, or bitumen) phase.
- Three step verification:
    - Visual identification of pore
    - Grey scale histogram patterning
    - Calculated difference between pore and solid pixel grey scale values (justification is that if the difference between two neighboring pixel grey scale values is large, then it is the interface between solid and pore)

Step 1: Visual identification

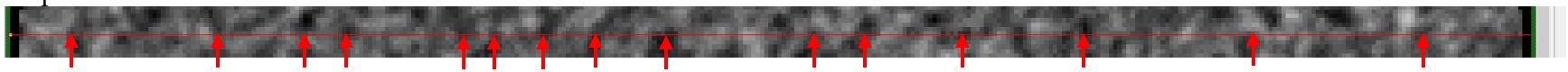

Step 2: Compare with grey scale histogram

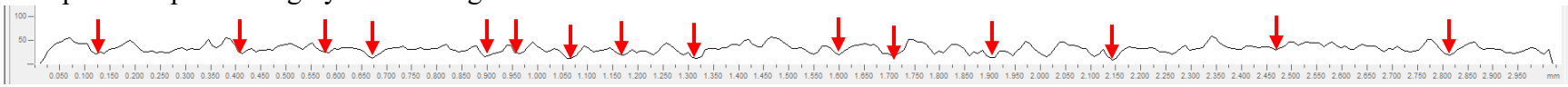

Step 3. Calculate difference in pixel grey scale values

Table 3. Calculated differences between neighboring pixels of assigned pores and solids.

	Grey Scale Units*	Ratio: $\frac{\text{Difference between neighboring pixels}}{\text{Whole Grey Scale Range}}$
Average difference between pore and solid pixel grey scale values	27.6	0.108
Average difference between pixel grey scale values within pores	14.2	0.056
Average difference between pixel grey scale values within solids	13.7	0.054

*Normalized to 255 grey scale spectrum

- The average difference in grey scale value between two neighboring pixels of pore-solid interface is twice as large as the difference between two neighboring pixels within a pore (pore-pore) or within a solid (solid-solid)

APPENDIX C – SAMPLE CALCULATIONS FOR FILTRATION EXPERIMENTS

NWR (ASP 600 kaolinite with 50 g/t A3335 + 150 g/t Alcomer 7115)

1. Calculate the amount of polymer needed (50 g/t A3335, 150 g/t Alcomer)

Solids content of the slurry = 37 wt.%

Solids in 500 g sample = $(0.37)(500\,\text{g})$

= 185 g

Mass of A3335 needed = $\dfrac{(50\,\text{g})(185\,\text{g})}{1000000\,\text{g}}$

= 9.25 mg

Amount of 0.4 wt.% A3335 stock = $\dfrac{(1\,\text{g})(0.00925\,\text{g})}{0.004\,\text{g}}$

= 2.3 g ~ 2.3 mL

Mass of Alcomer 7115 needed = $\dfrac{(150\,\text{g})(185\,\text{g})}{1000000\,\text{g}}$

= 27.75 mg

Amount of 2 wt.% Alcomer stock = $\dfrac{(1\,\text{g})(0.02775\,\text{g})}{0.02\,\text{g}}$

= 1.4 g ~ 1.4 mL

Since the MFT used 20 times this amount, we diluted the 2.3 mL of A3335 stock solution to equal 45 mL and the 1.4 mL of Alcomer 7115 stock solution to equal 27 mL.

2. Amount of slurry consumed for the filter cake

- Calculate amount of slurry needed for the cake:

Original slurry solids content = 37 wt.%

Filter cake solids content = 68.2 wt.%

Volume of filter plates = 280 cm^3

Density of pure kaolinite = 2.6 g/cm^3

Cake density at 68.2 wt.% = $\dfrac{100}{68.2 \Big/ \left(2.6\ g/cm^3\right) + \left(100 - 68.2\right)}$

= 1.72 g/cm^3

Mass of cake = $\left(280\,cm^3\right)\left(1.72\,g/cm^3\right)$

= 482.5 g

Mass of solids = $(482.5\,g)(0.682)$

= 329.1 g

Mass of slurry needed = $\dfrac{329.1\,g}{0.37}$

= 889.4 g

- Calculate volume of hose and pump under pressure:

Hose diameter = 1.59 cm

Hose length = 47 cm

Hose volume = $\pi r^2 h$

= $\pi\left(\dfrac{1.59\,cm}{2}\right)^2 (47\,cm)$

= 93.3 cm^3

Volume of the pump = 262 cm^3

- Total slurry = $\left[93.3\,cm^3 + 262\,cm^3\right]\left(1.25\,g/cm^3\right) + 889.4\,g$

= 1333.5 g

3. Volume of polymer (diluted)

Volume of polymer needed for 1266 g slurry $= \dfrac{(72\,\text{mL})(1333.5\,\text{g})}{500\,\text{g}}$

$= 192.0$ mL

4. NWR

Water released $= 684$ g

NWR $= \dfrac{V_f - V_p}{V_s}$

$= \dfrac{684\,\text{g} - 192.0\,\text{g}}{(1333.5\text{g})(0.63)}$

$= 0.586$

SRF (Sample calculation for kaolinite treated with 50 g/t A3335 + 150 g/t Alcomer 7115)

1. Calculation of concentration c_m

- Amount of solids in the cake at 10 minutes:

Final solids content = 68.2 wt.%

Initial solids content = $\frac{185\,\text{g}}{(500\,\text{g})+(72\,\text{g polymer})}$

= 32.3 wt.%

Slurry density at 32.3 wt.% solids = $\frac{100}{32.3/(2.6\,\text{g/cm}^3)+(100-32.3)}$

= 1.25 g/cm^3

Filtrate collected at 10 minutes = 373 mL

Total filtrate from filtration = 684 mL

% filtrate collected at 10 minute = $\frac{373\,\text{mL}}{684\,\text{mL}}$

= 54.5 %

Water in the cake at the end = (cake mass) – (solids)

= $(482.5\,\text{g})-(329.1\,\text{g})$

= 153.4 g

Water in the cake at the start = $(280\,\text{cm}^3)(1.25\,\text{g/cm}^3)(1-0.323)$

= 236.5 g

If 55% of the water is removed then = $(236.5\,\text{g}-153.4\,\text{g})(0.545)$

= 45 g water removed at 10 min

Solids in cake at 10 min = $(280\,\text{cm}^3-(236.5\,\text{mL}-45\,\text{mL}))(2.6\,\text{g/cm}^3)$

= 230.9 g

c_m = $\frac{230.9\,\text{g}}{373\,\text{mL}}\times 1000$

= 618.9 kg/m^3

2. SRF

SRF = $\frac{2\Delta P A^2}{\mu_f c_m} b$

ΔP = 620 530 Pa - 101 300 Pa = 519 230 Pa

μ_f = 0.0008937 Pa s

A = 0.022 m^2

b (from t/V vs V plot) = 3.32×10^9 s/m^6

SRF = $\frac{2(519230 Pa)(0.022 m)^2}{(0.0008937 Pa\,s)(618.9 kg/m^3)}(3.32 \times 10^9\ s/m^6)$

= 3.01×10^{12} m/kg

APPENDIX D – CALCULATION OF WATER VOLUME FRACTION FROM SOLIDS CONTENT IN MFT

Density of solids = $2.6\ t/m^3$

Density of water = $1\ t/m^3$

Density of MFT (36 wt.% solids) = $$\frac{100}{36 \Big/ \left(2.6\ g/cm^3\right) + \left(100 - 36\right)}$$

= $1.28\ t/m^3$

Density of cake (59.8 wt.% solids) = $$\frac{100}{59.8 \Big/ \left(2.6\ g/cm^3\right) + \left(100 - 59.8\right)}$$

= $1.58 t/m^3$

Volume fraction of water = $$\frac{100 - 59.8}{59.8 \Big/ \left(2.6\ g/cm^3\right) + \left(100 - 59.8\right)}$$

= 63.6 %

APPENDIX E – THE MULTIPHASE SIMULATION OF DENSE SLURRY AND FLOCCULANT DISTRIBUTION IN A STIRRED VESSEL

Introduction

Based on early numerical applications to three-dimensional solids dispersion (Issa & Gosman, 1981; Looney *et al*., 1985; Politis, 1989; Rizk & Elghobashi, 1989; Kresta & Wood, 1991), flow models and numerical methods for multiphase systems of solids and liquids have been proposed (Gosman *et al*., 1992; Bakker *et al*., 1994; Myers *et al.*, 1994). Euler-Euler approaches using the k-ε turbulence model were preferred due to simplicity, lower computational requirements, faster numerical resolution, and their capability to deal with high solids loading. Flow patterns of suspended solids in an agitated tank were assessed and it was determined that mixed flow impellers such as the pitched blade turbine were more efficient for solids dispersion than radial flow impellers (Bakker *et al.*, 1994; Montante *et al.*, 2001). This claim was further supported with both floating solids and light solids (Kuzmanić & Ljubičić, 2001; Özcan-Taskin & McGrath, 2001).

The application of the more advanced Multi Fluid Model (MFM) yields superior results to the simpler Settling Velocity Model (SVM), however at the expense of random access memory (RAM) and central processing unit (CPU) times (Micale *et al*., 2000). The same can be said of the comparison between the Sliding Grid (SG) and Inner-Outer (IO) approach. SG is more computationally demanding than IO but yields better comparison to experimental results in both multiphase and single phase simulations (Luo *et al*., 1993; Brucato *et al.*, 1998; Montante &

Magelli, 2007). At high solids loading, the comparison of SG and Multiple Reference Frame (MRF) techniques shows no significant difference (Tamburini *et al*., 2013).

Numerical modeling of dense solid-liquid systems requires additional considerations of solid-liquid and solid-solid interactions. Even in dilute systems, the inclusion of interphase momentum exchange terms such as the Basset force, virtual mass force, lift force and drag force are important in correctly describing the interaction between phases (Ljungqvist & Rasmuson, 2001). The drag force influences solids suspension and dispersion (Ochieng & Onyango, 2008), and the drag force is affected by turbulence and concentration (Gidaspow, 1994; Brucato *et al.*, 1998; Montante & Magelli, 2007; Montante & Magelli, 2005; Khopkar *et al.*, 2006; Ochieng & Onyango, 2008). Various drag models have been applied to multiphase simulations and include the Schiller Naumann model (AEA Technology, 2003), the Brucato model (Brucato *et al*., 1998), the Syamlal and O'Brien model (Syamlal & O'Brien, 1989), and the Gidaspow model (Gidaspow, 1994). The Schiller Naumann drag force considers inertial effects on the drag force, however is most reliable at low impeller speeds (Micale *et al.*, 2004). For high particle concentrations ($\alpha_p > 10^{-3}$), four way coupling must be accounted for (Elghobashi, 1994). Particle-particle interactions have been examined and corrections such as the excess solid volume correction (ESVC) algorithm (Tamburini *et al.*, 2013; Tamburini *et al.*, 2009), the Gidaspow model which accounts for particle-particle interaction through the solid pressure (Ochieng &

Onyango, 2008; Gidaspow, 1994), and the corrections for collision intensities and frequencies (Derksen, 2003), have been compared.

Turbulent flow of particles as small as 10 μm (Altway *et al.*, 2001) and mass fractions as high as 0.338 have been modeled (Tamburini *et al*., 2013) with good agreement to experimental results. With high solids loading, the asymmetric *k-ε* turbulence model is more applicable than the homogeneous *k-ε* turbulence model (Tamburini *et al.*, 2013), although it has been recorded that the homogenous *k-ε* turbulence model provides satisfactory results for particle distribution in dense stirred suspensions (Montante & Magelli, 2005; Khopkar *et al.*, 2006; Micale *et al*., 2004; Tamburini *et al.*, 2009; Montante *et al*., 2001; Kasat *et al.*, 2008). Both Large Eddy Simulation (LES) and Reynolds Averaged Navier-Stokes (RANS) have been used to model high concentration slurries, with RANS yielding better results giving good predictions of trailing vortices length and intensity, solids velocities, and turbulent kinetic energy (Guha *et al.*, 2008).

Model Description

- Euler-Euler approach
- K-epsilon model renormalization group (RNG) swirl dominated flow
- Fluid (water) and dispersed phase (solid particles) treated mathematically as inter-penetrating continua using conservative equations averaged over *representative elementary volume* (REV) for each phase
- Volume fraction of overlapping phases are assumed to be continuous fractions of space and time

- Laws of conservation of mass and momentum are satisfied by each phase
- Model equations adapted from ANSYS FLUENT user guide

Model Parameters

Table 4. Model parameters used for the multiphase simulation of dense slurry.

Parameter	*Model/Scheme Name*
Multiphase flow	Euler-Euler
Volume fraction parameters	Implicit Scheme
Viscous model	Unsteady Laminar
Drag model	Syamlal-O'Brien
Granular temperature	Phase property
Granular viscosity	Syamlal-O'Brien
Granular bulk viscosity	Lun-et-al
Frictional Viscosity	Johnson-et-al
Frictional Pressure (pascal)	Johnson-et-al
Solid Pressure	Syamlal-O'Brien
Radial Distribution	Syamlal-O'Brien
Pressure-Velocity Coupling	Coupled Scheme
Spatial Discretization-Gradient	Least Squares Cell Based
Spatial Discretization-Momentum	QUICK
Spatial Discretization-Volume Fraction	Modi_ed HRIC
Transient Formulation	First Order Implicit

Numerical Parameters

- Vessel dimensions (see Figure 47) were chosen based on an experimental procedure established by Syncrude Canada Ltd for mature fine tailings (MFT) slurry treatment (Yuan and Siman, 2012)
- 45° PBT impeller chosen based on experimental support for efficient solids suspension by mixed flow radial impellers
- Solids chosen based on MFT solids concentration (36 wt.% solids)
- Particle size of solids 15 μm
- Impeller speeds of 300 and 600 rpm were simulated, however only the results of the 300 rpm simulations are reported here
- Use coupled algorithm to solve momentum and pressure based continuity equations together
- QUICK scheme for the discretization of convective terms in momentum conservation equations
- Modified High Resolution Interface Capturing (HRIC) scheme for the discretization of convective terms in calculation of solid volume fraction
- Computational grid comprised of 524 288 cells shown in Figure 47.

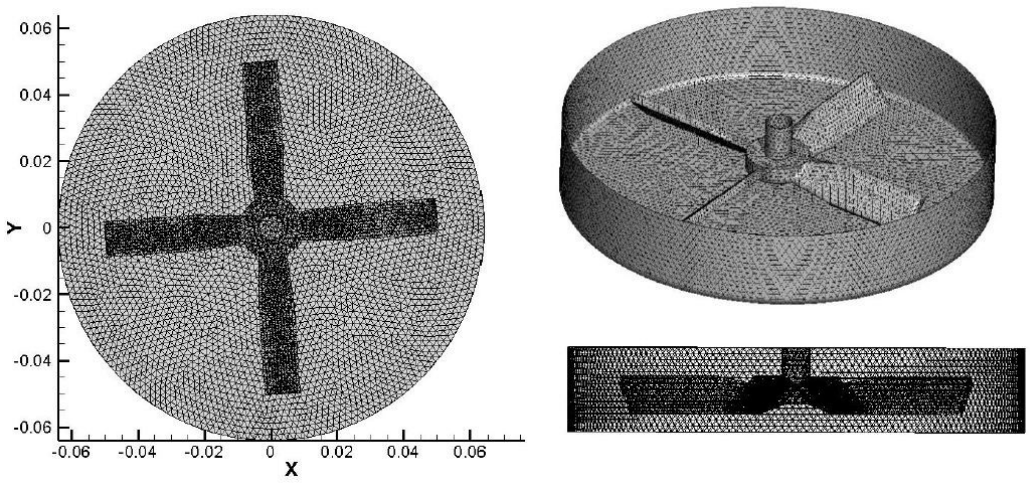

Figure 47 The computational grid that was adopted to run all simulations. It consists of 524 288 cells.

Table 5. Vessel dimensions.

Parameter	*Measurement*
Vessel Diameter	128 mm
Impeller Diameter	100 mm
Shaft Diameter	8 mm
Vessel Depth	28 mm
Impeller Height	15 mm
Impeller Clearance	5 mm
Impeller Submergence	8 mm

Results and Discussion

Two simulations were compared to evaluate the quantities of turbulent kinetic energy (*TKE,* J/kg), turbulent dissipation rate (ε, J/kg s), and turbulent length scale ($L_{ED,}$ m). The first case consisted of pure water and served as a control and a benchmark comparison for the slurry cases. The second case consisted of a two

phase slurry system where water was the fluid phase and the solids (15 μm diameter silicon particles) were the dispersed phase. These two cases were also used to assess the steady state conditions based on the integral characteristics azimuthal velocity (U_θ) and turbulent viscosity (μ_t) in the non-dimensional form. A third simulation was carried out to solve for scalar mixing of a viscous tertiary phase (flocculant solution) into the slurry that was set up in case 2.

Figures 48 and 49 show the time histories of U_θ and μ_t in the non-dimensional form, where the scaling parameters are radial velocity (ΩR) and laminar viscosity (μ), respectively.

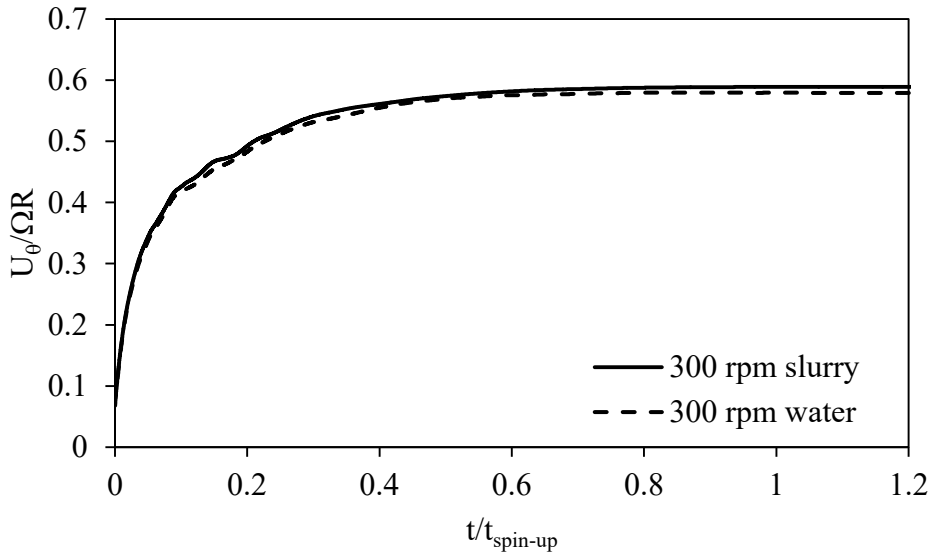

Figure 48. Time history of the integral characteristic $U_\theta/\Omega R$ with respect to $t/t_{spin\text{-}up}$ at 300 rpm of pure water and slurry.

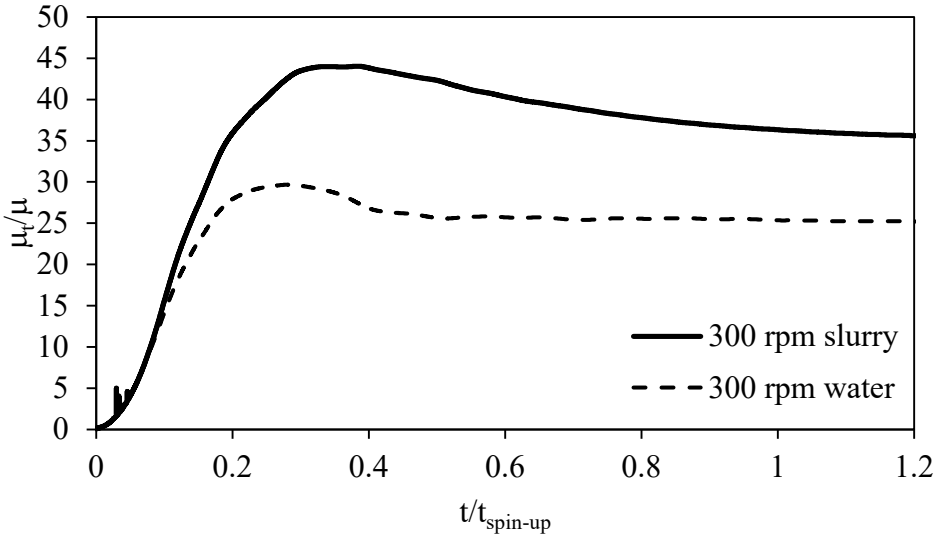

Figure 49. Time history of the integral characteristic μ_t/μ with respect to $t/t_{spin-up}$ at 300 rpm of pure water and slurry.

The ratio μ_t/μ is also known as the turbulent viscosity ratio. The non-dimensional parameters $U_\theta/\Omega R$ and μ_t/μ are reported with respect to non-dimensional time ($t/t_{spin-up}$) where $t_{spin-up}$ is the spin-up time.

The calculation of spin-up time was taken from Maynes and Butcher who gathered data from 33 different impellers in three different cylindrical tanks on the number of revolutions it took to achieve steady state. The $t_{spin-up}$ is thus the time it takes for the system to reach steady state and can be described by the following relationships (Maynes & Butcher, 2002):

$$t^* = \frac{\omega t}{2\pi} \tag{11}$$

$$L^* = \frac{L}{R} \tag{12}$$

$$t^*_{spin-up} = 3.94\left[L^{*3}\frac{h}{H}\right]^{-0.7} \tag{13}$$

$$t_{spin-up} = \frac{2\pi}{\omega} t^*_{spin-up} \tag{14}$$

t^* = non-dimensional time (revolutions)

ω = angular rotation rate, 1/s

t = time, s

L^* = non-dimensional body length

L = characteristic body length (impeller radius), m

R = tank radius, m

$t^*_{spin\text{-}up}$ = revolutions when steady state is attained

h = body height, m

H = fluid height in tank, m

$t_{spin\text{-}up}$ = time to reach steady state, s

As expected for steady state, the non-dimensional parameters $U_\theta/\Omega R$ and μ_t/μ reached a constant value when the elapsed time (t) equaled the $t_{spin\text{-}up}$ (i.e. $t/t_{spin\text{-}up}$ = 1). It was also expected that the μ_t/μ would be higher for the slurry since the viscosity of the slurry (1 Pa·s) was much larger than that of water (0.8937 mPa·s) (Yang, 2009).

The quantities of *TKE,* ε, and L_{ED} are shown in Figures 50, 51, and 52 respectively. The *TKE,* ε, and L_{ED}, are reported in terms of non-dimensional time calculated from spin-up time ($t_{spin\text{-}up}$).

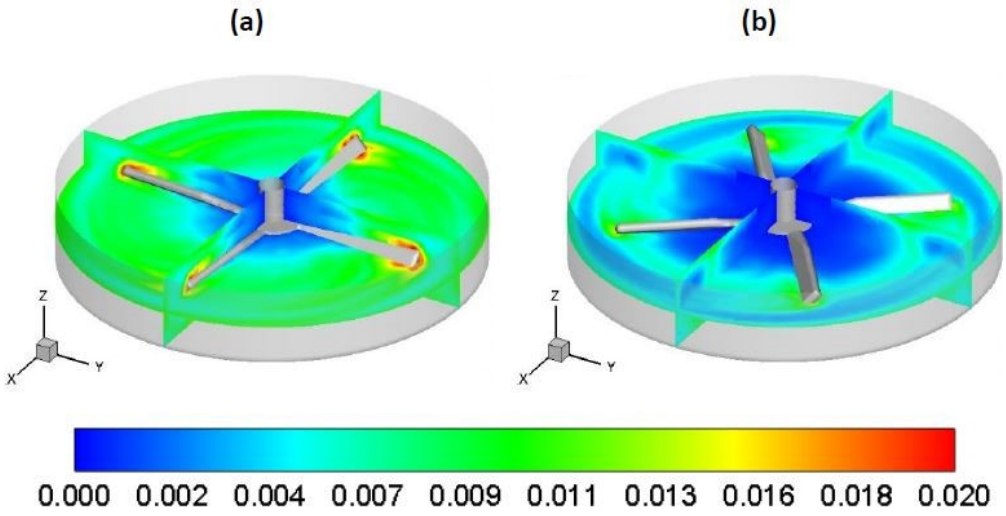

Figure 50. Steady state turbulent kinetic energy, *TKE* (J/kg) for (a) water 300 rpm (b) slurry 300 rpm.

Pure water was found to have a higher *TKE* than the slurry. The *TKE* represents the turbulence in the system, and the turbulence in a stirred tank is a result of fluctuating velocity components that form eddies. In the presence of solids, the turbulence is dampened, thus lowering the *TKE*. *TKE* reached a maximum at the impeller tips due to the trailing vortices that form, resulting in larger velocity fluctuations.

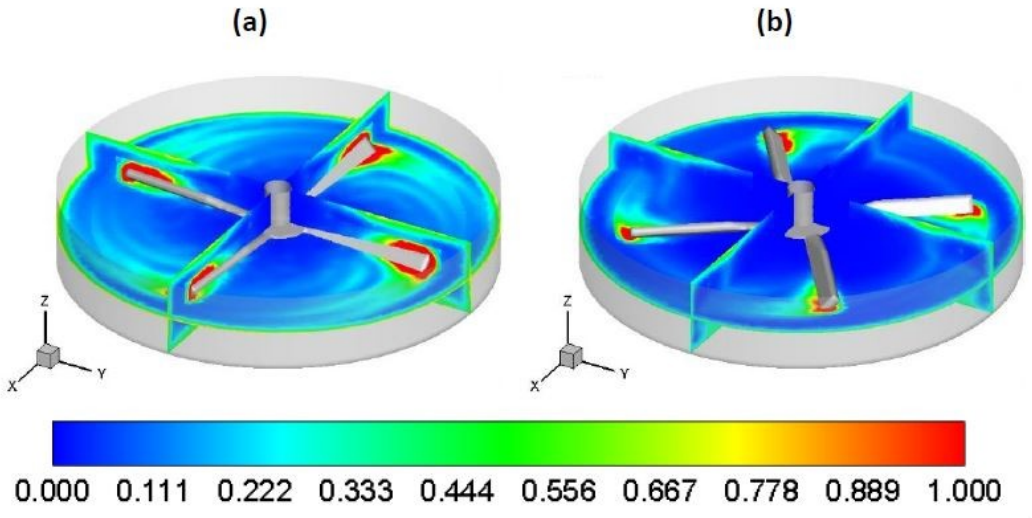

Figure 51. Steady state turbulent dissipation rate, ε (J/kg s) for (a) water 300 rpm (b) slurry 300 rpm.

As with *TKE*, it is observed that the ε, also diminished with the addition of solids. This can be explained with the same logic that applies to the decrease of *TKE* upon the presence of solids. These results were consistent with the findings of Micheletti & Yianneskis (2004) and Unadkat *et al.* (2009).

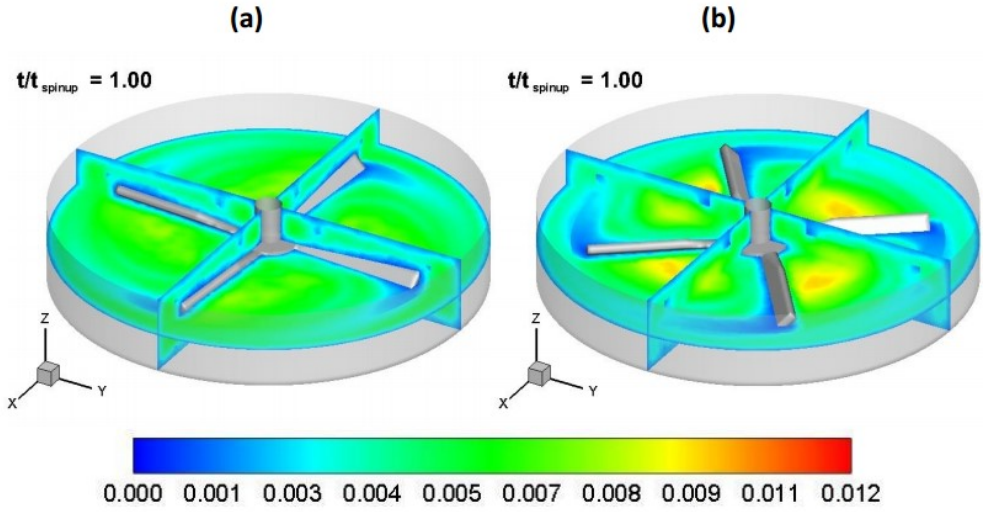

Figure 52. Steady state turbulent length scale, L_{ED} (m) for (a) water 300 rpm (b) slurry 300 rpm.

The L_{ED} represents the size of the eddies that contribute to the velocity fluctuations in turbulent environments. It stands to reason, based on the relationship that L_{ED} is derived from (Equation 15), that the L_{ED} would be larger in the presence of solids. Since 80% of the turbulent kinetic energy is found at the integral length scale (also referred to as the energy containing range), the L_{ED} is given by (Tennekes & Lumley, 1972):

$$L_{ED} = \frac{TKE^{\frac{3}{2}}}{\varepsilon} \tag{15}$$

L_{ED} = *t*urbulent length scale (eddy length scale), m

TKE = turbulent kinetic energy, J/kg

ε = turbulent dissipation rate, J/kg s

The mass fraction results of the scalar mixing are reported in Figure 53. The scalar mixing case simulated the scalar dissipation of a shear thinning viscous tertiary phase into the two-phase dense slurry.

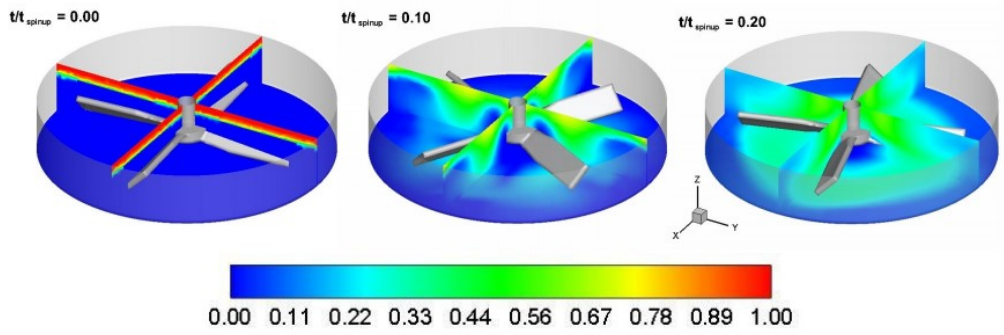

Figure 53. The development of mixing over time for the scalar mixing case. The initial distribution of the tertiary phase is evenly spread in a thin layer across the entire surface of the slurry.

Due the computationally demanding requirements of the scalar mixing, numerical data was only collected up to $t/t_{spin\text{-}up} = 0.2$. Comparisons between the numerical data and experimental data could not be drawn due to several considerations. It was not possible to visualize or quantify the extent of mixing for a viscous tertiary phase into a slurry of 36 wt.% solids experimentally. It was also not possible to simulate the impeller start up that was witnessed experimentally (i.e. numerically the impeller speed is 300 rpm at initiation, whereas experimentally it takes a few seconds for the impeller to reach 300 rpm). Additionally it was not possible to measure quantities of *TKE,* ε, or L_{ED} experimentally given the available resources.

In the attempt to draw a very general comparison between the numerical data and the experimental data, a modified experiment was carried out to compare the experimental and numerical edge velocity of the vessel. A glass vessel with the same numerical dimensions that were used in the simulations was fabricated and fitted with a ground glass lid. The dimensions of the vessel were prepared so there would be no air gaps. Syncrude mature fine tailings (MFT) (500 g) was carefully poured into the glass vessel with the impeller already in position. The MFT was poured in such a way that the surface was level. A 95%/5% mixture of CIL Premium Exterior Satin White Base paint/DI water (66 g) was then deposited in an even layer via a syringe. The lid of the container was then lowered. The Ipevo P2V USB Document Camera was set up with auto click software to take snapshots at 0.1 second intervals. The impeller was attached to a Heidolph RZR 2052 electronic stirrer. The camera was started simultaneously as the stir speed was set to 300 rpm.

Figure 54 shows the movement of the paint along the edge of the glass vessel in a 0.1 second interval.

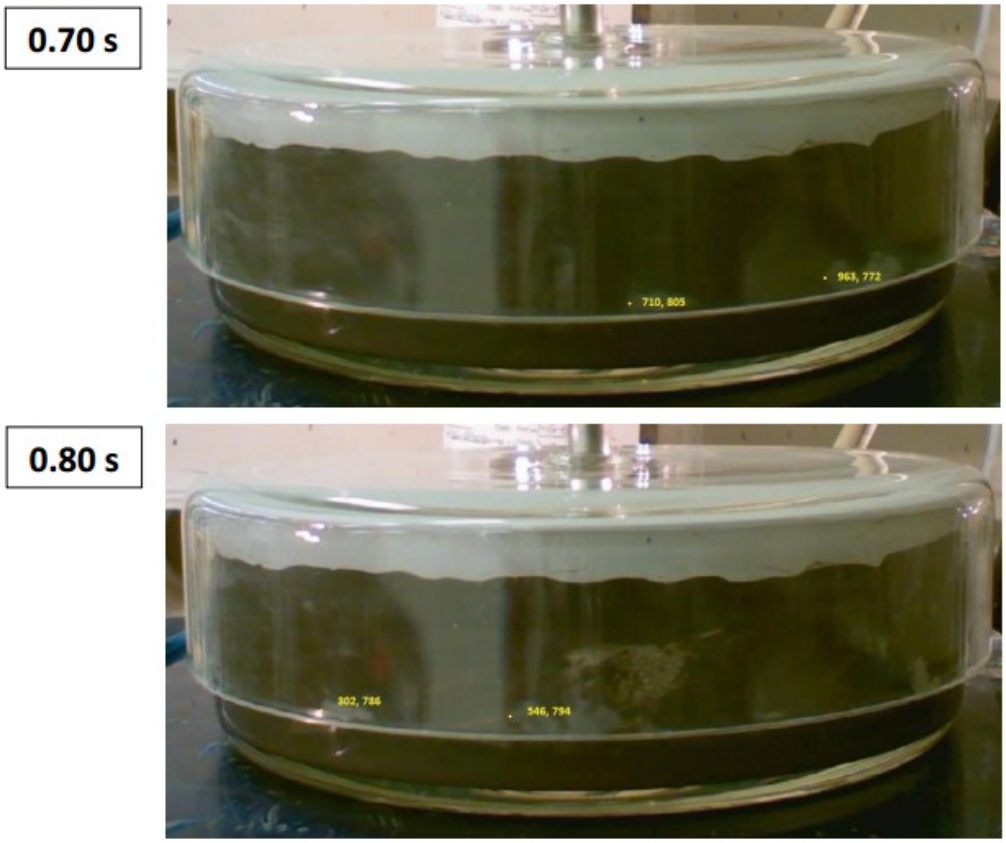

Figure 54. Experimental images of slurry at 300 rpm with paint traces marked by pixel positions.

Figure 55 shows the edge velocity calculated from the scalar mixing simulation.

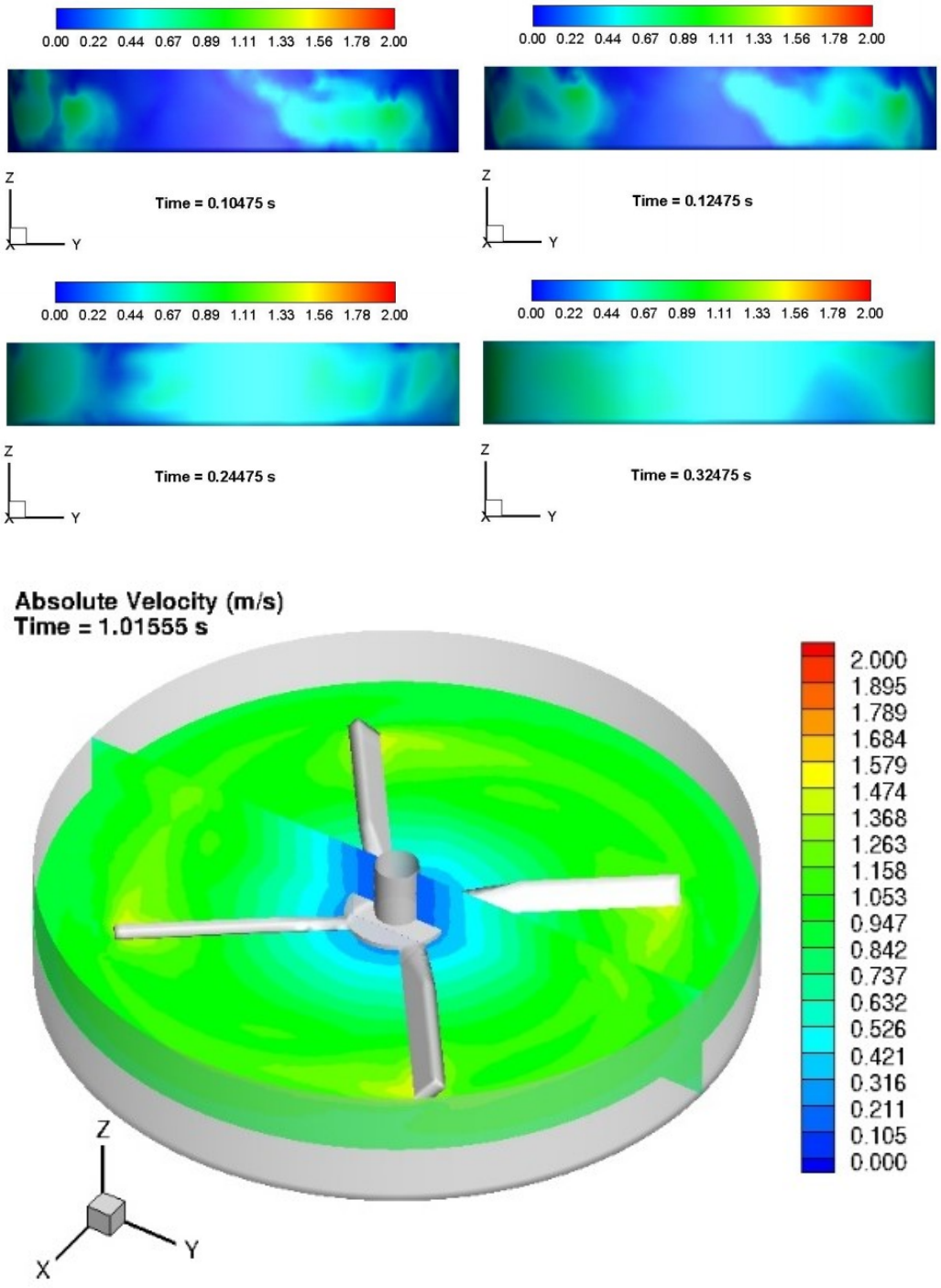

Figure 55. Snapshots of edge velocity for slurry at 300 rpm.

The edge velocity calculated from Figure 54 was 0.87 m/s, which was comparable to the edge velocities shown in Figure 55. To reiterate, this is a very general

comparison. There are too many sources of error to state a direct comparison with any certainty.

Conclusions

Three simulations were carried out to assess the multi-phase mixing of a dense slurry and flocculant solution distribution in a stirred vessel. The first simulation of pure water was compared against the second simulation of a two-phase dense slurry with a solids loading of 36 wt.%. Turbulent kinetic energy *TKE*, turbulent dissipation rate ε, and turbulent length scale L_{ED}, were compared between the first two simulations and produced results that could be supported by literature. The third simulation modeled the distribution of a viscous tertiary phase (flocculant solution) into a dense two-phase slurry (solids content 36 wt.%). Due to limited time and resources, the simulation of the two and three-phase systems could not be validated experimentally. No direct comparisons could be drawn between the multi-phase simulations and the mature fine tailings experimental data. One attempt was made to compare the experimental and numerical edge velocity of the vessel. The edge velocity results suggested a general correlation, however too many variables existed to draw a direct comparison.

With additional resources, there is potential to use computation fluid dynamics simulations to predict mixing behavior of dense slurries such as oil sands mature fine tailings. The ability to model such systems would aid in the experimental

design of testing tailings treatments and would be beneficial in the scale up industrial tailings treatments.

Appendix E References

AEA Technology. (2003). *CFX5 Flow Solver User guide, Computational Fluid Dynamics Services*. Harwell, Oxfordshire, UK: AEA Industrial Technology.

Altway, A., Setyawan, H., Margono, & Winardi, S. (2001). Effect of Particle Size on Simulation of Three-Dimensional Solid Dispersion in Stirred Tank. *Chemical Engineering Research and Design*, *79*(8), 1011–1016. https://doi.org/10.1205/02638760152721578

Bakker, A., Fasano, J. B., & Myers, K. J. (1994). Effect of Flow Pattern on Solids Distribution in a Stirred Tank. . *IChemE. Symp. Ser. No., 136*, 1–8.

Brucato, A., Ciofalo, M., Grisafi, F., & Micale, G. (1998). Numerical Prediction of Flow Fields in Baffled Stirred Vessels: A Comparison of Alternative Modelling Approaches. *Chemical Engineering Science*, *53*(21), 3653–3684. https://doi.org/10.1016/S0009-2509(98)00149-3

Brucato, A., Grisafi, F., & Montante, G. (1998). Particle Drag Coefficients in turbulent Fluids. *Chemical Engineering Science*, *53*(18), 3295–3314. https://doi.org/10.1016/S0009-2509(98)00114-6

Coulson, J. M., Richardson, J. F., Backhurst, J. R., & Harker, J. H. (1990). *Chemical Engineering: Particle Technology & Separation Processes* (4 edition, Vol. 2). Butterworth-Heinemann.

Derksen, J. J. (2003). Numerical Simulation of Solids Suspension in a Stirred Tank. *AIChE Journal*, *49*(11), 2700–2714. https://doi.org/10.1002/aic.690491104

Elghobashi, S. (1994). On Predicting Particle-Laden Turbulent Flows. *Applied Scientific Research*, *52*(4), 309–329. https://doi.org/10.1007/BF00936835

Gidaspow, D. (1994). *Multiphase Flow and Fluidization: Continuum and Kinetic Theory Descriptions* (1 edition). Boston: Academic Press.

Gosman, A. D., Lekakou, C., Politis, S., Issa, R. I., & Looney, M. K. (1992). Multidimensional Modeling of Turbulent Two-Phase Flows in Stirred Vessels. *AIChE Journal*, *38*(12), 1946–1956. https://doi.org/10.1002/aic.690381210

Guha, D., Ramachandran, P. A., Dudukovic, M. P., & Derksen, J. J. (2008). Evaluation of Large Eddy Simulation and Euler-Euler CFD Models for Solids Flow Dynamics in a Stirred Tank Reactor. *AIChE Journal*, *54*(3), 766–778. https://doi.org/10.1002/aic.11417

Issa, R. I., & Gosman, A. D. (1981). The Computation of 3D Turbulent Two-Phase Flows in Mixer Vessels. Presented at the 2nd International

Conference on Numerical Methods in Laminar and Turbulent Flows, Venice, Italy.

Kasat, G. R., Khopkar, A. R., Ranade, V. V., & Pandit, A. B. (2008). CFD Simulation of Liquid-Phase Mixing in Solid–Liquid Stirred Reactor. *Chemical Engineering Science*, *63*(15), 3877–3885. https://doi.org/10.1016/j.ces.2008.04.018

Khopkar, A. R., Kasat, G. R., Pandit, A. B., & Ranade, V. V. (2006). Computational Fluid Dynamics Simulation of the Solid Suspension in a Stirred Slurry Reactor. *Industrial & Engineering Chemistry Research*, *45*(12), 4416–4428. https://doi.org/10.1021/ie050941q

Kresta, S. M., & Wood, P. E. (1991). Prediction of the Three-Dimensional Turbulent Flow in Stirred Tanks. *AIChE Journal*, *37*(3), 448–460. https://doi.org/10.1002/aic.690370314

Kuzmanić, N., & Ljubičić, B. (2001). Suspension of Floating Solids with Up-Pumping Pitched Blade Impellers; Mixing Time and Power Characteristics. *Chemical Engineering Journal*, *84*(3), 325–333. https://doi.org/10.1016/S1385-8947(00)00382-X

Ljungqvist, M., & Rasmuson, A. (2001). Numerical Simulation of the Two-Phase Flow in an Axially Stirred Vessel. *Chemical Engineering Research and Design*, *79*(5), 533–546. https://doi.org/10.1205/02638760152424307

Looney, M. K., Gosman, A. D., Issa, R. I., & Politis, S. (1985). Modeling of the Turbulent Flow of Solid-Liquid Suspensions in Stirred Vessels. Presented at the 5th International Conference of Mathematical Modelling, Berkeley, CA, USA.

Luo, J. Y., Gosman, A. D., Issa, R. I., Middleton, J., & Fitzgerald, M. K. (1993). Full flow field computation of mixing in baffled stirred vessels. *Trans. IChemE*, *71 Part A*, 342–344.

Maynes, D., & Butcher, M. (2002). Steady-State and Decay Dynamics for Impellers of Varying Aspect Ratio in Unbaffled Tanks. *AIChE Journal*, *48*(1), 38–49. https://doi.org/10.1002/aic.690480106

Micale, G., Grisafi, F., Rizzuti, L., & Brucato, A. (2004). CFD Simulation of Particle Suspension Height in Stirred Vessels. *Chemical Engineering Research and Design*, *82*(9), 1204–1213. https://doi.org/10.1205/cerd.82.9.1204.44171

Micale, G., Montante, G., Grisafi, F., Brucato, A., & Godfrey, J. (2000). CFD Simulation of Particle Distribution in Stirred Vessels. *Chemical Engineering Research and Design*, *78*(3), 435–444. https://doi.org/10.1205/026387600527338

Micheletti, M., & Yianneskis, M. (2004). Study of Fluid Velocity Characteristics in Stirred Solid-Liquid Suspensions with a Refractive Index Matching Technique. *Proceedings of the Institution of Mechanical Engineers, Part E: Journal of Process Mechanical Engineering*, *218*(4), 191–204. https://doi.org/10.1243/0954408042466945

Montante, G., Lee, K. C., Brucato, A., & Yianneskis, M. (2001). Numerical Simulations of the Dependency of Flow Pattern on Impeller Clearance in

Stirred Vessels. *Chemical Engineering Science*, *56*(12), 3751–3770. https://doi.org/10.1016/S0009-2509(01)00089-6

Montante, G., & Magelli, F. (2005). Modelling of Solids Distribution in Stirred Tanks: Analysis of Simulation Strategies and Comparison with Experimental Data. *International Journal of Computational Fluid Dynamics*, *19*(3), 253–262. https://doi.org/10.1080/10618560500081795

Montante, G., & Magelli, F. (2007). Mixed Solids Distribution in Stirred Vessels: Experiments and Computational Fluid Dynamics Simulations. *Industrial & Engineering Chemistry Research*, *46*(9), 2885–2891. https://doi.org/10.1021/ie060616i

Montante, G., Micale, G., Magelli, F., & Brucato, A. (2001). Experiments and CFD Predictions of Solid Particle Distribution in a Vessel Agitated with Four Pitched Blade Turbines. *Chemical Engineering Research and Design*, *79*(8), 1005–1010. https://doi.org/10.1205/02638760152721253

Myers, K. J., Corpstein, R. R., Bakker, A., & Fasano, J. B. (1994). Solids Suspension Agitator Design with Pitched-Blade and High Efficiency Impellers. *AIChE Symp. Ser., (Industrial Mixing Technology) No 299*, *90*, 186–190.

Ochieng, A., & Onyango, M. S. (2008). Drag Models, Solids Concentration and Velocity Distribution in a Stirred Tank. *Powder Technology*, *181*(1), 1–8. https://doi.org/10.1016/j.powtec.2007.03.034

Özcan-Taskin, G., & McGrath, G. (2001). Draw Down of Light Particles in Stirred Tanks. *Chemical Engineering Research and Design*, *79*(7), 789–794. https://doi.org/10.1205/026387601753191966

Politis, S. (1989). *Prediction of two-phase solid-liquid turbulent flow in stirred vessels* (PhD). University of London, London, England.

Rizk, M. A., & Elghobashi, S. E. (1989). A Two-Equation Turbulence Model for Dispersed Dilute Confined Two-Phase Flows. *International Journal of Multiphase Flow*, *15*(1), 119–133. https://doi.org/10.1016/0301-9322(89)90089-X

Syamlal, M., & O'Brien, T. J. (1989). Computer Simulation of Bubbles in a Fluidized Bed. *AIChE Symp. Ser.*, *85*(1), 22–31.

Tamburini, A., Cipollina, A., Micale, G., Brucato, A., & Ciofalo, M. (2013). CFD Simulations of Dense Solid–Liquid Suspensions in Baffled Stirred Tanks: Prediction of solid Particle Distribution. *Chemical Engineering Journal*, *223*, 875–890. https://doi.org/10.1016/j.cej.2013.03.048

Tamburini, A., Cipollina, A., Micale, G., Ciofalo, M., & Brucato, A. (2009). Dense solid–Liquid Off-Bottom Suspension Dynamics: Simulation and Experiment. *Chemical Engineering Research and Design*, *87*(4), 587–597. https://doi.org/10.1016/j.cherd.2008.12.024

Tarleton, E. S., & Wakeman, R. J. (2007). *Solid/Liquid Separation Equipment Selection and Process Design /* (1st ed.). Oxford : Butterworth-Heinemann,.

Tennekes, H., & Lumley, J. L. (1972). *A First Course in Turbulence*. MIT Press.

Unadkat, H., Rielly, C. D., Hargrave, G. K., & Nagy, Z. K. (2009). Application of Fluorescent PIV and Digital Image Analysis to Measure Turbulence

Properties of Solid–Liquid Stirred Suspensions. *Chemical Engineering Research and Design*, *87*(4), 573–586. https://doi.org/10.1016/j.cherd.2008.11.011

Wu, J., Zhu, Y. G., & Pullum, L. (2002). Suspension of High Concentration Slurry. *AIChE Journal*, *48*(6), 1349–1352. https://doi.org/10.1002/aic.690480620

Yang, J. (2009). Computational Fluid Dynamics Modeling of Deposition of Oil Sand Slurry into Mature Fine Tailings. PhD. Thesis, University of Alberta.

Yuan, S., & Siman, R. (2012). *Procedures for Validation of Flocculants for High Density FFT with a 125-mm Dynamic Mixing Tank* (Internal Report of the Tailings Environmental Priority Area of Canada's Oil Sands Innovation Alliance No. Rev 4). Research and Development Syncrude Canada Ltd.